An Active Reflection Compensation (ARC) Algorithm for a Wave Generator

V. Amijs

Master of Science Thesis

Delft Center for Systems and Control

An Active Reflection Compensation (ARC) Algorithm for a Wave Generator

MASTER OF SCIENCE THESIS

For the degree of Master of Science in Systems and Control at Delft University of Technology

V. Amijs

July 1, 2020

Faculty of Mechanical, Maritime and Materials Engineering (3mE) · Delft University of Technology

Abstract

The development of an Active Reflection Compensation (ARC) algorithm for a wave generator is challenging. Water behaves in a strong nonlinear way and the time available for the computation of the compensating segment displacements is short. Especially for the case where the wave height sensors are mounted on the surface of the segments.

The current ARC algorithm of Bosch Rexroth is based on an approximation of the Biésel transfer function. Although this method gives fair results, it lacks performance regarding the absorption of oblique waves. This report introduces a wave model identification method based on the Discrete Fourier Transform (DFT) and Extended Kalman Filter (EKF). With the EKF having the ability to include measurement noise and determine model uncertainty, this leads to reasonable estimates of complex second order waves. This report does not only cover the identification part of the algorithm but the full ARC algorithm from wave height measurements to a time series for the segment displacements. Although the results are based on simulations, the algorithm shows a much improved absorption performance for a wide range of propagation directions. It shows decent results for tests with several different sets of wave characteristics. The identification process needs time to mature, which leads to a decrease in absorption performance in the early stage of the free-surface elevation time series. A hybrid method is designed, in which the short-term absorption is based on the current algorithm and, after a certain time interval, the model based algorithm will take over.

Table of Contents

Preface **xiii**

1 Introduction **1**

2 Motivation **3**
- 2-1 Current ARC Method Bosch Rexroth 3
- 2-2 Research Setup 7
  - 2-2-1 Research Problem 7
  - 2-2-2 Research Goal 8
  - 2-2-3 Research Approach 9

3 Proposed Solution **11**
- 3-1 First Order Wave Model 11
- 3-2 Discrete Fourier Transform 12
- 3-3 Linear Model 15
- 3-4 Nonlinear Model 17
  - 3-4-1 State-space Representation 18
  - 3-4-2 Kalman Filter Equations 19
  - 3-4-3 Estimation Results 20
- 3-5 Wave Prediction 24
  - 3-5-1 Prediction Equation 24
  - 3-5-2 Prediction Results 24
- 3-6 Wave Angle Estimation 27
  - 3-6-1 Adjusted State-space Representation 27
  - 3-6-2 Nonlinear Least Squares Optimization 28
  - 3-6-3 Wave Angle Estimation Results 29
  - 3-6-4 Wave Angle Estimation Based on DFT 33
- 3-7 Wave spectrum 37

3-7-1 Free-surface Elevation Time Series 37
3-7-2 Identification Results 38
3-7-3 Tuning 39
3-8 Wave Heights to Segment Displacements 43

4 Testing Results 45
4-1 Simulation Setup 45
4-2 Regular Waves 47
4-3 Irregular Waves 51
4-3-1 Segment Displacement Prediction 58
4-3-2 Short-crested Waves 60
4-3-3 Hybrid ARC Algorithm 61

5 Real Scenario 65
5-1 Measurement Noise 65
5-2 Additional Effects 67

6 Conclusion and Recommendation 69
6-1 Conclusion 69
6-2 Recommendation 70

Bibliography 71

List of Figures

2-1 Illustration for the SWA applied to wave generation, blue coloured area's are assumed to be equal [10]. 4

2-2 Bode diagram of the Biésel transfer function for an elevated flap type wave generator (blue), transfer function of the RLF (red) and theoretical transfer function for reflected to re-reflected waves for RLF (yellow). 5

2-3 Frequency spectrum for re-reflected wave with and without ARC. $\theta = 0^\circ$ [10]. . . 6

2-4 Frequency spectrum for re-reflected 3D waves with and without ARC. $\theta = 45^\circ$ [10]. 7

2-5 Graphical illustration of the difference between generating a perpendicular wave and an oblique wave. 8

3-1 Graphical representation of parametric wave in Eq. (3-1). The figure shows an incoming reflected wave with one frequency component n. 12

3-2 Graphical illustration of aliasing. Samples are indicated by the arrows. With this sampling frequency, no distinction can be made between the actual signal and the aliased signal[1]. 13

3-3 Free-surface elevation time series and DFT of two monochromatic waves with different frequencies. The figures show the effect of spectral leakage as a result of the influence of non-periodicity in the DFT window. DFT window: $[0, \quad 4]$ s. . . 14

3-4 Free-surface elevation time series and DFT of a wave, consisting of a superposition of two sinusoidal functions. The DFT resolution is not sufficient to make a distinction between the two frequencies in the wave signal. DFT window: $[0, \quad 4]$ s. 15

3-5 Left figure: DFT of an harmonic signal and threshold line at 20%. Right figure: the corresponding free-surface elevation time series of the original and the filtered wave signal. 16

3-6 RLS amplitude estimation for a two-component wave. The frequencies are taken as input values and are not further estimated by the algorithm. True frequencies $= [0.51 \quad 0.95]$ Hz, model frequencies $= [0.5 \quad 1]$ Hz. RLS parameters: $\lambda = 0.95$, $\Pi_0 = 10$. 17

3-7 Schematic representation of wave identification part of the ARC. 20

3-8 Angular frequency estimation results for a two-component wave. Diagonal values Q: $[1 \quad 0.1 \quad 0.1]$, diagonal values P: $[1 \quad 0.01 \quad 0.01]$, $R = 0$. $F_s = 10$ Hz. $t_{DFT} = 10$ s, DFT window: $[0, \quad t_{DFT}]$ s, threshold $= 20\%$. 21

3-9 Amplitude (a) and stationary phase (b) estimation results for a two-component wave. Diagonal values Q: $[1 \quad 0.1 \quad 0.1]$, diagonal values P: $[1 \quad 0.01 \quad 0.01]$, $R = 0$. $F_s = 10$ Hz. $t_{DFT} = 10$ s, DFT window: $[0, \quad t_{DFT}]$ s, threshold $= 20\%$. . . 22

3-10 Angular frequency estimation results for a 50-component wave. Diagonal values Q: $[1 \quad 0.1 \quad 0.1]$, diagonal values P: $[1 \quad 0.01 \quad 0.01]$, $R = 0$, $F_s = 10$ Hz, threshold $= 10\%$, DFT times (green lines): $[1 \quad 5 \quad 20 \quad 50 \quad 100 \quad 200 \quad 400]$ s, DFT window sizes: $[0, \quad t_{DFT}]$ s. 23

3-11 Amplitude and stationary phase estimation results for a 50-component wave. Diagonal values Q: $[1 \quad 0.1 \quad 0.1]$, diagonal values P: $[1 \quad 0.01 \quad 0.01]$, $R = 0$, $F_s = 10$ Hz, threshold $= 10\%$, DFT times (green lines in figure (a)): $[1 \quad 5 \quad 20 \quad 50 \quad 100 \quad 200 \quad 400]$ s, DFT windows: $[0, \quad t_{DFT}]$ s. 23

3-12 Snapshot of the wave prediction results for a two-component wave (Figure 3-8. Diagonal values Q: $[1 \quad 0.1 \quad 0.1]$, diagonal values P: $[1 \quad 0.01 \quad 0.01]$, $R = 0$. $F_s = 10$ Hz. $t_{DFT} = 10$ s, DFT window: $[0, \quad t_{DFT}]$ s, threshold $= 20\%$, $T_{pred} = 0.2$ s. 25

3-13 Snapshot of the wave prediction results for a 50-component wave. Diagonal values Q: $[1 \quad 0.1 \quad 0.1]$, diagonal values P: $[1 \quad 0.01 \quad 0.01]$, $R = 0$, $F_s = 10$ Hz, threshold $= 10\%$, DFT times (green lines): $[1 \quad 5 \quad 20 \quad 50 \quad 100 \quad 200 \quad 400]$ s, DFT window sizes: $[0, \quad t_{DFT}]$ s, $T_{pred} = 0.2$ s. 25

3-14 Schematic representation of the wave identification based on just the wave parameters provided by the DFT. 26

3-15 Snapshot of the prediction results for the 50-component wave, just based on the wave parameters provided by the DFTs. $F_s = 10$ Hz, Threshold $= 10\%$, $T_{pred} = 0.2$ s. 27

3-16 Wave angle estimation results for a two-component wave. Diagonal values Q: $[1 \quad 0.1 \quad 0.1]$, diagonal values P: $[1 \quad 0.01 \quad 0.01]$, $R = 0$. $F_s = 10$ Hz. $t_{DFT} = 10$ s, DFT window: $[0, \quad t_{DFT}]$ s, threshold $= 20\%$, wave angle optimization interval: 5 s. 30

3-17 Wave angle estimation results for a 50-component wave. Diagonal values Q: $[1 \quad 0.1 \quad 0.1]$, diagonal values P: $[0.001 \quad 0.01 \quad 0.01]$, $R = 0$. $F_s = 10$ Hz. $t_{DFT} = [1 \quad 5 \quad 20 \quad 50 \quad 100 \quad 200 \quad 400]$ s, DFT windows: $[0, \quad t_{DFT}]$ s, threshold $= 10\%$, wave angle optimization interval: 5 s. 31

3-18 NLS Grid search for wave angle estimation (Figure 3-17). All possible values for optimizable wave angle θ and corresponding residuals. Based on the estimated wave parameters for the 50-component wave at 500 seconds. 31

3-19 Phase estimation results for a 50-component wave. Threshold $= 10\%$, $F_s = 10$ Hz, $R = 0$. (a) $q_\varphi = 1$, $p_\varphi = 0.001$ (b) $q_\varphi = 100$, $p_\varphi = 1$. 32

3-20 Wave angle estimation results for the same wave as in Figure 3-17. Altered values: $q_\varphi = 100$, $p_\varphi = 1$ 33

3-21 (a) Free-surface elevation time series of a monochromatic oblique wave measured by two neighbouring segments. (b) Actual stationary phase terms of time series in green and DFT phase terms in red. 34

3-22 Wave angle estimation for the 50-component wave (Figure 3-17), using the DFT wave parameters. 35

3-23 Variable wave angle estimation for two different DFT window sizes. 36

3-24 Wave angle estimation for a multi-directional wave at 100 sec. A separate wave angle is estimated for all the frequencies qualified for angle estimation. DFT window: $[0, \quad 100]$ s. 37

3-25 Theoretical and actual JONSWAP spectrum (a) and corresponding free-surface elevation time series (b). $H_s = 0.4$ m, $T_p = 2$ s. 38

3-26 Wave angle estimation for the JONSWAP wave in Figure 3-25. 39

3-27 Influence of DFT threshold value on the RMS errors between predicted and actual wave (JONSWAP), for different time intervals. 40

3-28 Influence of the model uncertainty matrix Q on the RMS errors between predicted and actual wave (JONSWAP), for different time intervals. 41

3-29 Influence of the state covariance matrix P on the RMS errors between predicted and actual wave (JONSWAP), for different time intervals. 41

3-30 Influence of the prediction horizon on the RMS errors between predicted and actual wave (JONSWAP), for different time intervals. 42

3-31 Schematic representation of ARC EKF. 43

4-1 Schematic overview of the simulation setup. 46

4-2 Snapshot of estimation results for a regular second order wave. Q: $= [0.1 \quad 0.1 \quad 0.1]$, R $= 10$, P: $[0.01 \quad 0.01 \quad 0.01]$, $t_{DFT} = 1$ s, DFT window: $[0, \quad t_{DFT}]$, threshold: 30%. 47

4-3 Snapshots of absorption segment displacement time series for both the ARC methods, compared to the time series for the generation of the wave. Corresponding to the wave in Figure 4-2. 48

4-4 Amplitude spectrum comparison based on the segment displacement time series for the generation of the wave and the absorption time series of both the ARC algorithms. Corresponding to the wave in Figure 4-2. **f = 1 Hz**, $\boldsymbol{\theta} = \mathbf{0}$ °, **H= 0.16 m**, Time window spectrum = **[10, 200]** s. 49

4-5 Amplitude spectrum comparison based on the segment displacement time series for the generation of the wave and the absorption time series of both the ARC algorithms. **f = 0.4 Hz**, $\boldsymbol{\theta} = \mathbf{0}$ °, **H= 0.6 m**, Time window spectrum = **[10, 200]** s. 50

4-6 Amplitude spectrum comparison based on the segment displacement time series for the generation of the wave and the absorption time series of both the ARC algorithms. **f = 0.6 Hz**, $\boldsymbol{\theta} = \mathbf{45}$ °, **H= 0.5 m**, Time window spectrum = **[10, 200]** s. 50

4-7 Amplitude spectrum comparison based on the segment displacement time series for the generation of the wave and the absorption time series of both the ARC algorithms. $\boldsymbol{T_p} = \mathbf{2}$ **s**, $\boldsymbol{H_s}$**= 0.4 m**, $\boldsymbol{\theta} = \mathbf{0}$ °, Time window spectrum = **[10, 100]** s. 52

4-8 Amplitude spectrum comparison based on the segment displacement time series for the generation of the wave and the absorption time series of both the ARC algorithms. $\boldsymbol{T_p} = \mathbf{2}$ **s**, $\boldsymbol{H_s}$**= 0.4 m**, $\boldsymbol{\theta} = \mathbf{0}$ °, Time window spectrum = **[10, 100]** s. 52

4-9 Amplitude spectrum comparison based on the segment displacement time series for the generation of the wave and the absorption time series of both the ARC algorithms. $\boldsymbol{T_p} = \mathbf{2}$ **s**, $\boldsymbol{H_s}$**= 0.4 m**, $\boldsymbol{\theta} = \mathbf{0}$ °, Time window spectrum = **[100, 500]** s. 53

4-10 Snapshots of absorbing segment displacement time series of both the ARC algorithms compared to the time series for the generation of the wave. $\boldsymbol{T_p} = \mathbf{2}$ **s**, $\boldsymbol{H_s}$**= 0.4 m**, $\boldsymbol{\theta} = \mathbf{0}$ °. 54

4-11 Amplitude spectrum comparison based on the segment displacement time series for the generation of the wave and the absorption time series of both the ARC algorithms. $\boldsymbol{T_p}$ **= 2 s**, $\boldsymbol{H_s}$**= 0.4 m**, $\boldsymbol{\theta}$ **= 44** °, Time window spectrum = **[100, 500]** s. 54

4-12 Snapshots of absorbing segment displacement time series of both the ARC algorithms compared to the time series for the generation of the wave. $\boldsymbol{T_p}$ **= 2 s**, $\boldsymbol{H_s}$**= 0.4 m**, $\boldsymbol{\theta}$ **= 44** °. 55

4-13 Amplitude spectrum comparison based on the segment displacement time series for the generation of the wave and the absorption time series of both the ARC algorithms. $\boldsymbol{T_p}$ **= 1.8 s**, $\boldsymbol{H_s}$**= 0.3 m**, $\boldsymbol{\theta}$ **= 15** °, Time window spectrum = **[100, 500]** s. 55

4-14 Snapshots of absorbing segment displacement time series of both the ARC algorithms compared to the time series for the generation of the wave. $\boldsymbol{T_p}$ **= 1.8 s**, $\boldsymbol{H_s}$**= 0.3 m**, $\boldsymbol{\theta}$ **= 15** °. 56

4-15 Amplitude spectrum comparison based on the segment displacement time series for the generation of the wave and the absorption time series of both the ARC algorithms. $\boldsymbol{T_p}$ **= 2.3 s**, $\boldsymbol{H_s}$**= 0.3 m**, $\boldsymbol{\theta}$ **= 35** °, Time window spectrum = **[100, 500]** s. 56

4-16 Snapshots of absorbing segment displacement time series of both the ARC algorithms compared to the time series for the generation of the wave. $\boldsymbol{T_p}$ **= 2.3 s**, $\boldsymbol{H_s}$**= 0.3 m**, $\boldsymbol{\theta}$ **= 35** °. 57

4-17 Amplitude spectrum comparison based on the segment displacement time series for the generation of the wave and the absorption time series of both the ARC algorithms. $\boldsymbol{T_p}$ **= 2.2 s**, $\boldsymbol{H_s}$**= 0.6 m**, $\boldsymbol{\theta}$ **= 40** °, Time window spectrum = **[100, 500]** s. 57

4-18 Snapshots of absorbing segment displacement time series of both the ARC algorithms compared to the time series for the generation of the wave. $\boldsymbol{T_p}$ **= 2.2 s**, $\boldsymbol{H_s}$**= 0.6 m**, $\boldsymbol{\theta}$ **= 40** °. 58

4-19 Amplitude spectrum comparison based on the real-time and predicted (PRED) segment displacement time series of the ARC EKF for the absorption of the wave versus the time series for the generation of the wave. $\boldsymbol{T_p}$ **= 2.2 s**, $\boldsymbol{H_s}$**= 0.6 m**, $\boldsymbol{\theta}$ **= 40** °, Time window spectrum = **[100, 500]** s, RMS prediction spectrum: $\boldsymbol{1.1e^{-3}}$, RMS real-time spectrum: $\boldsymbol{1.0e^{-3}}$. 59

4-20 Snapshot of the real-time and predicted absorbing segment displacement time series of the ARC EKF compared to the time series for the generation of the wave. $\boldsymbol{T_p}$ **= 2.2 s**, $\boldsymbol{H_s}$**= 0.6 m**, $\boldsymbol{\theta}$ **= 40** °, RMS predicted segment displacements: $\boldsymbol{2.4e^{-2}}$, RMS real-time segment displacements: $\boldsymbol{2.3e^{-2}}$. 60

4-21 Amplitude spectrum comparison based on the segment displacement time series for the generation of the wave and the absorption of the wave for both the ARC algorithms. $\boldsymbol{T_p}$ **= 2 s**, $\boldsymbol{H_s}$**= 0.45 m**, Time window spectrum = **[100, 500]** s, Spreading parameter **s = 1**. 61

4-22 Snapshots of absorbing segment displacement time series of both the ARC algorithms compared to the time series for the generation of the wave. $\boldsymbol{T_p}$ **= 2 s**, $\boldsymbol{H_s}$**= 0.45 m**, Spreading parameter **s = 1**. 61

4-23 Hybrid system: transition from the time series of the Rexroth ARC to the time series for the ARC EKF. 62

4-24 Amplitude spectrum comparison based on the segment displacement time series for the generation of the wave and the absorption of the wave, for the Rexroth ARC with the current and the new 3D implementation. $\boldsymbol{T_p}$ **= 2 s**, $\boldsymbol{H_s}$**= 0.4 m**, $\boldsymbol{\theta}$ **= 44** °, Time window spectrum = **[10, 100]** s. 63

4-25 Amplitude spectrum comparison based on the ARC EKF and hybrid ARC segment displacement time series for the absorption of the wave versus the time series for the generation of the wave. $\boldsymbol{T_p}$ **= 2 s**, $\boldsymbol{H_s}$**= 0.4 m**, $\boldsymbol{\theta}$ **= 44** °, Time window spectrum = **[10, 500]** s, RMS ARC EKF spectrum: $\boldsymbol{7.6e^{-4}}$, RMS hybrid ARC spectrum: $\boldsymbol{5.4e^{-4}}$. 64

5-1 Snapshots of absorbing segment displacement time series for the Rexroth ARC and the hybrid ARC compared to the time series for the generation of the wave. Measurement noise has been added to the free-surface elevation time series of the regular wave. $\boldsymbol{T}$ **= 1 s**, $\boldsymbol{H}$**= 0.16 m**, $\boldsymbol{\theta}$ **= 0** °, Measurement noise: $\boldsymbol{\sigma^2} = 1\boldsymbol{e^{-3}}$. 66

5-2 Amplitude spectrum comparison based on the segment displacement time series for the generation of the wave and the absorption time series of the Rexroth ARC and the hybrid ARC. **f = 1 Hz**, $\boldsymbol{\theta}$ **= 0** °, **H= 0.16 m**, Time window spectrum = **[10, 200]** s, Measurement noise: $\boldsymbol{\sigma^2} = 1\boldsymbol{e^{-3}}$. 66

List of Tables

3-1 Intervals for the randomly created parameters of the reflected wave. 20

3-2 RMS errors for according to the time intervals between the DFTs, corresponding to the free-surface elevation time series in Figure 3-13. 26

3-3 RMS errors for according to the same time intervals as in Table 3-2, corresponding to the free-surface elevation time series in Figure 3-15. 27

3-4 RMS errors for according to the time intervals between the DFTs, corresponding to the wave in Figure 3-25. Model parameters: Threshold $= 10\%$, $F_s = 10$ Hz, Q: $[1 \quad 0.1 \quad 0.1]$, P: $[1 \quad 0.01 \quad 0.01]$, $T_{pred} = 0.2$ sec. 38

4-1 Parameter values of ARC EKF for the absorption of irregular waves. 51

Preface

This thesis report is conducted in cooperation with Bosch Rexroth B.V. With its 30 years of experience the company has supplied numerous systems for academic and commercial purposes. Written under the supervision of:

Prof.dr.ir. J. W. van Wingerden *(DCSC)*
Ir. M. van de Molengraft *(Bosch Rexroth)*
Dr.-Ing. M. Brühl *(DCSC)*

Chapter 1

Introduction

During the development of offshore structures, like drilling platforms or coastal profiles, a lot of testing will be done in a water tank with the use of scale models. Artificial waves are produced by a wave generator in order to simulate a real sea state. This is a crucial part in the design process, because in this way it is possible to see how these structures deal with the forces which they will be exposed to in real waters.

However, where real ocean waves will propagate towards the 'infinite' surface area of the sea, the artificial waves produced in a water tank will meet the boundaries of the testing environment. This results in reflected waves that disturb the desired wave profile. Although passive absorbers, in the form of e.g. beaches, are often installed on the opposing side of the wave generator when testing floating structures, these fail to absorb the waves completely. Reflection of the incident wave by the boundaries of the facility might be unavoidable, yet it is essential that this wave, together with the wave reflected from the structure itself, does not get re-reflected again by the wave generator. If these reflected waves do not get compensated, it won't take long before the desired wave profile gets disturbed to such a degree that the test run needs to be stopped in order for the water to calm down. This phenomenon limits the effective testing time of the facility drastically.

The current ARC method of Bosch Rexroth will be elaborated, discussing the (dis)advantages regarding its absorption performance. Subsequently a new ARC algorithm is introduced based on the identification of a first order wave model. The performances will be compared by running simulation on several different waves. For the basic theory about water dynamics, generation and absorption of waves, refer to the preceding literature survey [1].

Chapter 2

Motivation

2-1 Current ARC Method Bosch Rexroth

As thoroughly discussed in [1], the current ARC method used by Rexroth is based on the Shallow Water Approximation (SWA). The SWA is extended with several other filters to approximate the Biésel transfer function. The Biésel function transfers the displacements of the wave generator segments to wave heights, provided that the frequency content of the wave is known. It is used for wave generation as the desired wave profile is calculated beforehand. The inverse of the Biésel function, transferring the measured wave heights to corresponding segment displacements, could be useful for the absorption of the reflected wave. The problem is that the frequency content of the reflected waves is unknown, making it impossible to use the Biésel function for this application. Its approximation, based on the SWA, results in a Real-time Linear Filter (RLF) that transfers the measured wave heights directly to segment displacements without needing in-depth information (like frequency content) about the reflected wave. The filter is stable, but has limited performance regarding oblique waves. As the lag between the measurement and control action should be minimal, the computation time is limited. Figure 2-1 shows the theory of the SWA applied to wave generation in the case of an elevated flap type wave generator. The volume of the water displaced by the wave generator is equal to the crest volume of the propagating wave. In case of the segment moving backwards the volume of the displacement is equal to the volume of the resulting trough of the wave.

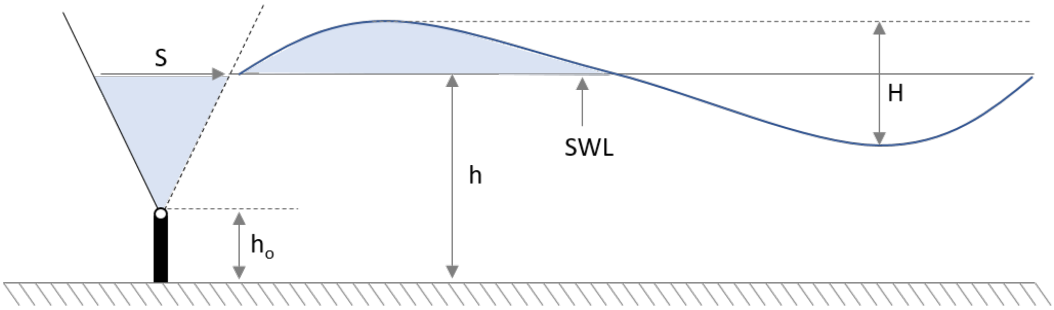

Figure 2-1: Illustration for the SWA applied to wave generation, blue coloured area's are assumed to be equal [10].

H in the figure refers to the wave height, S to the segment stroke, h to the water depth and h_0 to the hinge elevation measured from the floor. The still water level is indicated by SWL. In control theory the SWA equations translate to transfer functions having the form of an integrator, as given in Eq. (2-1). With g as the gravitational acceleration.

$$\text{Piston type :} \qquad \frac{H}{S} = \sqrt{\frac{g}{h}} \cdot \frac{1}{s} \tag{2-1}$$

$$\text{Flap type :} \qquad \frac{H}{S} = \frac{2}{h - h_0} \cdot \sqrt{g \cdot h} \cdot \frac{1}{s}$$

Figure 2-2 is provided by Rexroth to give insight into the frequency response of their algorithm. The blue line shows the Biésel function for a flap type wave generator, given in Eq. (2-2) [2] transferring the segment set points to wave heights. This biésel transfer function corresponds to the progressive part of the wave [1].

$$\frac{H}{S} = \frac{2}{k(h - h_0)} \left[\frac{\sinh(kh)((h - h_0)k \sinh(kh) - \cosh(kh) + \cosh(kh_0))}{\sinh(kh)\cosh(kh) + kh} \right] \tag{2-2}$$

With k as the wave number, depending on the frequency according the dispersion relation [1]. For this figure, the water depth is taken to be $h = 7$ m and the hinge elevation $h_0 = 3.5$ m. The red line shows the transfer function of the RLF for the segment set points to wave heights. The basis of this transfer function is the SWA equation for a flap type wave generator in Eq. (2-1). This equation is extended with several other filters to create a better fit to the Biésel function in Eq. (2-2). Although some of these additional filters are more thoroughly elaborated in [1], the transfer function for the RLF and its corresponding parameter values are classified and can therefore not be shared in this report. Different values can be assigned to the water depth h and, in the case of a flap type wave generator, the hinge elevation h_0 to adjust the algorithm for different wave generator characteristics. In this case, the values for the water depth and hinge elevation are taken to be the same as for the Biésel function for comparison. As visible in the figure, for the frequency range of $0.1 - 3$ Hz the transfer function of the RLF shows a similar frequency response as the Biésel function. The yellow line shows the transfer function of the reflected wave to the re-reflected wave for the RLF to show the theoretical absorption performance of the algorithm. This result is not based on actual measurements, but the frequency response is purely based on the RLF transfer function. This response is given to show that the performance of the RLF differs for the each of the frequencies present in the reflected wave. Looking at the larger negative gain for a frequency of 0.4 Hz, this frequency will theoretically be absorbed better than a frequency component of e.g. 1 Hz. The line shows very low to zero absorption performance for frequencies beyond 3 Hz.

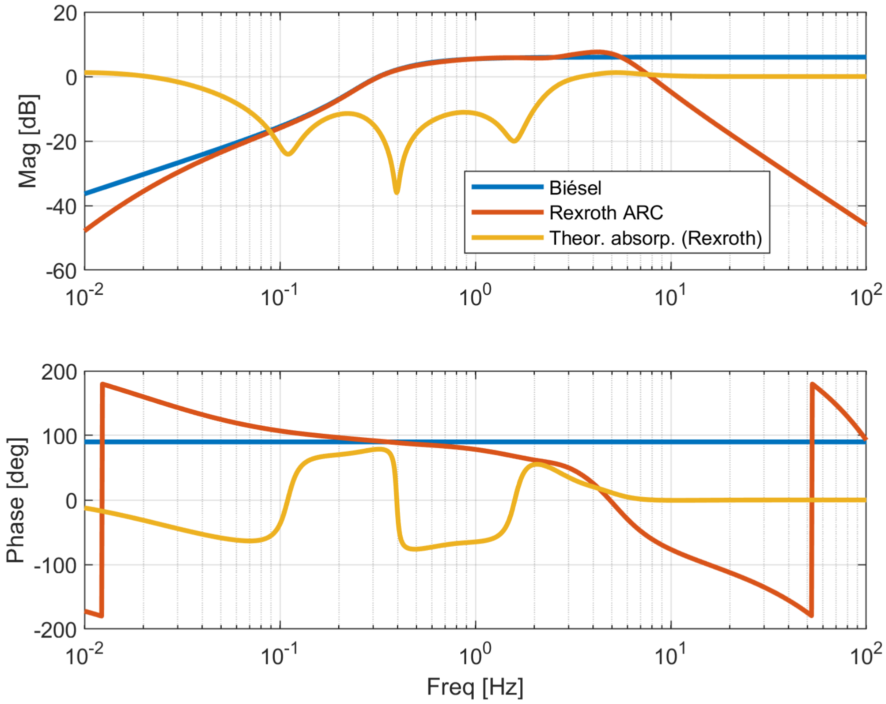

Figure 2-2: Bode diagram of the Biésel transfer function for an elevated flap type wave generator (blue), transfer function of the RLF (red) and theoretical transfer function for reflected to re-reflected waves for RLF (yellow).

3D Implementation To compensate for waves coming in with a propagation direction that differs from the perpendicular line, Rexroth uses a rudimentary method including the measurements from the neighbouring segments. The ARC algorithm takes the form of a two-dimensional filter, given in Eq. (2-3). Subscript i accounts for the time, or discrete time steps, and j relates to the measurements of the neighbouring segments. k and l are iteration variables for the time and spatial measurements respectively. With $u_{i,j}$ representing the measured wave height as input of the system, and $v_{i,j}$ the segment position needed to absorb the wave as output. M_2 is set on 1, this means that only the information of the neighbouring segments will be used. These extra measurements are not implemented for the recursive part, so $N_2 = 0$. M_1 indicates the amount of past measurements taken into account and N_1 the amount of past segment set points. a and b correspond to the filter parameters of RLF transfer function. The values of these parameters can be adjusted for different values of k and l to determine the influence of the neighbouring measurements.

$$v_{i,j} = \sum_{l=-M_2}^{M_2} \sum_{k=0}^{M_1} a_{kl} \cdot u_{i-k,j-l} + \sum_{l=-N_2}^{N_2} \sum_{k=1}^{N_1} b_{kl} \cdot v_{i-k,j-l} \tag{2-3}$$

Performance and Conclusion Actual test measurements using this ARC algorithm have been performed in the Seakeeping and Maneuvering Basin Marin [10], a prominent research institute for offshore structures. The advantage of this water basin is the ability to lower the passive absorbers on the long side of the tank, which results in fully reflected waves back to the wave generator. The ARC algorithm can then be used to compensate for these reflected waves. In order to create insight in the performance the spectral density of the surface elevations of the re-reflected waves was measured in the middle of the basin. These tests have been performed using a flap type wave generator with a hinge elevation of $h_0 = 3.4$ m. The water depth is $h = 5$ m. For absorption of the wave, the inverse of the RLF transfer function for flap type wave generators is used to obtain the transfer from the wave heights to segment set points. The transfer function is extended with the 3D implementation covered in the previous paragraph to compensate for oblique waves. The upcoming figures will show the spectral density of two test runs; first with the ARC algorithm switched off (blue), resulting in a full re-reflection of the wave, and then with the ARC switched on (black). Figure 2-3 shows the performance of a reflected wave that propagates with an angle perpendicular to the wave generator. The incident wave is generated by the segments on the long side of the tank, directed perpendicular to the opposing side. The wave angle θ of the reflected wave hitting the segments is the angle with respect to the perpendicular line, so in this case $\theta = 0$. The figure shows that the ARC algorithm reduces the energy of the reflected wave significantly.

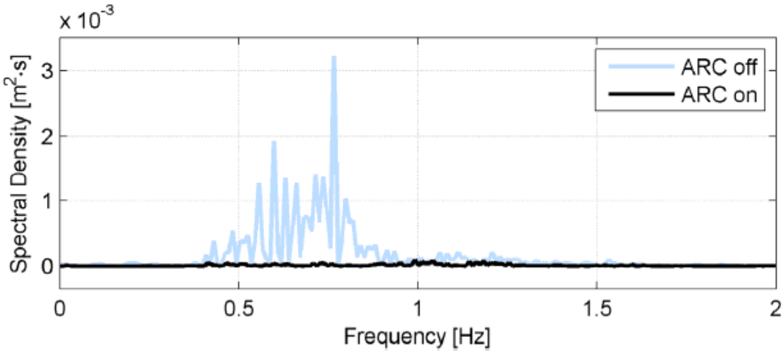

Figure 2-3: Frequency spectrum for re-reflected wave with and without ARC. $\theta = 0°$ [10].

Similar measurements have been performed for a reflected wave with a direction of $\theta = 45°$ (Figure 2-4). This oblique wave has been created using the segments on the short side of the basin, directed at the long side. The figure shows that the ARC still reduces the reflected wave energy, but the performance is lower than in the case of the perpendicular wave. Especially frequencies above 1 Hz seem to be absorbed poorly. This is most likely caused by the phase difference and the ratio between the segment width and the wave length at these frequencies [10]. For most of the wave lengths the rudimentary 3D implementation of assigning fixed weights to measurements of neighbouring segments results in an inaccurate segment displacement for the absorption of oblique waves.

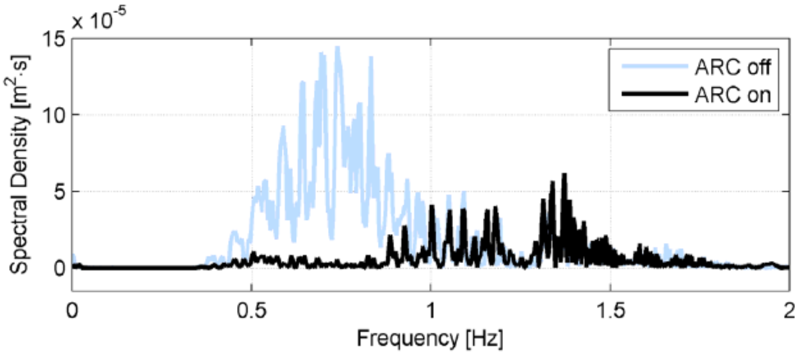

Figure 2-4: Frequency spectrum for re-reflected 3D waves with and without ARC. $\theta = 45°$ [10].

To conclude, this method is mainly developed by hands-on tuning, is fairly easy to implement and delivers good results for reflected waves with an angle perpendicular to the wave generator. Unfortunately, in a real scenario waves reflect with a wide range of propagation angles.

2-2 Research Setup

2-2-1 Research Problem

When looking at Figures 2-3 and 2-4, it is clear that the propagation angle of the reflected wave has a major impact on the absorption performance. The current 3D implementation used by Rexroth appears to be lacking ability to compensate for oblique waves, resulting in incorrect segment displacements for absorption.

Importance of Wave Angle To emphasize the importance of the wave angle to the segment displacement, Eq. (2-4) shows the equation that relates the 2D Biésel function for perpendicular waves (Bi_2) to the 3D Biésel function (Bi_3). The equation shows that the difference between generating the same wave perpendicularly or oblique, is the scaling of the segment displacements according to the wave angle θ. The Biésel function transfers the segment displacements to the corresponding wave heights for the generation of waves, but the relation remains when taking the inverse of the functions for the absorption of waves.

$$Bi_3 = \frac{Bi_2}{\cos(\theta)} \tag{2-4}$$

In order to get a better intuitive understanding of the concept, this can be graphically explained using Figure 2-5.

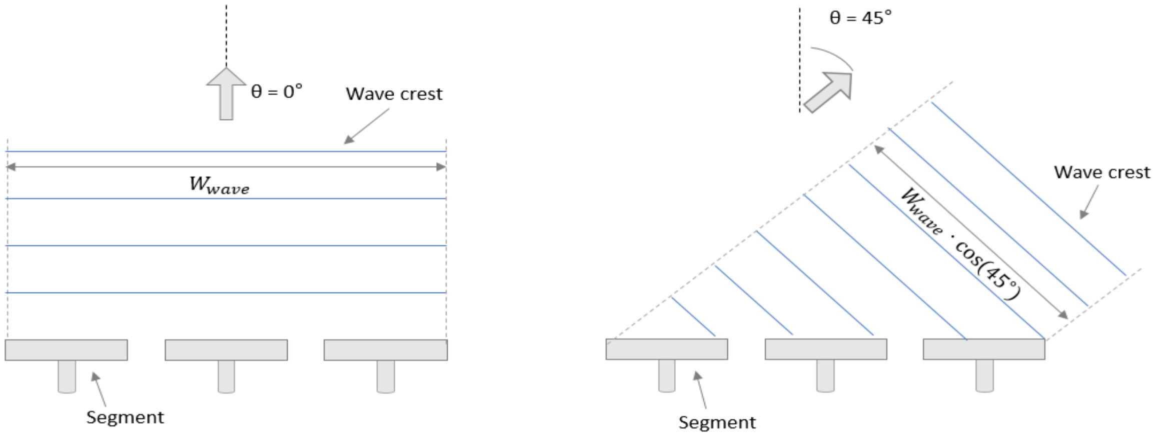

(a) Perpendicular wave, $\theta = 0°$.

(b) Oblique wave, $\theta = 45°$.

Figure 2-5: Graphical illustration of the difference between generating a perpendicular wave and an oblique wave.

The left figure illustrates the generation of an incident wave with an angle of 0° and the right figure for a wave with an angle of 45°. The solid lines indicate the wave crests and the dashed lines outline the width of the incident wave (W_{wave}) as generated by the three segments. As illustrated in the figure, this width decreases as the propagation angle θ increases. The width of the oblique wave can be obtained by scaling the perpendicular width by $\cos(\theta)$. This results in a corresponding reduction of the amplitude of the segment displacement (scaled by $\cos(\theta)$) for the generation of the same wave height over a smaller width. For the same reason, smaller segment displacement amplitudes are required for the absorption of oblique waves.

For the Rexroth ARC the amplitude of the resulting segment displacement is a direct result of the combination of the settings of the 2D filter (Eq. (2-3)), the propagation angle, the ratio between the wave length (depending on the frequency) and the segment width [10]. This method is not adaptive when it comes to diverging wave angles, which explains the lack of performance when dealing with oblique waves.

Even more, Figure 2-2 shows that the absorption performance of the Rexroth ARC theoretically depends on the frequencies of the reflected wave, although this cannot be verified in the actual test results given in Figures 2-3 and 2-4. Obviously, it is desirable for an ARC algorithm to have a decent absorption performance regarding the different frequencies and wave heights present in the reflected wave.

2-2-2 Research Goal

As a result of the research problem, an important point of improvement is the absorption of oblique reflected waves. Additionally, the proposed solution should have a decent performance regarding diverging values for the wave frequencies and wave heights.

This results in the main objective for the thesis; Creating an ARC algorithm for a 3D wave generator that is able to absorb reflected waves with diverging propagation angles, wave frequencies and wave heights.

2-2-3 Research Approach

This research introduces an ARC algorithm that is based on the identification of a first order wave model. The first step is to find a suitable algorithm for the estimation of the parameters. The performance of the estimation will first be tested on simple waves, and subsequently for waves with increasing complexity. In this way it is possible to gain insight into the process and deal with the limits of the method. As there will not be a possibility to test the algorithms in actual facilities, the tests results will be obtained using simulations. In order to benchmark the proposed method to the current Rexroth ARC, both the segment displacement time series responsible for the absorption of the wave will be compared for reflected waves with diverging characteristics. These simulations consider a simplified scenario compared to actual test runs. Some additional difficulties concerning wave absorption in real test facilities will be covered in a separate chapter.

Chapter 3

Proposed Solution

Instead of transferring the reflected wave height measurements directly to segment displacements, the data can also be used to perform a real-time identification of a wave model. The proposed algorithm performs a separate wave identification for each of the segments according to the measurements of the corresponding wave height sensors mounted on their surfaces. The idea is to take the identified parametric reflected wave and apply a phase shift of π to obtain the counter wave that cancels this reflected wave out. The counter wave can then be transposed into displacements for that segment using the Biésel transfer function instead of using the RLF. Including wave angle estimation using the measurements of neighbouring sensors would make it possible to scale these displacements with respect to the propagation angle of the reflected wave. More complex, and therefore more computationally expensive, algorithms will result in an increased phase lag between the time of measurement and the control action response time. Although this problem is not yet substantial with the current algorithm, it is something that has to be taken into account when using more extensive algorithms. An additional advantage of identifying a wave model is that it could be used to make predictions over a short time span in order to compensate for this lag.

3-1 First Order Wave Model

Higher order wave models introduce a large amount of extra parameters, due to the additional super- and sub-harmonic components [1], which can be unpractical for model identification. For this reason, the identification will be based on a first order wave model. The free-surface elevation can be described using the sum of a number of sinusoidal functions, as given in Eq. (3-1) for each segment i. This equation corresponds to Equation (3.4) in [2].

$$y_{i,k} = \sum_{n=1}^{M} a_n \cos\{\underbrace{\omega_n t_k}_{\varphi_{\text{time}}} - \underbrace{k_n[x_{i,k}^{seg}\cos(\theta_n+\pi) + y_i^{seg}\sin(\theta_n+\pi)]}_{\varphi_{\text{space}}} + \underbrace{\phi_n}_{\varphi_{\text{fixed}}}\} \tag{3-1}$$

a_n = Amplitude $\qquad$ ω_n = Angular frequency $\qquad$ $y_{i,k}$ = Free-surface elevation

θ_n = Wave angle ϕ_n = Fixed phase $x_{i,k}^{seg}/y_i^{seg}$ = Relative segment position

k_n = Wave number t_k = Discrete time

The subscript k refers to the discrete time step, n to the different frequency components and i to the segment of the wave generator. The segment positions $x_{i,k}^{seg}$ and y_i^{seg} are relative positions with respect to a certain segment reference position in the basin. y_i is fixed for every segment, as it refers to where the segment is positioned in line. $x_{i,k}^{seg}$ is variable according to the displacement of the segment. The directional information is represented as $\theta_n + \pi$ for the incoming reflected wave, as the range for the wave angle θ_n for the generation of waves is on the first and fourth quadrant of the unit circle. To get a better understanding of the parameters, Figure 3-1 shows a graphical representation of an incoming reflected wave in the case of a piston type wave generator. $y_{k,i}$ indicates the surface elevation measured by the wave height sensor on the surface of the segment, with respect to the SWL. The wave length λ_n and the wave number k_n are related according the following equality: $k_n = 2\pi/\lambda_n$. C refers to the phase speed on the incoming wave: $C = \lambda_n/T_n$. With T_n as the wave period, related to the angular frequency as follows: $\omega_n = 2\pi/T_n$. For a graphical representation of the wave angle θ_n, refer to Figure 2-5.

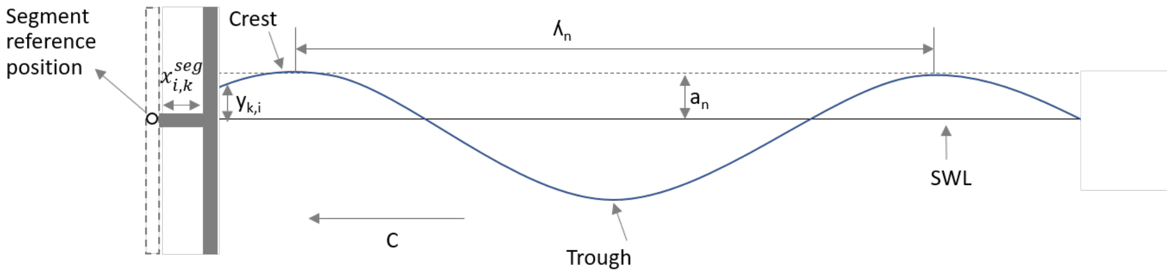

Figure 3-1: Graphical representation of parametric wave in Eq. (3-1). The figure shows an incoming reflected wave with one frequency component n.

Eq. (3-1) makes a distinction between three different phase terms. The time dependent phase term relates to the angular frequency of the component. The spatial phase term depends on the wave angle, the wave number and the segment position. This spatial term is used for the estimation of the wave angle, elaborated later in the report. The wave number k_n results from the angular frequency ω_n according the dispersion relation [1]. This is why the frequency content of the wave is important for the estimation of the wave angle. At last, every frequency component has a fixed phase term ϕ_n.

The following variables are left to be estimated for every component n: a_n, ω_n, θ_n, ϕ_n. Although Eq. (3-1) gives the free-surface elevation according to each individual segment i, the measurement of multiple segments have to be taken into account for the estimation of the wave angle θ_n.

3-2 Discrete Fourier Transform

When dealing with harmonic signals, the Discrete Fourier Transform (DFT) is often considered due to its capability of providing insight into the frequency content. Fourier analyses not only give insight into the frequencies present in the signal, but also into the corresponding amplitudes and phases. The equation for the DFT is given in Eq. (3-2) according to the wave height measurements of each segment i.

$$Y_i[n] = \sum_{k=0}^{N-1} y_{i,k} e^{-j\frac{2\pi}{N}nk} \qquad \text{for } n = 0, 1, \ldots, N-1 \tag{3-2}$$

The correlations between the discrete signal $y_{i,k}$ and sinusoidal functions with different frequencies are stored in the Fourier coefficients $Y_i[n]$. [6] describes how the values of $Y_i[n]$ have to be interpreted to extract information about the frequencies, and their corresponding amplitudes and phases.

Aliasing When sampling harmonic signals it is important to choose the right sampling frequency. In case of undersampling, two signals with different frequencies can be seen as the same signal. This is called aliasing and is illustrated in Figure 3-2. The arrows in the figure indicate the moments in time when a sample is taken. The sampling frequency is too low to make a distinction between the actual signal and the aliased signal.

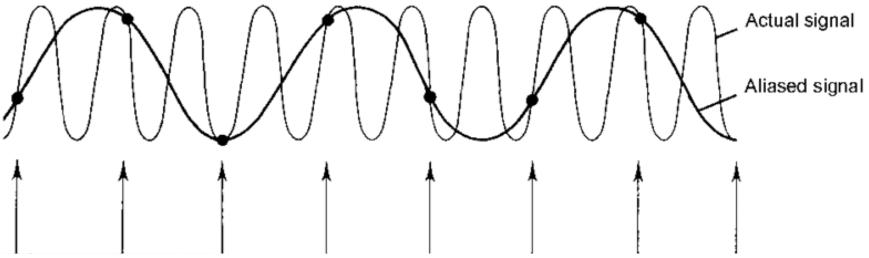

Figure 3-2: Graphical illustration of aliasing. Samples are indicated by the arrows. With this sampling frequency, no distinction can be made between the actual signal and the aliased signal[1].

In order to be sure the sampling frequency is sufficiently high to capture the desired frequency components, Shannon's theorem is used. This theorem states that any continuous-time signal containing no larger frequency components than F_0 is uniquely determined by its values in equidistant points if the sampling frequency F_s is higher than $2 \cdot F_0$ [3]. $F_s/2$ is called the Nyquist frequency. This has to be taken into account when choosing the sampling frequency for wave model identification, as it should be large enough to capture the frequency range present in the wave. As higher sampling frequencies result in an increased computation time, and subsequently a slower control action response time, it is important that this frequency is not unnecessary large. For the generation of waves, Rexroth considers a spectrum with frequencies up until 5 Hz. Assuming wave reflections with the same frequency range, the sampling frequency of the ARC algorithm should be higher than 10 Hz to capture the frequencies in the wave.

Frequency Resolution The frequency resolution, and corresponding frequency bin size, of the DFT depends on the window size of the DFT[2], as given in the equation below.

---

[1] Source: https://www.researchgate.net/figure/An-example-of-aliasing-in-the-time-domain-The-two-signals-have-the-same-values-at-the-fig6-28359715

[2] Source: http://support.ircam.fr/docs/AudioSculpt/3.0/co/FFT%20Size.html

$$\text{Frequency bin size (Hz)} = \frac{1}{\text{Window size (s)}}$$

If the true frequency of a wave signal is 0.7 Hz and the bin size of the DFT is 0.25 Hz, the actual frequency will fall in between the 0.5 Hz and the 0.75 Hz points in the DFT. This corresponds with the fact that the signal is not periodic in the DFT window (in this case 4 seconds). The non-periodicity introduces discontinuities which results in additional frequency components in the DFT [6]. Energy from the true frequency will leak to neighbouring bins in the DFT, called spectral leakage. Figure 3-3 gives a graphical explanation. The left figure shows the time series of two monochromatic waves with different frequencies for the DFT window $[0, \quad 4]$ s and the right figure shows the corresponding DFTs. Both waves have an amplitude of 1m. The 1 Hz wave is periodic in the DFT window, resulting in the right frequency and amplitude in the DFT. The 0.7 Hz wave is not periodic in the DFT window, which results in energy leakage to neighbouring frequency bins in the DFT. This does not only lead into the leakage of energy to additional frequencies, but also a discrepancy in the frequency and amplitude for the dominant frequency in the DFT.

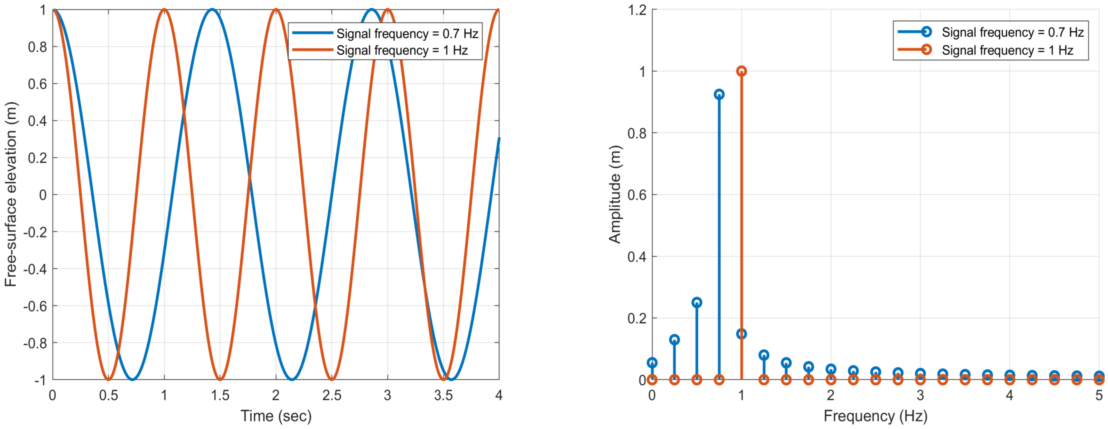

(a) Free-surface elevation time series. **(b)** DFT.

Figure 3-3: Free-surface elevation time series and DFT of two monochromatic waves with different frequencies. The figures show the effect of spectral leakage as a result of the influence of non-periodicity in the DFT window. DFT window: $[0, \quad 4]$ s.

Furthermore, the DFT resolution influences the amount of dominant frequencies detectable by the DFT. This can be graphically explained using Figure 3-4. The same DFT window size of $[0, \quad 4]$ s is considered. The left figure shows the time series of a wave consisting of a superposition of two sinusoidal components with the frequencies 0.95 Hz and 1.05 Hz and amplitudes of 1m. The corresponding DFT is visible in the figure on the right. The DFT resolution is not sufficient to make a distinction between the two frequencies, resulting them to fall in the same bin (1 Hz). This leads to one dominant frequency in the DFT, instead of two.

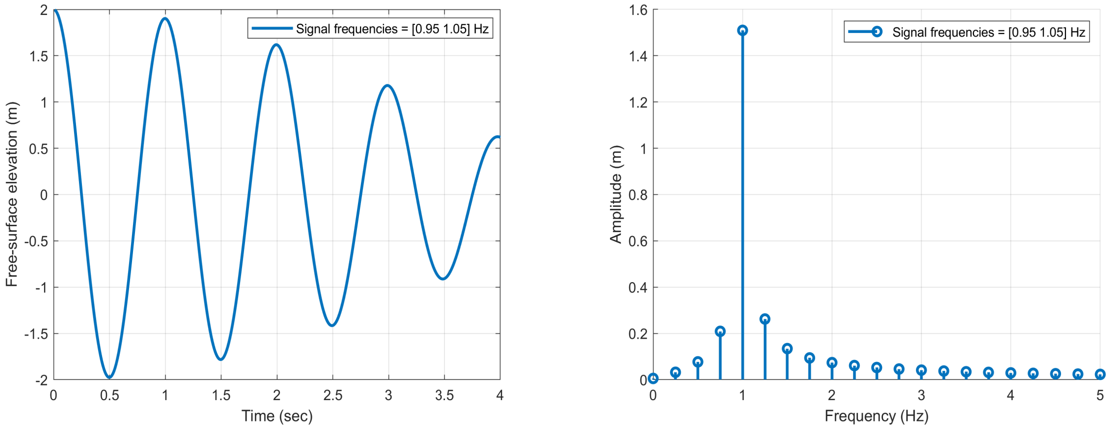

(a) Free-surface elevation time series.

(b) DFT.

Figure 3-4: Free-surface elevation time series and DFT of a wave, consisting of a superposition of two sinusoidal functions. The DFT resolution is not sufficient to make a distinction between the two frequencies in the wave signal. DFT window: $[0, \quad 4]$ s.

As actual wave spectra contain an infinite amount of frequency components, this effect leads to a wave model that contains less components than present in the actual wave. Later in the report it will become clear that this lack of components does not necessarily have to lead to a worse fit with respect to the free-surface elevation time series of the model and the actual wave.

These results show that the DFT window size determines the quality of the data provided by the DFT. This can have a strong influence on the wave identification in the early stage of the free-surface elevation time series, as the available measurement time is limited.

3-3 Linear Model

In order to compensate for the discrepancies in the data provided by the DFT, an estimation algorithm can bring a solution. The idea is to use the parameters that result from the DFT as initial values for the algorithm, which converges them towards their actual values, leading to a better fit of the wave model.

Threshold Value The amount of components included in the model depends on the amount of significant frequencies identified by DFT. Low-amplitude components will have minimal influence on the free-surface elevation and result in an unnecessary large model. Figure 3-5 shows this graphically. A threshold value determines which of these identified frequency components are included to set the basis for the model. This value will be given as a percentage of the maximal amplitude in the DFT. The left figure shows the DFT of a harmonic signal and the threshold line on 20%. The right figure shows the free-surface elevation time series of the original and the filtered wave signal, with the latter containing only the frequency components with amplitudes above the threshold line. The influence of shifting this threshold line will be covered in a next section.

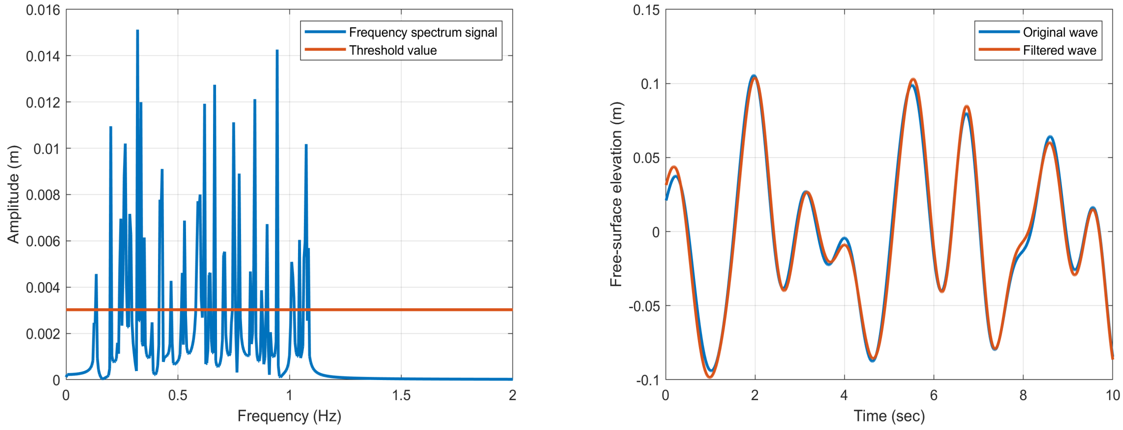

(a) DFT and threshold line.

(b) Free-surface elevation time series.

Figure 3-5: Left figure: DFT of an harmonic signal and threshold line at 20%. Right figure: the corresponding free-surface elevation time series of the original and the filtered wave signal.

Recursive Least-Squares The estimation of the angular frequency, amplitude and phase asks for a nonlinear model, due to the cosine term in Eq. (3-1). When considering only the amplitude and phase for estimation, the first order model can be written in a linear form. This linear form is based on the equality given in Eq. (3-3). The angular frequency in this equation is taken as an input. The value for this frequency results from the DFT and is not further converged by the estimation algorithm.

$$A\cos(\omega t) + B\sin(\omega t) = \sqrt{A^2+B^2}\cdot\cos(\omega t - \tan^{-1}(B/A)) \tag{3-3}$$

This linear model can be solved by a Recursive Least-Squares (RLS) algorithm. The RLS error function is described in Eq. (3-4) [8]. y_k corresponds to the free-surface elevation measurements of one segment.

$$\varepsilon(N) = (\mathrm{w}-\bar{\mathrm{w}})^T[\lambda^{-(N+1)}\Pi_0]^{-1}(\mathrm{w}-\bar{\mathrm{w}}) + \sum_{k=0}^{N}\lambda^{N-j}|y_k - u_k^T\mathrm{w}|^2 \tag{3-4}$$

With w as the optimizable vector, which can be extended according to the amount of included frequency components: $\mathrm{w} = [A_1 \quad B_1 \cdots A_M \quad B_M]^T$. $\bar{\mathrm{w}}$ is the initial guess vector and Π_0 is the weight related to it. A low value for Π_0, indicates a high certainty for the initial guesses to be close to the actual values. $u_k^T = [\cos(\omega_1 t) \qquad \sin(\omega_1 t) \qquad \cdots \qquad \cos(\omega_M t) \qquad \sin(\omega_M t)]$ is the vector with the input signals. λ is the forgetting factor, indicating the inclusion of past measurement points.

Estimation Performance In theory, if the provided frequencies by the DFT are accurate, the RLS algorithm is able to estimate the exact corresponding amplitudes and phases. But as discussed before, the quality of the data provided by the DFT depends on its window size. Figure 3-6 shows the amplitude estimation of a two-component wave, with the frequencies 0.51 Hz and 0.95 Hz. The sampling frequency F_s is 10 Hz, with a Nyquist frequency of 5 Hz more than enough to capture the two components. As the initial guesses for the parameters A_n and B_n (Eq. (3-3)) are not straightforward, the initial guess vector w for the RLS algorithm contains only zeros. The DFT window is $[0, \quad 10]$ s and the threshold value is 20%. The resulting frequencies provided by the DFT are 0.5 Hz and 1 Hz. The discrepancy of these frequencies with respect to the original frequencies can lead to a poor estimation of the rest of the wave parameters. As shown in the figure, the amplitude estimates are subject to noise and one of them deviates from its true value.

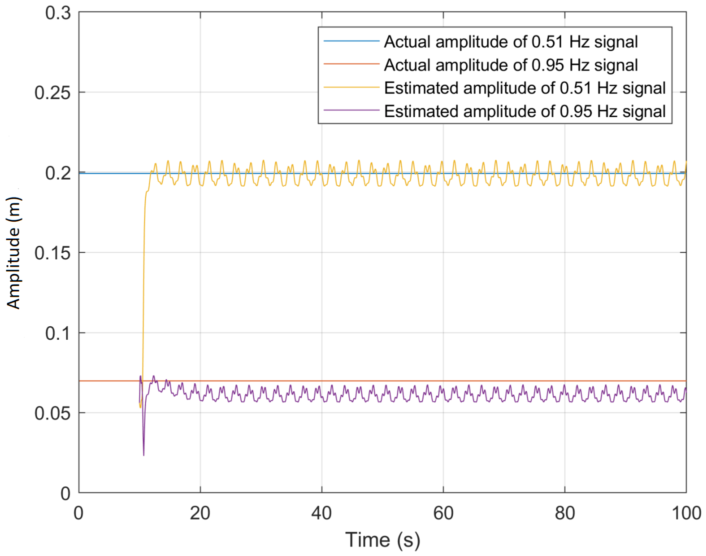

Figure 3-6: RLS amplitude estimation for a two-component wave. The frequencies are taken as input values and are not further estimated by the algorithm. True frequencies $= [0.51 \quad 0.95]$ Hz, model frequencies $= [0.5 \quad 1]$ Hz. RLS parameters: $\lambda = 0.95$, $\Pi_0 = 10$.

3-4 Nonlinear Model

As stated before, due to the nonlinearity in the wave model (Eq. (3-1)) the angular frequency can not be estimated using a linear approach. The coming section focuses on the research of the significance of a linearized approach in the form of an Extended Kalman Filter (EKF) to the convergence of the wave parameters. The EKF is chosen because of its estimation performance in the presence of (known) measurement noise. The model uncertainty matrix can be tuned to specify the reliability of the model, which can be useful to compensate for unmodeled dynamics. This is convenient when identifying the wave model, as the dynamics of actual waves will be too complex to be captured in a first order model. Although optimality can be guaranteed for the regular version of the Kalman filter, this is not the case for the EKF. The reason for this is that the EKF approximates the nonlinear model by linearization. The performance of the algorithm is based on how well the linearized model approximates the nonlinear one.

3-4-1 State-space Representation

The equation for the wave model will first be transformed into a state-space representation. A linearization in the output matrix C matrix will be used to approximate the nonlinear wave dynamics.

Continuous Time The basis of the model starts with the continuous time state-space model for each frequency component, given in Eq. (3-5).

$$\dot{\widehat{\begin{bmatrix}\varphi\\ \omega\\ a\end{bmatrix}}} = \underbrace{\begin{bmatrix}0&1&0\\0&0&0\\0&0&0\end{bmatrix}}_{A}\widehat{\begin{bmatrix}\varphi\\ \omega\\ a\end{bmatrix}} + \underbrace{\begin{bmatrix}-\hat{k}\\0\\0\end{bmatrix}}_{B}\underbrace{\dot{x}^{seg}[t]\cos(\hat{\theta}+\pi)}_{u} + \begin{bmatrix}w_{\varphi}\\ w_{\omega}\\ w_a\end{bmatrix} \tag{3-5}$$

φ is taken as the full phase term inside the brackets of the cosine (Eq. (3-1)); $\varphi = \varphi_{\text{time}} + \varphi_{\text{space}} + \varphi_{\text{fixed}}$. This state-space model contains all the necessary parameters in the state vector, except the wave angle. The wave angle can be derived separately using a least squares optimization including the wave number, resulting from the angular frequency, and the phase, without having to include θ in the state vector. This separate optimization does not have to be performed every time step, as the variability of wave angles in a real scenario is low. The estimation of the wave angle θ will be covered in a later section. w corresponds to the model uncertainty according to each state, with zero mean and covariance q: $w \sim N(0,q)$. The estimated wave angle $\hat{\theta}$ is used for the input u of the state-space model, to compensate for the phase difference corresponding to the movement of the segments.

Discrete Time The discrete state-space model is given in Eq. (3-6). The discretization of the continuous time model is based on the method in section *1.11.1* of [5]. With T_s as the sampling time.

$$\widehat{\begin{bmatrix}\varphi\\ \omega\\ a\end{bmatrix}}_{k+1} = \underbrace{\begin{bmatrix}1&T_s&0\\0&1&0\\0&0&1\end{bmatrix}}_{A_k}\widehat{\begin{bmatrix}\varphi\\ \omega\\ a\end{bmatrix}}_{k} + \underbrace{\begin{bmatrix}-\hat{k}_k\\0\\0\end{bmatrix}}_{B_k}\underbrace{(x^{seg}_{k+1}-x^{seg}_{k})\cos(\hat{\theta}_k+\pi)}_{u_k} + \begin{bmatrix}w_{\varphi}\\ w_{\omega}\\ w_a\end{bmatrix} \tag{3-6}$$

When dealing with multiple components the model can easily be extended, as shown in Eq. (3-7). As the basis of the model is set by the data provided by the DFT, the amount of frequency components included in the wave model depends on the frequency resolution of the DFT and the threshold value. For the simulations performed in this research, the wave angle is considered to be equal for all the frequency components in the reflected wave.

$$\widehat{\begin{bmatrix}\varphi_1\\ \omega_1\\ a_1\\ \vdots\\ \varphi_M\\ \omega_M\\ a_M\end{bmatrix}}_{k+1} = \begin{bmatrix}A_k&&\\&\ddots&\\&&A_k\end{bmatrix}\widehat{\begin{bmatrix}\varphi_1\\ \omega_1\\ a_1\\ \vdots\\ \varphi_M\\ \omega_M\\ a_M\end{bmatrix}}_{k} + \begin{bmatrix}-\hat{k}^1_k\\0\\0\\ \vdots\\ -|\hat{k}^M_k|\\0\\0\end{bmatrix}(x^{seg}_{k+1}-x^{seg}_{k})\cos(\hat{\theta}_k+\pi) + \begin{bmatrix}w_{\varphi,1}\\ \vdots\\ w_{a,M}\end{bmatrix} \tag{3-7}$$

As the measured wave height is a nonlinear function of the states, this results in a nonlinear output equation, given in Eq. (3-8) according to the measurements of a single segment. With $\hat{x}_k$ referring to the states of the state space model (Eq. (3-6)). Note that this equation does not directly depend on the angular frequency ω_n, but only indirectly through the phase term φ_n. The Jacobian of the nonlinear function $h(\hat{x}_k)$ is used to obtain the linearized discrete output matrix C_k, given in Eq. (3-9). A measurement noise v_k is considered, with zero mean and covariance R_k: $v_k \sim N(0, R_k)$.

$$\hat{y}_k = \underbrace{\sum_n \hat{a}_n^k \cos(\hat{\varphi}_n^k)}_{h(\hat{x}_k)} \tag{3-8}$$

$$C_k = \begin{bmatrix} \frac{\partial \hat{y}}{\partial \hat{\varphi}_1} & 0 & \frac{\partial \hat{y}}{\partial \hat{a}_1} & \cdots & \frac{\partial \hat{y}}{\partial \hat{\varphi}_M} & 0 & \frac{\partial \hat{y}}{\partial \hat{a}_M} \end{bmatrix}_k \tag{3-9}$$

3-4-2 Kalman Filter Equations

Eq. (3-10) shows the equations for the EKF, based on [4]. The Q_k and R_k matrices are the model uncertainty covariance and the measurement noise covariance matrices respectively. K_k is the Kalman gain and P_k the state covariance matrix. The superscript $^-$ refers to the a priori estimate of the state vector $\hat{x}_k$ and the state covariance matrix P_k. The a posteriori estimates are denoted without a superscript. The algorithm consists of a two-step process; The prediction update step produces predictions of the state. These predictions are later updated in the measurement step, with the use of a weighted average between the measured output and the model predicted output. Depending on the values for the matrices Q_k and R_k, more weight is given to the output with higher certainty.

Prediction Update *Measurement Update*

$$\begin{aligned} \hat{x}_k^- &= A_k \hat{x}_{k-1} + B_{k-1} u_k & K_k &= (P_k^- C_k^T)(C_k P_k^- C_k^T + R_k)^{-1} \\ P_k^- &= A_k P_{k-1} A_k^T + Q_k & \hat{x}_k &= \hat{x}_k^- + K_k(y_k - h(\hat{x}_k^-)) \\ & & P_k &= (I - K_k C_k) P_k^- \end{aligned} \tag{3-10}$$

Nonzero values will only be assigned to the diagonal values of the matrices Q and P as their influence is more straightforward. Eq. (3-11) shows the continuous-time version of the two matrices.

$$Q = \begin{bmatrix} q_\varphi & 0 & 0 \\ 0 & q_\omega & 0 \\ 0 & 0 & q_a \end{bmatrix} \qquad P = \begin{bmatrix} p_\varphi & 0 & 0 \\ 0 & p_\omega & 0 \\ 0 & 0 & p_a \end{bmatrix} \tag{3-11}$$

The discrete time matrix Q_k (Eq. (3-12)) can be derived using the method described in [5]. The state covariance matrix P remains the same in discrete time ($P_k = P$).

$$Q_k = \begin{bmatrix} q_\varphi \cdot T_s + \frac{q_\omega \cdot T_s^3}{3} & \frac{q_\omega \cdot T_s^2}{2} & 0 \\ \frac{q_\omega \cdot T_s^2}{2} & q_\omega \cdot T_s & 0 \\ 0 & 0 & q_a \cdot T_s \end{bmatrix} \tag{3-12}$$

3-4-3 Estimation Results

In this paragraph the contribution of the EKF on the wave parameter convergence will be evaluated. The identification will first be performed on a simple two-component wave and subsequently on a more complex 50-component wave.

Setup This section only the considers the identification part of the algorithm, as the identified wave model will not be transferred to segment displacements yet. Figure 3-7 shows a schematic representation of the wave model identification part for a single segment.

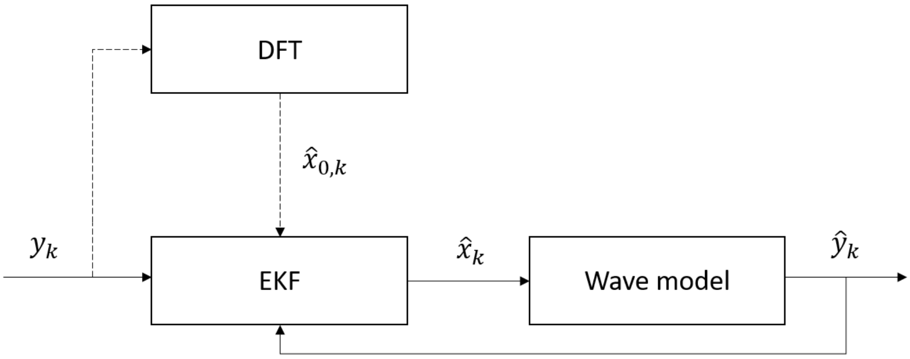

Figure 3-7: Schematic representation of wave identification part of the ARC.

y_k corresponds to the reflected wave height measurements, and $\hat{y}_k$ to the estimated wave heights by the model. $\hat{x}_k$ refers to the wave parameters and $\hat{x}_{0,k}$ to their initial values provided by the DFT. The dashed line indicates that the parameter initialization by the DFT will not be performed every time step, as the EKF needs time to estimate the true values of the parameters. As more measurement data becomes available, more accurate DFT parameters can be provided to re-initialize the wave model at a later moment in time. The window sizes of these DFTs can be adjusted for each simulation. The identification process starts as soon as the first DFT has been performed.

The parameter values for these simulated waves are randomly created in MATLAB. Table 3-1 shows the intervals from which the random parameter values are chosen. The resulting frequency components are superposed to form a first order approximation of the wave. The estimation of the wave angle is not included and will be elaborated in a next section. For now, only perpendicular waves are considered, so $\theta_n = 0$. As covered before, the wave number k results from the dispersion relation.

Parameter	Interval
ω_n	[0.1, 2π] rad/s
a_n	[0.1, 1.2] m
φ^n_{fixed}	[-π, π] rad

Table 3-1: Intervals for the randomly created parameters of the reflected wave.

The maximum angular frequencies in the interval corresponds to a frequency of 1 Hz. For this reason, a sampling frequency of 10 Hz will suffice to capture the frequency components in the wave. DFTs are performed on certain fixed moments in time, referred to as t_{DFT}.

Two-component Wave For this wave, only one DFT is performed: $t_{DFT} = 10$ s, with the window $[0, \quad t_{DFT}]$ s. Figure 3-8 shows the performance of the angular frequency estimation for one wave height sensor. The initial parameter values provided by the DFT are not accurate, but the EKF manages to converge them towards their actual values. The values for the algorithm are taken as mentioned in the caption of the figure. The values for Q and P correspond to the diagonal values for the continuous time matrices: $[q_\varphi \quad q_\omega \quad q_a]$ and $[p_\varphi \quad p_\omega \quad p_a]$

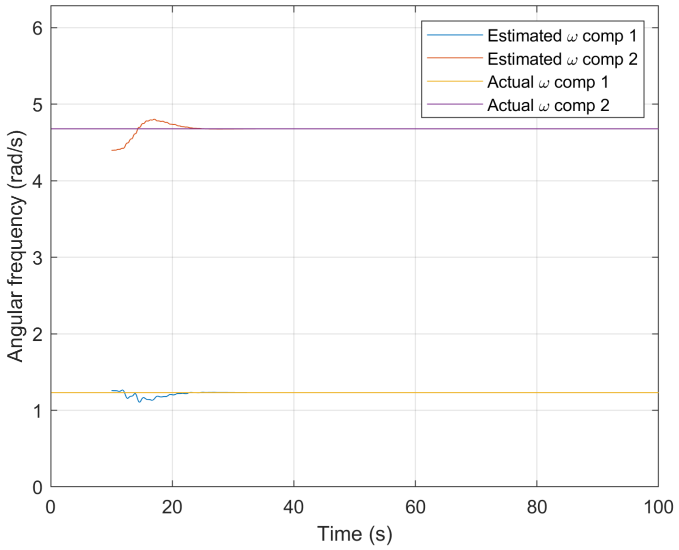

Figure 3-8: Angular frequency estimation results for a two-component wave. Diagonal values Q: $[1 \quad 0.1 \quad 0.1]$, diagonal values P: $[1 \quad 0.01 \quad 0.01]$, $R = 0$. $F_s = 10$ Hz. $t_{DFT} = 10$ s, DFT window: $[0, \quad t_{DFT}]$ s, threshold $= 20\%$.

Also the errors of the amplitudes and phases are compensated by the EKF, as shown in the estimation results in Figure 3-9. The phase terms in the figure correspond to the stationary terms, obtained by subtracting the time-dependent phase from the total phase term; $\varphi - \varphi_{time}$.

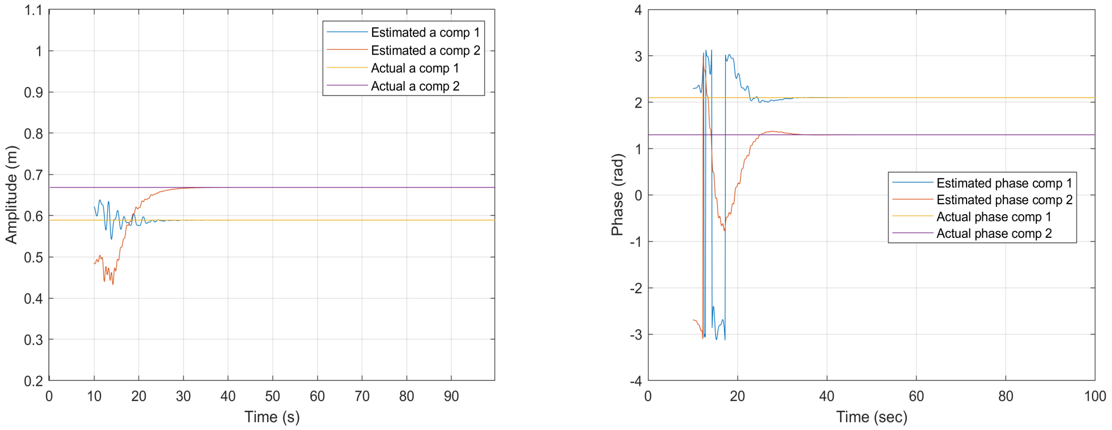

(a) **(b)**

Figure 3-9: Amplitude (a) and stationary phase (b) estimation results for a two-component wave. Diagonal values Q: $[1 \quad 0.1 \quad 0.1]$, diagonal values P: $[1 \quad 0.01 \quad 0.01]$, $R = 0$. $F_s = 10$ Hz. $t_{DFT} = 10$ s, DFT window: $[0, \quad t_{DFT}]$ s, threshold $= 20\%$.

The linearized approach has the possibility to compensate for slight discrepancies in the angular frequencies provided by the DFT. This led to the choice of an EKF for the wave parameter estimation in the proposed algorithm.

50-component Wave To analyse the performance for more complex waves, the algorithm is used for a 50-component wave. The wave parameters for each of the components are again randomly selected from the intervals described in Table 3-1. The length of the free-surface elevation time series of the simulated wave is set on 500 s. The estimation results for the parameters are shown in Figures 3-10 and 3-11. The figure only shows the stationary phase terms of the first two components, which are wrapped around 2π. DFTs are performed for certain fixed moments in time and are indicated by the green lines in the figure: $t_{DFT} = [1 \quad 5 \quad 20 \quad 50 \quad 100 \quad 200 \quad 400]$. The DFT windows contain all the wave height measurement up until that moment: $[0, \quad t_{DFT}]$. The use of multiple DFTs with different window sizes creates insight into the importance of the DFT resolution to the wave identification. DFTs performed at a later moment in time are able to detect more frequency components, as a larger DFT window results in a higher DFT frequency resolution. This means that on those time steps the model will be resized, corresponding to the amount of significant frequency components from the DFT, and initialized with the corresponding parameter values.

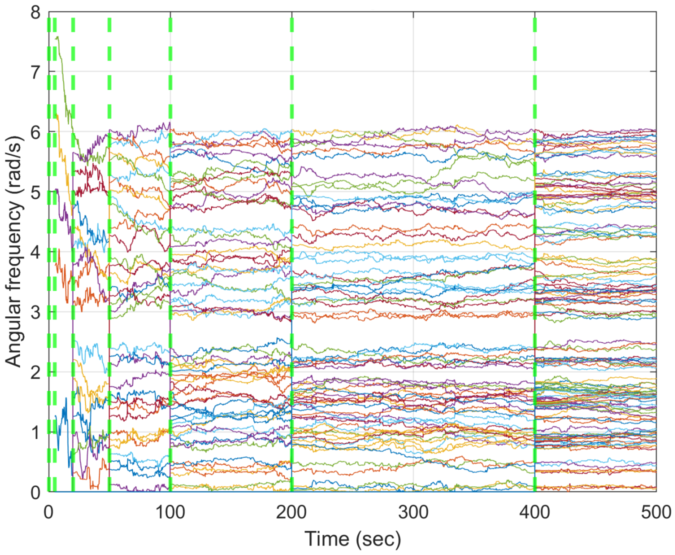

Figure 3-10: Angular frequency estimation results for a 50-component wave. Diagonal values Q: $[1 \quad 0.1 \quad 0.1]$, diagonal values P: $[1 \quad 0.01 \quad 0.01]$, $R = 0$, $F_s = 10$ Hz, threshold $= 10\%$, DFT times (green lines): $[1 \quad 5 \quad 20 \quad 50 \quad 100 \quad 200 \quad 400]$ s, DFT window sizes: $[0, \quad t_{DFT}]$ s.

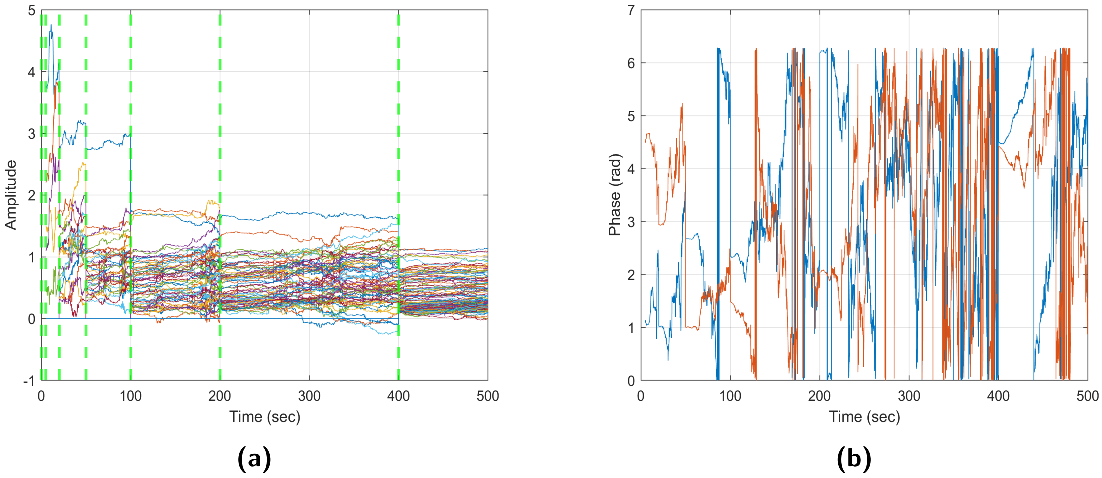

(a) **(b)**

Figure 3-11: Amplitude and stationary phase estimation results for a 50-component wave. Diagonal values Q: $[1 \quad 0.1 \quad 0.1]$, diagonal values P: $[1 \quad 0.01 \quad 0.01]$, $R = 0$, $F_s = 10$ Hz, threshold $= 10\%$, DFT times (green lines in figure (a)): $[1 \quad 5 \quad 20 \quad 50 \quad 100 \quad 200 \quad 400]$ s, DFT windows: $[0, \quad t_{DFT}]$ s.

Note that some of the estimated amplitudes take negative values. This is possible as no bounds are defined for the EKF. A negatively signed frequency component corresponds to the same positively signed component by a phase difference of π. Components with negative amplitudes will not form a problem for the wave model identification. The estimated variables seem to contain quite some noise. Especially the phase term contains a lot of noise, possibly due to the higher co-variance for the phase term compared to the other two states. The figures show that, for the amplitude and frequency estimation, the noise decreases as the window size of the DFT increases. This can be explained by more accurate parameter values and a larger amount of detected components by the DFT. A deficiency of components in the model leads to noisy wave parameters, as they try to compensate for the unmodeled components. Altering the values for the model uncertainty matrix Q and co-variance matrix P did not result in decreased estimation noise. This indicates that the main factor behind this noise is the mismatch between the amount of components in the model and the actual wave.

3-5 Wave Prediction

This section discusses the performance of the reflected wave prediction of the model. Wave prediction can be useful to compensate for the lag of the segment displacement response. By transferring the predicted wave heights to predicted segment displacements, the segment motion can be performed on exactly the right moment in the future. Even more, when comparing the predicted wave to the actual reflected wave it is easier to draw conclusions about the accuracy of the estimated parameters. An accurate real-time fit of the model does not guarantee a good convergence of the wave parameters, as different sets of values can lead to the same free-surface elevation at that moment. If the predicted wave height is still equal to the corresponding actual reflected wave height in the future, it indicates a reliable estimation.

3-5-1 Prediction Equation

To create predicted free-surface elevations Eq. (3-13) is used. This simple equation uses an extra term compared to the estimated wave height, introducing T_{pred} as the prediction horizon.

$$\hat{y}^k_{pred} = \sum_n \hat{a}^k_n \cos(\hat{\varphi}^k_n + T_{pred} \cdot \hat{\omega}_n) \tag{3-13}$$

3-5-2 Prediction Results

In order to check whether the prediction algorithm works properly, it will first be used for a simple two-component reflected wave. After that a 50 component wave will be analyzed to create more insight into the performance. The only difference with the setup described in Figure 3-7 is that the output of the model gives the predicted wave heights instead of the real-time wave heights. The wave parameters for the reflected wave are randomly selected from the intervals given in Table 3-1.

Two-component Wave Figure 3-12 shows the prediction results of the same two-component wave as shown in the previous section (Figure 3-9). For comparison, the predicted free-surface elevation time series is shifted manually in time, so it corresponds exactly with the actual free-surface elevation at that time in the future. The parameters for the algorithm are as given in the caption of the figure. The result shows that when the wave parameters converge towards their true values, the prediction for the reflected wave is equal to the actual reflected wave. From this result it can be concluded that the prediction algorithm works properly.

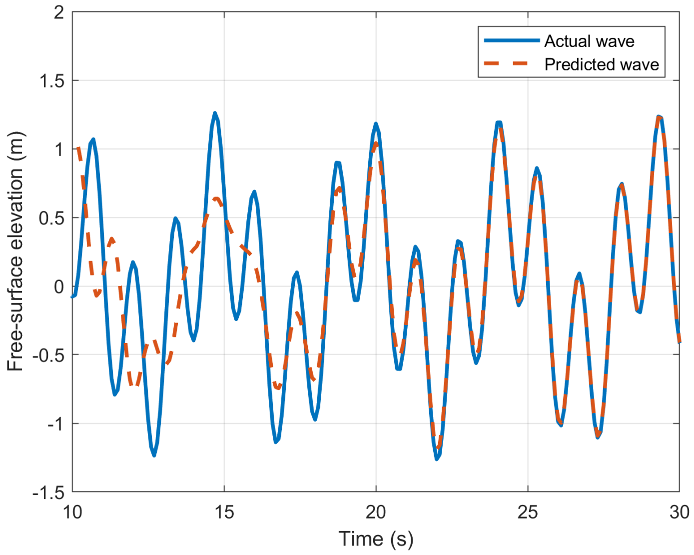

Figure 3-12: Snapshot of the wave prediction results for a two-component wave (Figure 3-8. Diagonal values Q: $[1 \quad 0.1 \quad 0.1]$, diagonal values P: $[1 \quad 0.01 \quad 0.01]$, $R = 0$. $F_s = 10$ Hz. $t_{DFT} = 10$ s, DFT window: $[0, \quad t_{DFT}]$ s, threshold $= 20\%$, $T_{pred} = 0.2$ s.

50-component Wave Figure 3-13 shows a snapshot of the prediction performance of the more complex reflected wave as used in Figure 3-11.

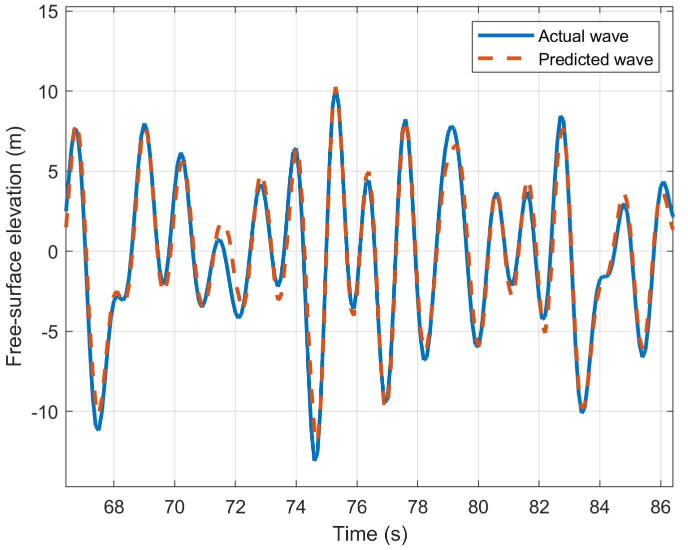

Figure 3-13: Snapshot of the wave prediction results for a 50-component wave. Diagonal values Q: $[1 \quad 0.1 \quad 0.1]$, diagonal values P: $[1 \quad 0.01 \quad 0.01]$, $R = 0$, $F_s = 10$ Hz, threshold $= 10\%$, DFT times (green lines): $[1 \quad 5 \quad 20 \quad 50 \quad 100 \quad 200 \quad 400]$ s, DFT window sizes: $[0, \quad t_{DFT}]$ s, $T_{pred} = 0.2$ s.

It is difficult to draw conclusions about the prediction performance by just looking at the free-surface elevation time series. Table 3-2 shows the Root Mean Square (RMS) values of the error between the predicted wave heights and the actual reflected wave heights, for the time intervals between the DFTs. The increasing window size of the DFTs leads to more accurate wave parameters and subsequently a better prediction performance.

Interval (s)	5-20	20-50	50-100	100-200	200-400	400-500
RMS error	2.008	1.534	0.857	0.795	0.604	0.568

Table 3-2: RMS errors for according to the time intervals between the DFTs, corresponding to the free-surface elevation time series in Figure 3-13.

To investigate the contribution of the EKF to the wave identification, the same 50-component wave is now estimated using just the wave data provided by the DFTs. The wave parameters provided by the DFTs are directly incorporated in the first order wave model (Eq. (3-1)), and not further converged by the EKF. Figure 3-14 gives a schematic representation of the setup.

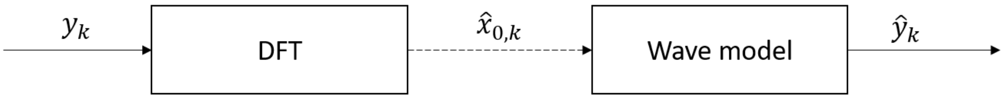

Figure 3-14: Schematic representation of the wave identification based on just the wave parameters provided by the DFT.

The DFTs are performed every 5 s of the measured free-surface elevation time series ($t_{DFT} = [5 \quad 10 \quad \cdots \quad 495]$ s). The corresponding DFT windows are: $[0, \quad t_{DFT}]$ s. The time intervals between the DFTs has been reduced to show that, even if the wave model is re-initialized more frequently, the predicted wave height shows a poor fit without the parameter convergence by the EKF. A snapshot of the predicted free-surface elevation time series is shown in Figure 3-15.

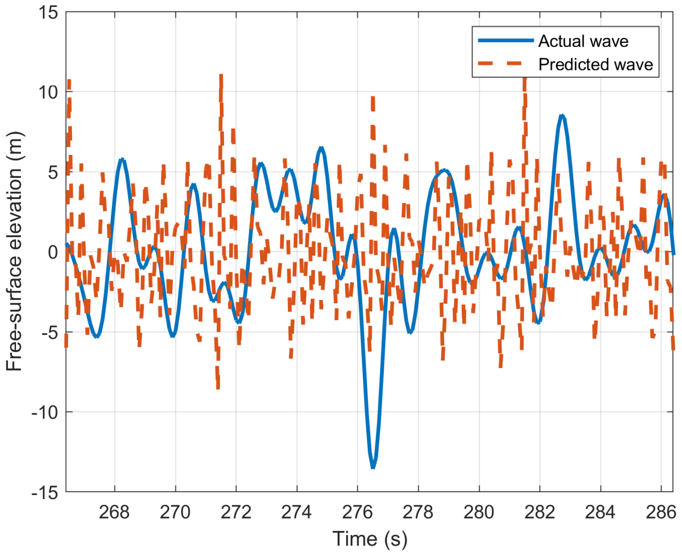

Figure 3-15: Snapshot of the prediction results for the 50-component wave, just based on the wave parameters provided by the DFTs. $F_s = 10$ Hz, Threshold $= 10\%$, $T_{pred} = 0.2$ s.

Table 3-3 shows the RMS errors between the predicted and actual time series, corresponding to the same time intervals as in Table 3-2. From the free-surface elevation time series in Figure 3-15 and the RMS errors in Table 3-3 it can be concluded that the EKF has a substantial contribution to the identification of the wave model. The RMS errors for the specified time intervals are not only larger, but they also do not decrease as more accurate wave parameters are provided by DFTs performed later in time.

Interval (s)	5-20	20-50	50-100	100-200	200-400	400-500
RMS error	4.853	4.824	5.210	5.241	5.048	5.094

Table 3-3: RMS errors for according to the same time intervals as in Table 3-2, corresponding to the free-surface elevation time series in Figure 3-15.

3-6 Wave Angle Estimation

As discussed in an earlier section, accurate knowledge of the reflected wave angle can be very useful for a good absorption strategy. To extract wave angle information from the estimated parameters, wave height measurement are needed from multiple segments. The wave angle can be estimated by determining the difference in phase from one spatial measurement point to another. This leads to a slight adjustment in the state-space model described in Eq. (3-5).

3-6-1 Adjusted State-space Representation

Eq. (3-14) gives the adjusted state-space model. For each frequency component the state vector includes the phase term φ_2 according to the measurements of a neighbouring segment.

Considering the measurements of two segments is enough to estimate the wave angle. This is convenient as every segment, including the ones at the end of the line, has at least one neighbouring segment. The neighbouring segment on the right is considered for most of the segments, and the left neighbouring segment for the one at the right end of the line. The amplitude and angular frequency in the state vector should theoretically be equal for the two spatial measurement points but, in the case of oblique waves, the wave angle results in a phase difference as one of the segments senses the reflected wave first. This estimated phase difference can be used to extract information about the wave angle.

$$\widehat{\begin{bmatrix} \varphi_1 \\ \varphi_2 \\ \omega \\ a \end{bmatrix}}_{k+1} = \begin{bmatrix} 1 & 0 & T_s & 0 \\ 0 & 1 & T_s & 0 \\ 0 & 0 & 1 & 0 \\ 0 & 0 & 0 & 1 \end{bmatrix} \widehat{\begin{bmatrix} \varphi_1 \\ \varphi_2 \\ \omega \\ a \end{bmatrix}}_{k} + \begin{bmatrix} -\hat{k}_k & 0 \\ 0 & -\hat{k}_k \\ 0 & 0 \\ 0 & 0 \end{bmatrix} \begin{bmatrix} (x^{seg}_{k+1,1} - x^{seg}_{k,1}) \cos(\hat{\theta}_k + \pi) \\ (x^{seg}_{k+1,2} - x^{seg}_{k,2}) \cos(\hat{\theta}_k + \pi) \end{bmatrix} + \begin{bmatrix} w_{\varphi_1} \\ w_{\varphi_2} \\ w_{\omega} \\ w_a \end{bmatrix} \tag{3-14}$$

For more components, the model can again be extended as described in Eq. (3-7). As the output of the neighbouring segment has to be taken into account, the new output equations and C_k matrix are shown in Eq. (3-15) and Eq. (3-16) respectively.

$$\begin{bmatrix} \hat{y}_1 \\ \hat{y}_2 \end{bmatrix}_k = \begin{bmatrix} \sum_n \hat{a}_n \cos(\hat{\varphi}_{1_n}) \\ \sum_n \hat{a}_n \cos(\hat{\varphi}_{2_n}) \end{bmatrix}_k \tag{3-15}$$

$$C_k = \begin{bmatrix} \frac{\partial \hat{y}_1}{\partial \hat{\varphi}_1^1} & 0 & 0 & \frac{\partial \hat{y}_1}{\partial \hat{a}_1} & \cdots & \frac{\partial \hat{y}_M}{\partial \hat{\varphi}_1^M} & 0 & 0 & \frac{\partial \hat{y}_1}{\partial \hat{a}_M} \\ 0 & \frac{\partial \hat{y}_2}{\partial \hat{\varphi}_2^1} & 0 & \frac{\partial \hat{y}_2}{\partial \hat{a}_1} & \cdots & 0 & \frac{\partial \hat{y}_2}{\partial \hat{\varphi}_2^M} & 0 & \frac{\partial \hat{y}_2}{\partial \hat{a}_M} \end{bmatrix} \tag{3-16}$$

3-6-2 Nonlinear Least Squares Optimization

As discussed before, φ consists of three separate phase terms, given in Eq. (3-17) according the measurements of one segment i. The subscripts k and n are omitted for convenience.

$$\varphi_i = \underbrace{\omega \cdot t}_{\varphi_{\text{time}}} + \underbrace{k(x_i^{seg} \cos(\theta + \pi) + y_i^{seg} \sin(\theta + \pi))}_{\varphi_{\text{space}_i}} + \underbrace{\phi}_{\varphi_{\text{fixed}}} \tag{3-17}$$

Note that the only difference with φ_{i+1} is the spatial part of the phase term φ_{space_i}. When calculating the difference $\varphi_{i+1} - \varphi_i$, the time dependent phase term φ_{time} and the fixed phase term φ_{fixed} drop. The remaining term is responsible for the phase difference due to the propagation angle of the wave. The estimated wave angle results from a Nonlinear Least Squares (NLS) method, fitting the difference in the spatial terms to the difference of the full phase terms, given in Eq. (3-18) according to one frequency component. As stated before, this optimization does not have to be performed for every time step. The time interval between the NLS optimizations can be adjusted according to the variability of the wave angle.

$$\hat{\theta} = \arg\min_{\theta} \left\| \left[\hat{\varphi}_i - \hat{\varphi}_{i+1} \right] - \left[\hat{\varphi}_{space_i}(\theta) - \hat{\varphi}_{space_{i+1}}(\theta) \right] \right\|^2 \tag{3-18}$$

$$\hat{\varphi}_{space_i}(\theta) = \hat{k}(x_i^{seg} \cos(\theta + \pi) + y_i^{seg} \sin(\theta + \pi)) \tag{3-19}$$

Equation (3-19) shows the estimate for φ_{space} including the optimizable wave angle θ. The estimate for the wave number k results from the estimated angular frequency $\hat{\omega}$ (EKF) according the dispersion relation. When assuming a single propagation angle for all the frequency components in the reflected wave, the wave parameters of multiple components can be used in the NLS equation to estimate a single wave angle.

Unique Solution For a reliable phase difference between neighbouring segments, the wave length of the component should be larger than the difference between the spatial measurement points. If this is not the case there will not be a unique solution, as there is no indication whether the wave has already completed a period before arrival at the next segment. Example: the width for each segment is 0.5 m. A frequency component with a wavelength $\lambda = 0.25$ m has zero phase lag, measured from segment i to segment $i+1$. This can either indicate that the wave angle is $\theta = 0°$, or the wave has already completed exactly one cycle before arrival at the next segment. In this case the wave angle would be $\theta = 45°$.

Not only the minimal wave length is important, but the combination with a maximal assumed propagation angle forms the constraint to guarantee a unique solution of the wave angle and its main direction (positive or negative with respect to the perpendicular line). This becomes clear when looking at the following example. Let's say the estimated phases according to two neighbouring segments are as follows.

$$\text{Segment 1: } \hat{\varphi}_k = \frac{\pi}{2}$$

$$\text{Segment 2: } \hat{\varphi}_k = \frac{5\pi}{4}$$

As the phases of sinusoidal functions are wrapped around 2π, the given phases are the remainders from the total estimated phase, after a division by 2π. This can either mean that the wave arrives at segment 1 first and arrives at segment 2 with a delay of $\frac{3\pi}{4}$. Or the wave could have arrived at segment 2 first and then at segment 1 with a delay of $\frac{5\pi}{4}$. This increased lag would indicate a larger propagation angle and an opposite wave direction than for the first option. Constraints can be implemented considering a minimum wave length for the component to be considered for wave angle estimation. Together with an assumption for a maximum wave angle the largest possible phase difference can be reduced to π. This leaves just a single possible propagation direction as one of the two options in the example drops. According to Rexroth, the maximum angle of reflected waves can be assumed to be 45°, as reflective waves are unlikely to come in with angles larger than that. Considering a distance between the measurement points of 0.5 m, the minimum wave length required for angle estimation is 0.5 m in order to guarantee a maximum delay of π.

3-6-3 Wave Angle Estimation Results

Two-component Wave The wave angle estimation will first be performed on a two-component reflected wave. The wave parameters are randomly from the intervals in Table 3-1. In addition, a random wave angle θ is picked from the interval $[-45°, \quad 45°]$, or in rad: $[-\frac{\pi}{4}, \quad \frac{\pi}{4}]$. The same wave angle is considered for all frequency components present in the reflected wave. All components in the model with estimated wave lengths larger than 0.5 m are considered for the wave angle optimization. The time interval between the optimizations is set on 5 s.

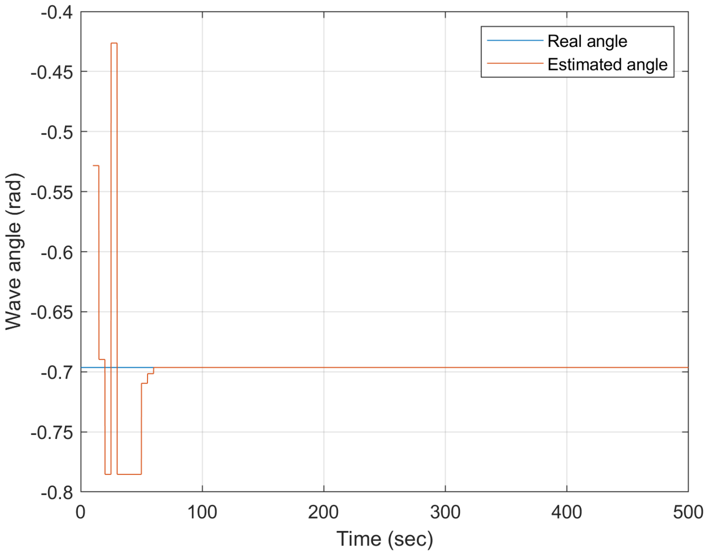

Figure 3-16: Wave angle estimation results for a two-component wave. Diagonal values Q: $[1 \quad 0.1 \quad 0.1]$, diagonal values P: $[1 \quad 0.01 \quad 0.01]$, $R = 0$. $F_s = 10$ Hz. $t_{DFT} = 10$ s, DFT window: $[0, \quad t_{DFT}]$ s, threshold $= 20\%$, wave angle optimization interval: 5 s.

For the case of the two-component wave the propagation angle is exactly identified after around 60 seconds. Although the wave angle estimation works properly, the estimation is slow considering the simplicity of this wave.

50-component wave Considering the same intervals for the randomly chosen wave parameters (Table 3-1), a 50-component wave is created. The wave angle estimation results for this wave are shown in Figure 3-17. Unlike the case for the simpler wave, the estimated wave angle does not come near its actual value. The nonlinearity of Eq. (3-18) might cause the estimate to get stuck in a local minimum. A grid search provides more insight into the NLS process. Figure 3-18 shows the possible values for θ on the x-axis and the NLS residual, based on the objective function in Eq. (3-18), on the y-axis. The wave parameters used for the objective function are the EKF estimates after 500 s.

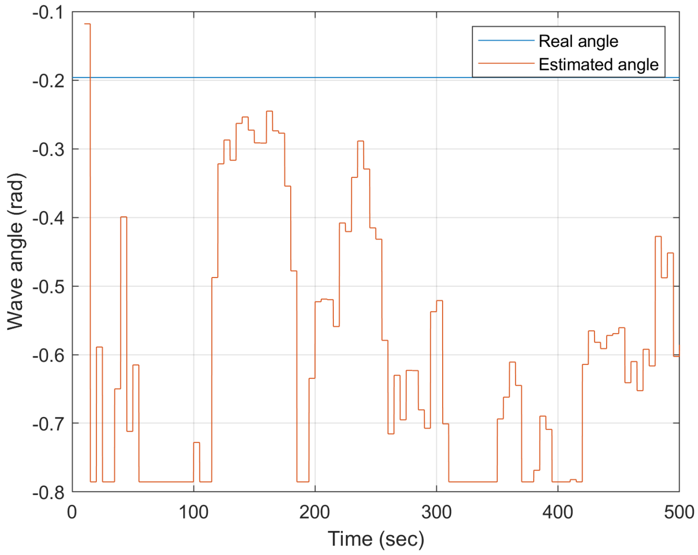

Figure 3-17: Wave angle estimation results for a 50-component wave. Diagonal values Q: $[1 \quad 0.1 \quad 0.1]$, diagonal values P: $[0.001 \quad 0.01 \quad 0.01]$, $R = 0$. $F_s = 10$ Hz. $t_{DFT} = [1 \quad 5 \quad 20 \quad 50 \quad 100 \quad 200 \quad 400]$ s, DFT windows: $[0, \quad t_{DFT}]$ s, threshold $= 10\%$, wave angle optimization interval: 5 s.

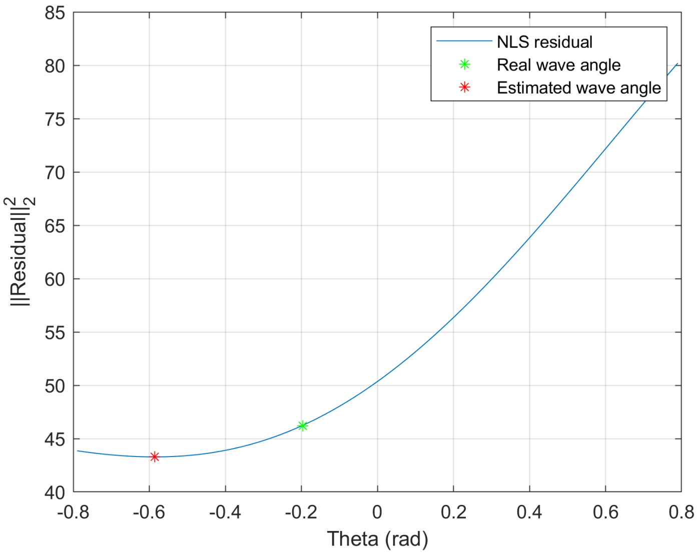

Figure 3-18: NLS Grid search for wave angle estimation (Figure 3-17). All possible values for optimizable wave angle θ and corresponding residuals. Based on the estimated wave parameters for the 50-component wave at 500 seconds.

The actual wave angle does not correspond with the minimum in the residual line. Even more, the minimum residual value is 43 instead of an expected value around zero. These two observations indicate that the input information of the NLS forms the problem, instead of the NLS process itself. Figure 3-11 showed that the estimation phases contain a lot of noise.

Disturbed phase estimates form a problem for the wave angle estimation as the NLS algorithm can only extract accurate wave angle information as the phase difference for a component from segment i to segment $i+1$ is accurate as well. Tuning the values for matrices Q and P might reduce the noise. Figure 3-19 shows the results of the phase estimation for one component, according to two neighbouring segments.

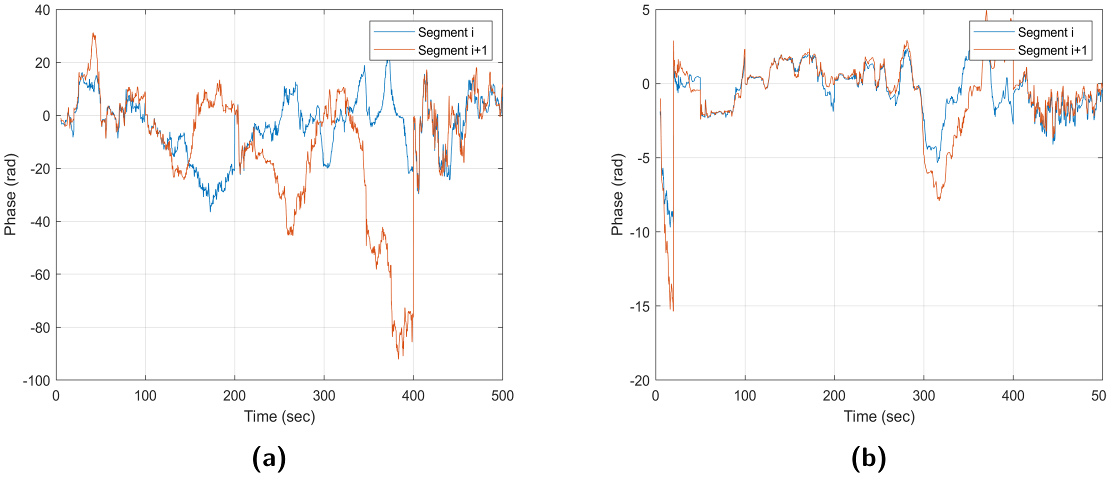

Figure 3-19: Phase estimation results for a 50-component wave. Threshold $= 10\%$, $F_s = 10$ Hz, $R = 0$. (a) $q_\varphi = 1$, $p_\varphi = 0.001$ (b) $q_\varphi = 100$, $p_\varphi = 1$.

After tuning the parameters for the matrices Q and P (Figure 3-19 b) the noise is reduced. The phase difference in particular seems to be more steady, as the phase of one component estimated from different measurement points show a similar pattern. This is a positive sign, as for the wave angle estimation the difference between the phases is particularly important. Figure 3-20 shows that the wave angle estimation still performs poorly despite the decreased noise for the estimated phases.

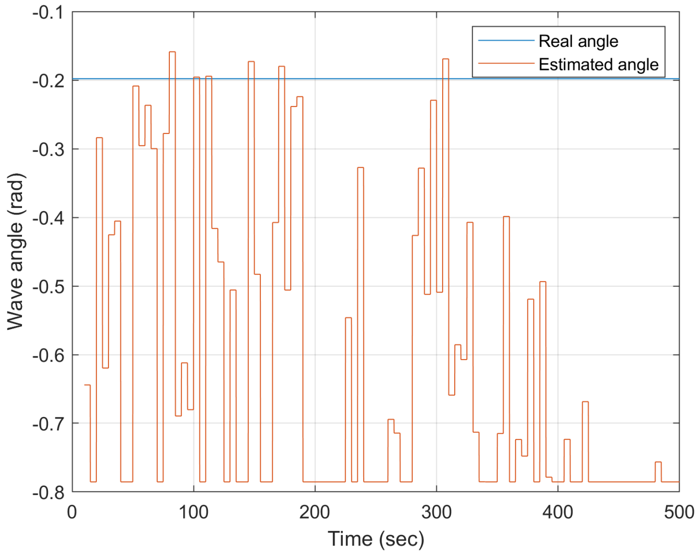

Figure 3-20: Wave angle estimation results for the same wave as in Figure 3-17. Altered values: $q_\varphi = 100$, $p_\varphi = 1$

3-6-4 Wave Angle Estimation Based on DFT

As discussed before, the difference in estimated phase terms measured from one segment to the other is important for the wave angle estimation. The EKF converges the wave parameters resulting from the DFT, leading to a much improved fit for the estimated free-surface elevation time series. Nonetheless, the unmodeled dynamics introduce a noisy behaviour, causing the phase terms to get unreliable. This section discusses wave estimation based on the phase terms provided by the DFT, before they are processed by the EKF. Figure 3-21 (a) shows the free-surface elevation time series of a monochromatic wave measured by two neighbouring segments. The time series show a slight phase difference due to the propagation angle of the wave. Figure 3-21 (b) shows the true stationary phase terms for both the free-surface elevation time series ($\varphi - \varphi_{time}$). These stationary phase terms according to the DFTs, performed by the two neighbouring segments, are shown in red. The time window of the DFT is $[0, \quad 10]$ s.

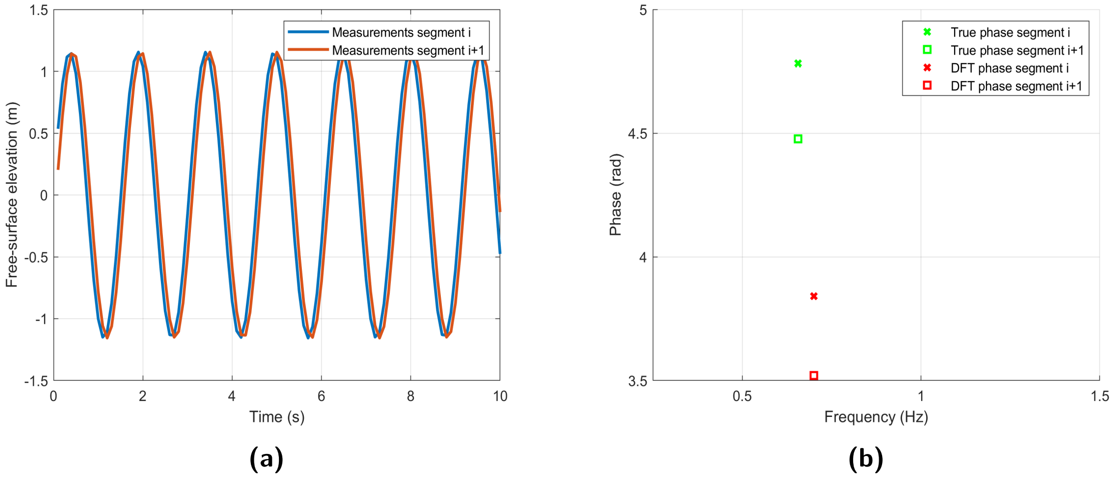

Figure 3-21: (a) Free-surface elevation time series of a monochromatic oblique wave measured by two neighbouring segments. (b) Actual stationary phase terms of time series in green and DFT phase terms in red.

The phase terms according to the DFT show mismatches regarding their true values. There are discrepancies in both the frequency and the phase. But interestingly, the two pairs seem to have an almost equal distance between each other. This looks promising for wave angle estimation as their phase difference is used, rather than their actual values. This method would not need the extended model described in Section 3-6-1 but directly uses the wave parameters provided by the DFT, before they are processed by the EKF. The algorithm looks for matching frequencies detected by the DFTs of two neighbouring segments and uses the provided wave parameters for the NLS optimization (Section 3-6-2), as long as the wave length is large enough and the components have equally signed amplitudes. All the qualifying frequency components are used to estimate a single wave angle. The wave numbers $\hat{k}$ in the NLS equation depends on the corresponding detected frequencies. Although the provided DFT parameters are not completely accurate, it improves the wave angle estimation compared to the method including the EKF.

Figure 3-22 shows the results for the same 50-component wave as in Figure 3-17. The wave angle estimations are performed simultaneously with the DFTs (t_{DFT}). The figure shows that the accuracy of the estimation has much improved. Even with a minimal amount of measurement data the estimated angle is close to its true value. A slight error occurs for the interval between $[100, \quad 200]$ s. This can be explained by spectral leakage, as some wave components are periodic in the DFT window and some are not. Non-periodic components result in irregularities, which on their turn lead to discrepancies in the parameters provided by the DFT. As the resolution of the DFT increases, the possible influence of spectral leakage decreases.

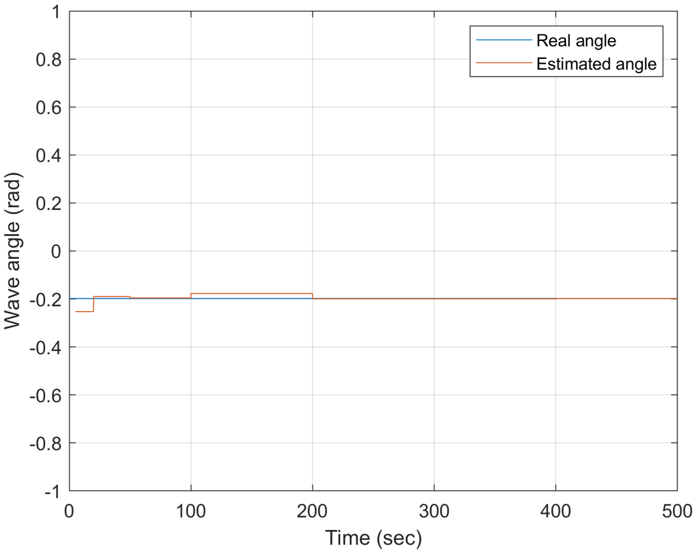

Figure 3-22: Wave angle estimation for the 50-component wave (Figure 3-17), using the DFT wave parameters.

Variable Wave Angle In a real scenario it is likely that the wave parameters change over time. A shifting DFT window can be used to adapt the model to these changes. The corresponding DFT windows are $[t_{DFT} - T_{win}, \quad t_{DFT}]$ s, with T_{win} as the constant window size. If $T_{win} \geq t_{DFT}$ the window will be $[0, \quad t_{DFT}]$. In the case of a changing wave angle, the earlier measurements that might contain waves with a different direction are not taken into account. A shorter DFT window will hypothetically be more sensitive to varying wave angles, as it considers less of the past measurement information. On the other hand, a short window decreases the quality of the DFT parameters leading to a less accurate wave angle estimation. This effect is visible in Figure 3-23. On the left side the DFT window size is taken to be $T_{win} = 20$ s, resulting in a fast but noisy wave angle estimation. The window size on the right is $T_{win} = 50$ s. This results in a more accurate estimation, but responds slower to shifting propagation angles. The DFTs in this case are performed on every time step to gain insight into the process.

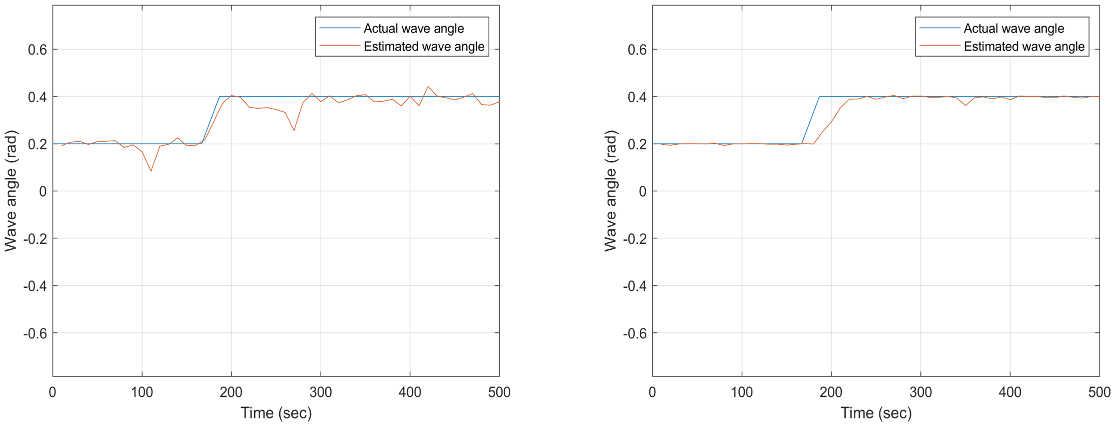

(a) $T_{win} = 20$ s.

(b) $T_{win} = 50$ s.

Figure 3-23: Variable wave angle estimation for two different DFT window sizes.

Multiple Wave Directions During a test run it could occur that there are multiple reflective waves coming in with different propagation angles. Using Eq. (3-18), propagation angles can be determined for every frequency component separately as long as the wave length λ is large enough. Figure 3-24 shows that quality of the angle estimation is different for every component because it depends on the accuracy of the corresponding phases provided by the DFT. The reflected wave considered in the figure contains three main directions, randomly divided over the frequency components. A DFT is performed with a window of $[0, \quad 100]$ s to provide the parameters for the NLS angle estimation. For optimal performance the estimated angles should all be equal to one of the three actual angles. The figure shows that most of the estimated angles are located somewhere in between the angles present in the wave. For these reasons this method does not seem suitable for the estimation of multiple propagation angles. Where the estimation of a single wave angle based on multiple frequency components leads to an accurate performance (Figure 3-22), the estimation based on a single component seems to be too sensitive to irregularities in the wave parameters. A solution could be to estimate a single wave angle based on the few largest frequency components in the case of a multi directional wave. This method is tested for short-crested waves in a next section.

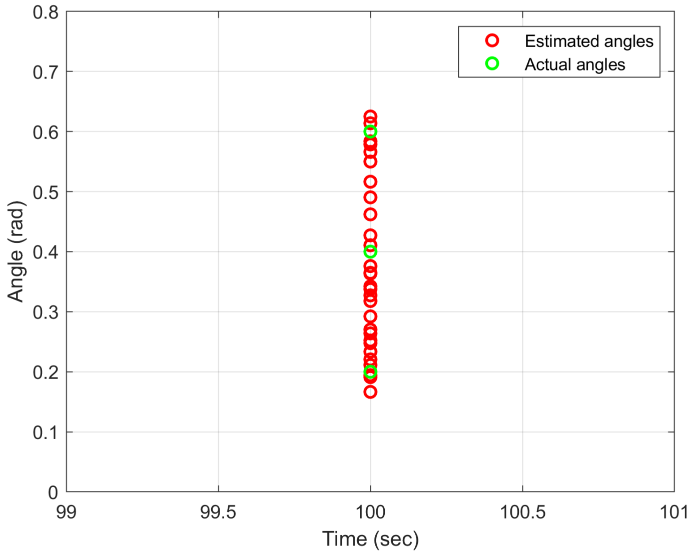

Figure 3-24: Wave angle estimation for a multi-directional wave at 100 sec. A separate wave angle is estimated for all the frequencies qualified for angle estimation. DFT window: $[0, \quad 100]$ s.

3-7 Wave spectrum

In this section, a wave spectrum is used to test the algorithm for a more realistic reflected wave. Although a first order approximation is used for the free-surface elevation time series, the strong irregularity makes it far more realistic than the relatively simple waves used before. Real wave spectra are continuous, resulting in an infinite amount of components. This can obviously not be realised in a simulation. The frequency bin size for the considered wave spectrum is set on 0.01 Hz.

3-7-1 Free-surface Elevation Time Series

The free-surface elevation time series of the wave will be based on a JONSWAP spectrum. To transfer the spectrum to the free-surface elevation time series, the random phase method is used. A clear step by step procedure is provided by [2] in chapter 2.4. Chapter 3.2.1. describes the procedure necessary to extend the wave to the three dimensional space. Figure 3-25 (a) shows the frequency content of the actual wave created using this method, compared to the theoretical JONSWAP spectrum. Figure 3-25 (b) shows the corresponding free-surface elevation time series. The length of the time series has been set on 500 s for the simulation.

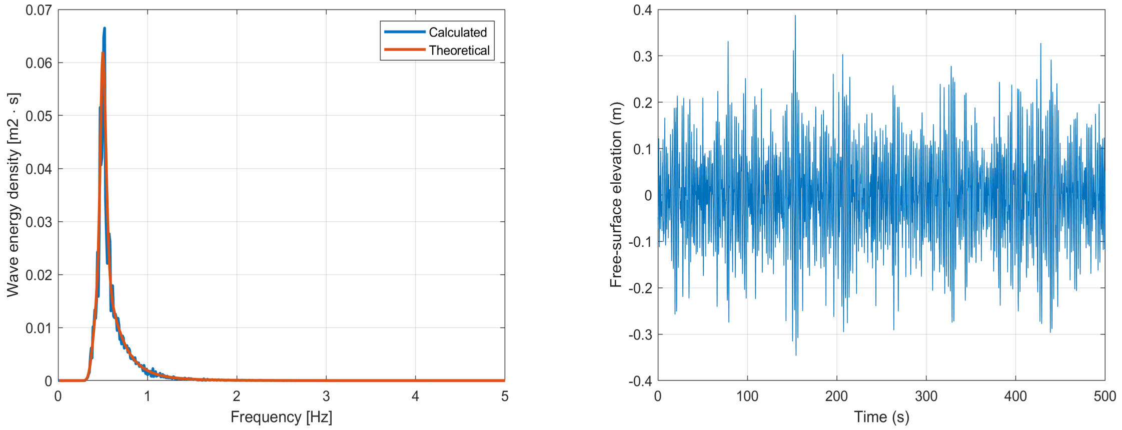

(a) Actual and theoretical JONSWAP spectrum.

(b) Free-surface elevation time series.

Figure 3-25: Theoretical and actual JONSWAP spectrum (a) and corresponding free-surface elevation time series (b). $H_s = 0.4$ m, $T_p = 2$ s.

3-7-2 Identification Results

The sampling frequency for the wave model identification is 10 Hz. As the significant wave energy does not reach beyond 2 Hz, this is more than enough to capture the significant components. The DFTs are performed at $t_{DFT} = [5 \quad 20 \quad 50 \quad 100 \quad 200 \quad 400]$, with DFT windows: $[0, \quad t_{DFT}]$, to create insight into the process. The RMS errors corresponding to the time intervals can be seen in Table 3-4. Note that the DFTs performed after 50 seconds do not necessarily lead to an increased fit for the free-surface elevation time series. Although this might differ for more complex waves, being able to describe the wave well after such a relatively short time brings large advantages. It substantially increases the adaptability of the algorithm regarding wave characteristics that change over time. Even more, DFTs performed over a larger time window usually introduce more components, leading to a larger model. Larger models need more computation time and subsequently slow down the algorithm. Keeping the model at a (small) optimal size optimizes the computation time and the necessary corresponding prediction horizon to compensate for the control action response lag.

Interval (s)	5-20	20-50	50-100	100-200	200-400	400-500
RMS error	0.0602	0.0344	0.0337	0.0359	0.0354	0.0365

Table 3-4: RMS errors for according to the time intervals between the DFTs, corresponding to the wave in Figure 3-25. Model parameters: Threshold $= 10\%$, $F_s = 10$ Hz, Q: $[1 \quad 0.1 \quad 0.1]$, P: $[1 \quad 0.01 \quad 0.01]$, $T_{pred} = 0.2$ sec.

Figure 3-26 shows the wave angle estimation based on the wave parameters provided by the DFT.

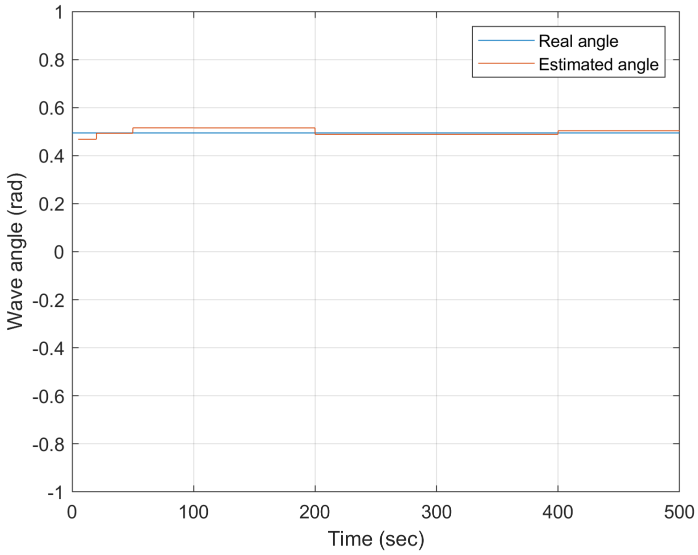

Figure 3-26: Wave angle estimation for the JONSWAP wave in Figure 3-25.

3-7-3 Tuning

This paragraph shows the RMS errors for the time intervals between the DFTs, according to different estimation parameters. These results will all be based on the JONSWAP wave (section 3-7-1), and might differ when considering more complex higher order waves.

Threshold Value Figure 3-27 shows the RMS errors for different DFT threshold values. Taking a higher threshold value results in a larger minimum amplitude (Figure 3-5) and thus less components to be included in the model. Interesting is that up until a threshold value of 80% the RMS errors stay rather constant. Only increasing the threshold to 95% leads to a deficit in wave components and a larger RMS error. Just as concluded from Table 3-4, the wave can be described using a relatively low amount of components, making the algorithm fast and adaptive.

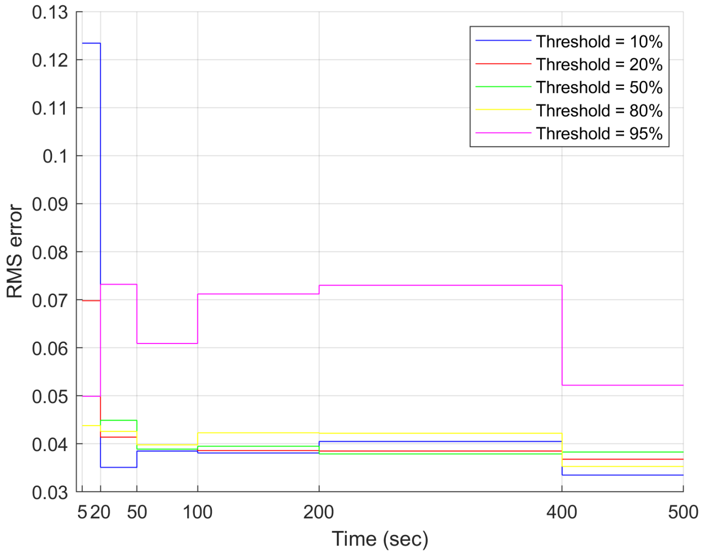

Figure 3-27: Influence of DFT threshold value on the RMS errors between predicted and actual wave (JONSWAP), for different time intervals.

Model Uncertainty Figure 3-28 shows the influence of altering the model uncertainty matrix Q. Increasing the uncertainty for each of the parameters does not have a large influence on the estimation performance of the algorithm. This can be expected as the measurement noise is taken to be $R = 0$. The EKF bases the estimate of a state on the weighted average of the model predicted output and the actual output. If the measurement noise R is small, the measured output is trusted more. In the case of a low model uncertainty, the a priori estimated output is trusted more. For these test runs the measurement noise is taken to be zero. This means that the measurements are taken to be exact, resulting in a large corresponding weight. The diagonal values for the continuous time matrix Q are given: $[q_\varphi \quad q_\omega \quad q_a]$.

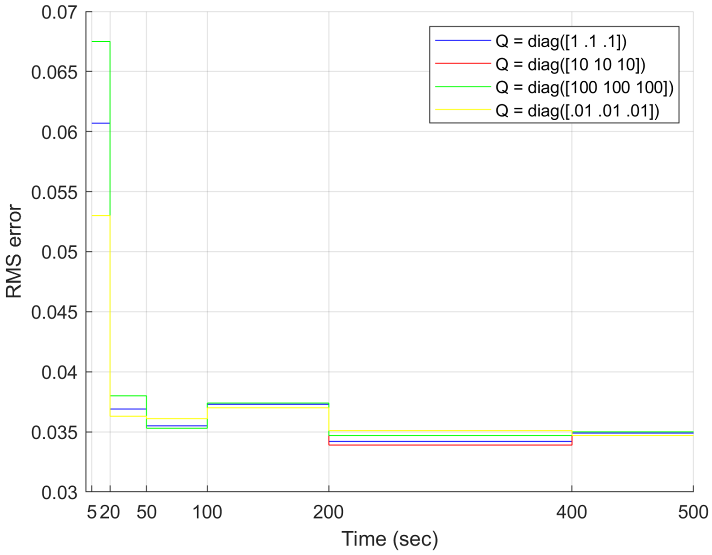

Figure 3-28: Influence of the model uncertainty matrix Q on the RMS errors between predicted and actual wave (JONSWAP), for different time intervals.

State Covariance Figure 3-29 shows the influence of different diagonal values for state covariance matrix P. The given values again correspond to the diagonal values of the continuous time matrix. Increasing the covariance results in a larger estimation error. Taking a low covariance for just the amplitudes still leads to good results. The amplitude is important for the accuracy of the estimation as it has a direct influence on the free-surface elevation.

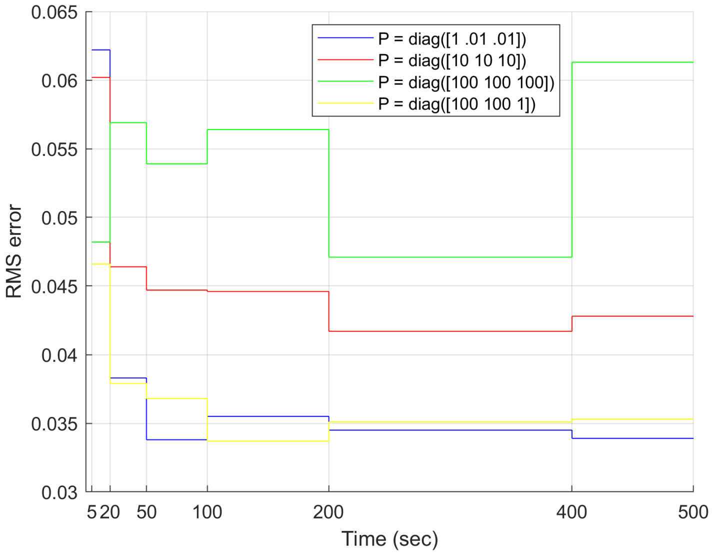

Figure 3-29: Influence of the state covariance matrix P on the RMS errors between predicted and actual wave (JONSWAP), for different time intervals.

Prediction Horizon The influence of the prediction horizon on the estimation performance is shown in Figure 3-30. Increasing the prediction horizon leads to a larger error between the predicted and the actual free-surface elevation. The small mismatches in the model play a larger role for a predicted free-surface elevation further ahead.

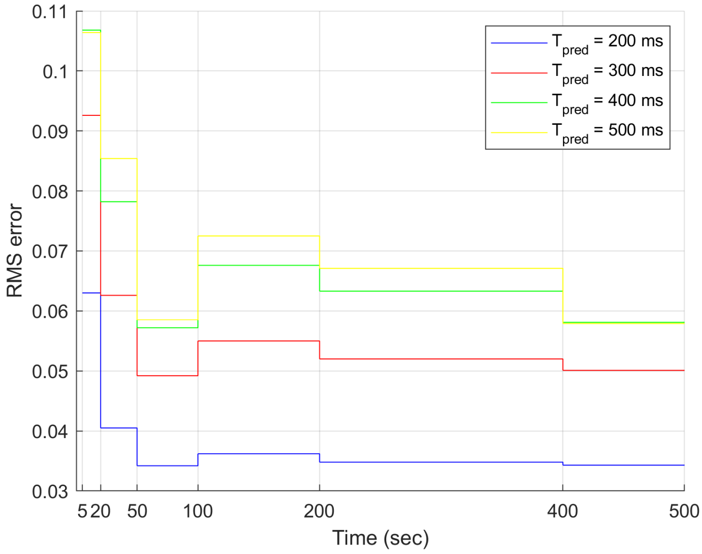

Figure 3-30: Influence of the prediction horizon on the RMS errors between predicted and actual wave (JONSWAP), for different time intervals.

3-8 Wave Heights to Segment Displacements

The identified frequency components will need to be translated into segment displacements for the absorption of the reflected wave. The representation in Figure 3-7 has been extended with the inverse Biésel transfer function, for the translation of the wave heights to segment displacements, and the wave angle estimation. As the frequency content is captured in the wave model, the Biésel transfer function can be used to transfer the identified wave to segment displacements instead of using its approximation (RLF). To give an overview of the proposed algorithm (ARC EKF) from the wave heights measurements to segment displacements for absorption, Figure 3-31 gives a schematic representation. The DFTs provide the phases and wave numbers, obtained from the dispersion relation, for the estimation of the wave angle. The dashed line indicates that DFTs, and subsequently the wave angle estimation, are only performed on certain predefined moments during the measurements of the free-surface elevation (t_{DFT}). The estimated wave angles are used to scale the segment displacements for the absorption of oblique waves (Eq. (2-4)).

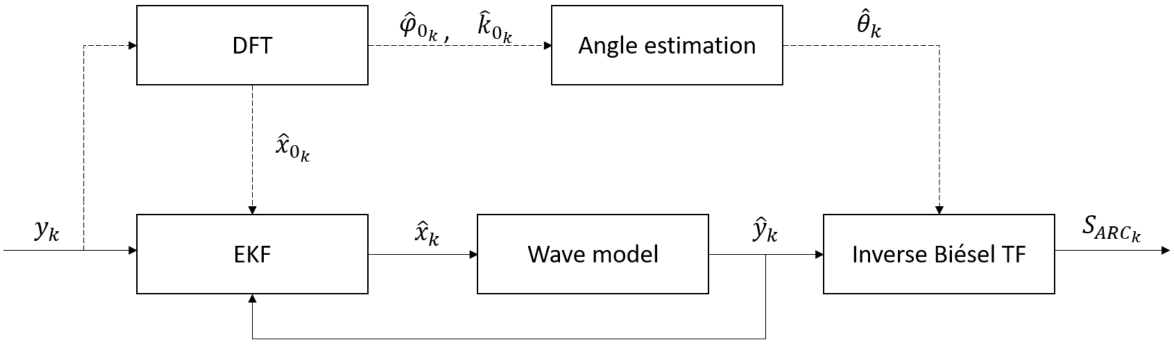

Figure 3-31: Schematic representation of ARC EKF.

Chapter 4

Testing Results

Testing an ARC algorithm is not straightforward as wave generators are very large and expensive machines, which are often not available. Bosch Rexroth does not own such a machine and neither a facility to perform reliable tests in. Any clients of Rexroth owning a wave generator either did not have the machine available or did not allow the performance of test runs for the new algorithm. This means that the test runs will need to be simulated. To gain insight into the performances of the two algorithms a wave spectrum will be used to compute a second order approximation of a reflected wave. A second order wave is used as it provides a much more realistic approximation of an actual wave than a first order approximation. Even more, it is interesting to see whether the identification of a first order wave model, based on second order free-surface elevation measurements, leads to a decent absorption strategy for a second order wave. This is important, as there will always be a discrepancy between the dynamics of actual water waves and the dynamics represented in a (reasonably sized) wave model. The ARC algorithms will process the free-surface elevation time series and compute the segment displacements for absorption, with the goal to obtain a flat water surface. Comparing the segment displacement time series of both the ARC methods with the original segments displacements responsible for the generation of the wave gives insight into the performance of the algorithms. In theory the segment displacement time series responsible for the absorption of the wave should be exactly equal to the time series for the generation of the wave, but with an opposite sign. The two time series should cancel each other out for optimal performance. The absorption performance of the current and new algorithm will be tested for several combinations of wave frequencies, wave heights and propagation angles.

4-1 Simulation Setup

The second order time series for the free-surface elevation of the reflected wave, and the corresponding segment displacements for generation, are obtained using the second order wavemaker theory described in [9]. The computation of the time series is incorporated in a file Rexroth uses for the generation of desired waves during actual test runs. The simulations are performed using an elevated flap type wave generator (Figure 2-1) with a segment width of 0.5 m. The corresponding Biésel function used in the ARC EKF is shown in Eq. (4-1) [2].

$$\frac{H}{S} = \frac{2}{k(h-h_0)}\left[\frac{\sinh(kh)((h-h_0)k\sinh(kh)-\cosh(kh)+\cosh(kh_0))}{\sinh(kh)\cosh(kh)+kh}\right] \tag{4-1}$$

With H as the wave height and S the segment displacement. In the simulations, the segment motion during the test runs is assumed to be zero. The resulting segment displacement time series for the absorption of the reflected waves are purely theoretical, and not taken into account regarding the free-surface elevation measurements of the simulated wave. Figure 4-1 shows a schematic overview of the setup for the simulations. The dashed line encloses the pre-calculated second order time series for the free-surface elevation of the reflected wave, and the second order segment displacement time series for generation. The free-surface elevations are processed by Rexroth's current ARC algorithm and the ARC EKF. The resulting time series for the absorbing segment displacements are compared with the pre-calculated segment displacement time series for the generation of the wave.

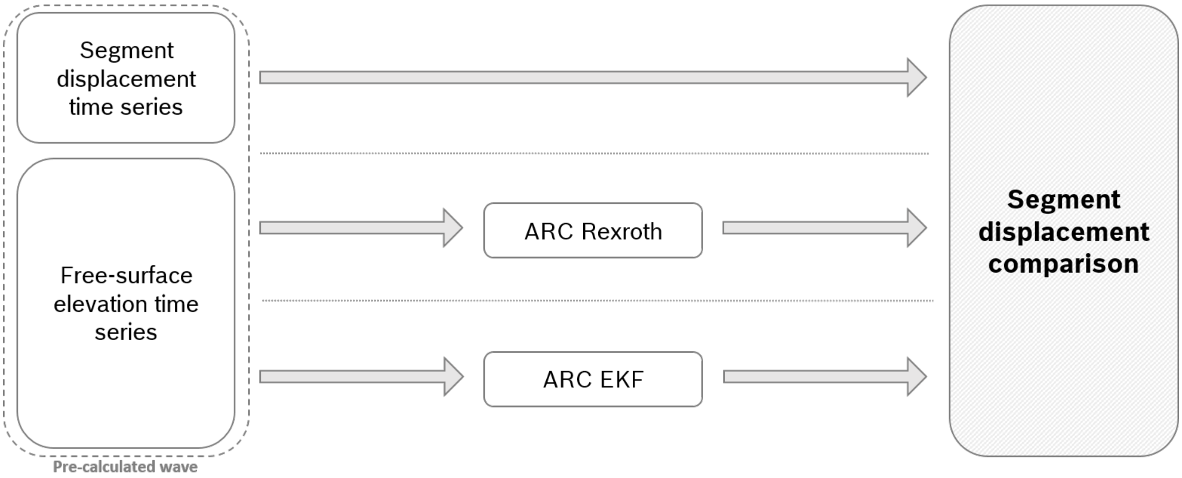

Figure 4-1: Schematic overview of the simulation setup.

For the simulations the water depth $h = 7$ and the hinge elevation $h_0 = 3.5$ m. This settings will be kept the same during all the simulations, as it does not fall within the scope of the research. The first test simulations will be performed on second order regular waves. These relatively simple waves will clarify the (dis)advantages of the two algorithms. After, more realistic irregular waves are simulated. These second order irregular waves are obtained using the Pierson-Moskowitz wave spectrum, as this spectrum is implemented in the Rexroth file for wave generation. In a real test environment the waves will not reach their full energy level immediately, that is why the first 10 s of the time series is used to ramp up the wave signals. For all test scenarios the sampling frequency of the ARC EKF has been put on 25 Hz. The reflected waves considered for the simulations do not contain components with frequencies higher than 5 Hz, so the sampling frequency will be sufficient to capture the frequencies present in wave signal. As Rexroth uses a real-time linear filter to transfer the measured wave heights directly to segment displacements, the sampling frequency is important for the fluency of segment motion. Rexroth uses a sampling frequency of 200 Hz for their actual systems, so this frequency will also be used in the simulations. For the test results, no prediction horizon is implemented for the estimated wave heights and corresponding segment displacements ($T_{pred} = 0$), unless stated otherwise. The simulation results in this section correspond to a single wave generator segment.

Cutoff Frequency When feeding segment displacement time series into a wave generator, the mechanical limits of the system have to be taken into account. The segment of the generator can handle displacements with frequencies limited by a certain bandwidth. This leads to the use of a cutoff frequency that limits the frequencies that are fed into the generator, in order for it to keep functioning properly. This results a decrease in absorption performance for wave frequencies beyond the cutoff frequency. The current systems provided by Bosch Rexroth have a bandwidth of around 7 Hz. As the test waves contain frequencies up to 5 Hz, the corresponding identified frequencies will not reach beyond that limit. For this reason no cutoff frequency is implemented for the upcoming test runs.

4-2 Regular Waves

Figure 4-2 shows a snapshot of the estimation results for a regular second order wave with a frequency $f = 1$ Hz, wave height $H = 0.16$ m and wave angle $\theta = 0°$. R has a nonzero value, despite the absence of measurement noise. Treating the second order dynamics as measurement noise improved the approximation of the wave by the first order model. The estimated first order wave shows a slight phase shifts at the crests and troughs of the wave.

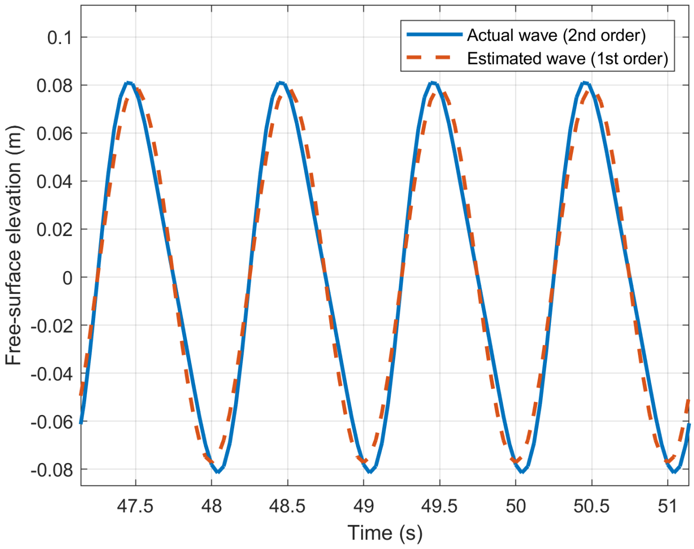

Figure 4-2: Snapshot of estimation results for a regular second order wave. Q: $= [0.1 \quad 0.1 \quad 0.1]$, R $= 10$, P: $[0.01 \quad 0.01 \quad 0.01]$, $t_{DFT} = 1$ s, DFT window: $[0, \quad t_{DFT}]$, threshold: 30%.

Figure 4-3 shows snapshots of the pre-calculated segment displacement (SD) time series for the generation of the wave versus the time series for absorption, according to the current

Rexroth ARC and the ARC EKF. The absorption time series have been plotted with an opposite sign to match the troughs and crest with the generation time series for comparison. This means that the two time series should be equal for optimal performance.

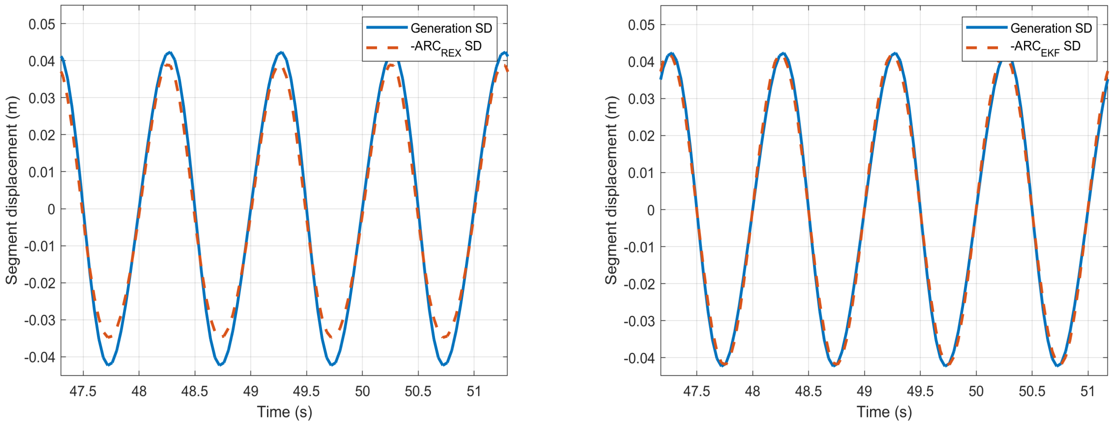

(a) ARC Rexroth

(b) ARC EKF

Figure 4-3: Snapshots of absorption segment displacement time series for both the ARC methods, compared to the time series for the generation of the wave. Corresponding to the wave in Figure 4-2.

The figure shows that the amplitude of the segment displacements for the Rexroth ARC does not match those of the actual ones. The segment displacement time series of the ARC EKF seem to fit the time series for the generation of the wave better. Amplitude spectra will be used to gain insight into the absorption performance of the ARC methods. This time the spectra will be based on the time series of segment displacements. For optimal performance, the spectrum for the generation time series should be equal to the spectrum of the absorption time series. This would indicate that the energy needed to generate these frequency components is equal to the energy used to absorb them. The first ten seconds of the time series can be seen as the start up phase, as it is used for ramping up the wave signal. Both the algorithms are prone to irregularities in this phase and for this reason the first ten seconds of the time series is not taken into account in the spectra. The RMS values for the errors between the absorption and generation spectra are given below the figures.

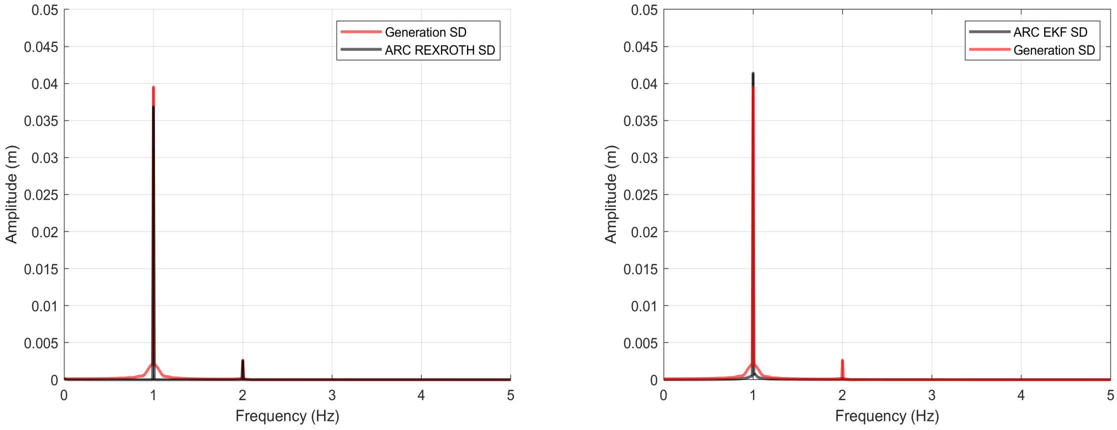

(a) ARC Rexroth, $RMS = 2.2e^{-4}$.

(b) ARC EKF, $RMS = 1.8e^{-4}$.

Figure 4-4: Amplitude spectrum comparison based on the segment displacement time series for the generation of the wave and the absorption time series of both the ARC algorithms. Corresponding to the wave in Figure 4-2. **f = 1 Hz**, $\boldsymbol{\theta = 0}$ °, **H= 0.16 m**, Time window spectrum = **[10, 200]** s.

Corresponding with the result in Figure 4-3, the spectrum for the Rexroth ARC shows a lower amplitude for the peak frequency. The spectrum for the ARC EKF shows that the second order component has not been included in the first order model. Instead the spectrum shows a slightly higher amplitude for the peak frequency to compensate for these unmodeled second order dynamics. Despite the first order dynamics, the RMS error with respect to the generation spectrum is lower for the absorption spectrum provided by ARC EKF.

Figure 4-5 shows the absorption results for a wave with a frequency of 0.4 Hz, as this frequency should theoretically be better absorbed by the Rexroth ARC (Figure 2-2). The amplitude spectrum shows a better absorption performance for the Rexroth ARC. The current Rexroth ARC and the ARC EKF show a similar RMS error for their amplitude spectrum for this frequency.

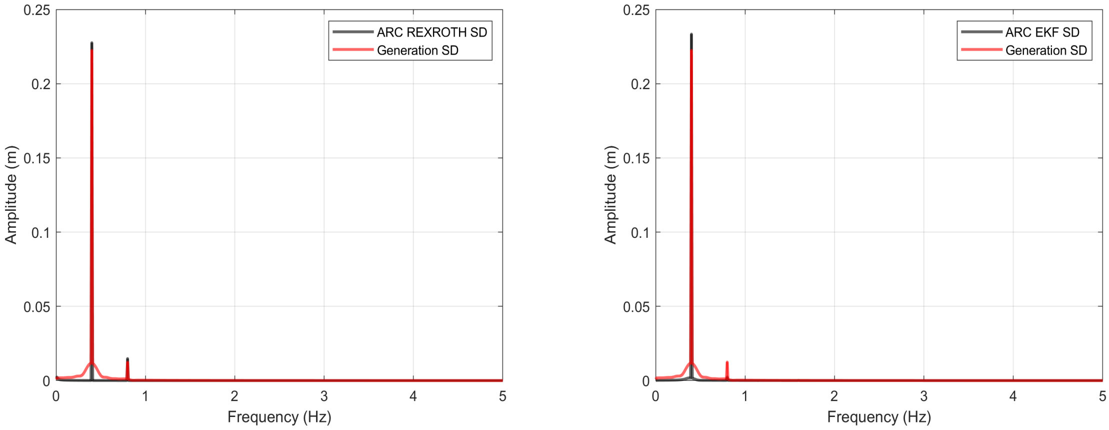

(a) ARC Rexroth, $RMS = 1.2e^{-3}$.

(b) ARC EKF, $RMS = 1.1e^{-3}$.

Figure 4-5: Amplitude spectrum comparison based on the segment displacement time series for the generation of the wave and the absorption time series of both the ARC algorithms. **f = 0.4 Hz**, $\boldsymbol{\theta}$ **= 0** °, **H= 0.6 m**, Time window spectrum = **[10, 200]** s.

Figure 4-6 shows the amplitude spectra for an oblique wave.

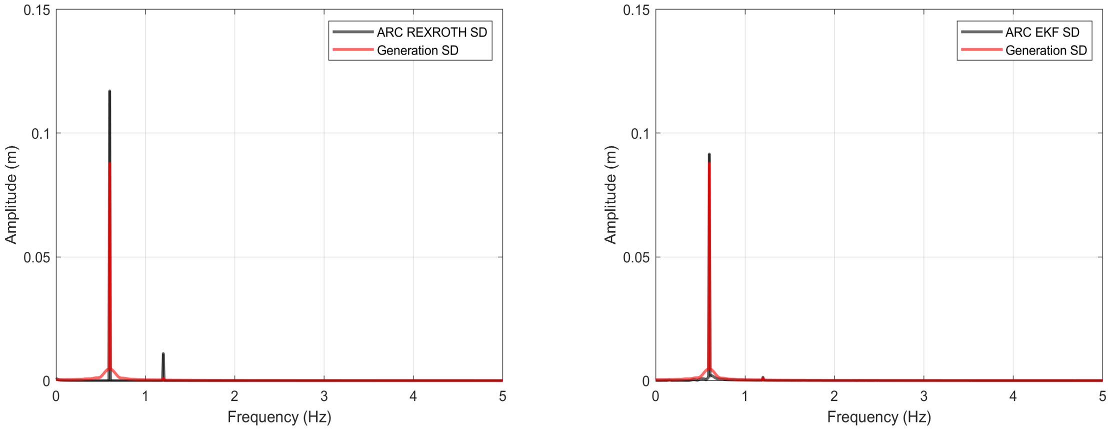

(a) ARC Rexroth, $RMS = 9.9e^{-4}$.

(b) ARC EKF, $RMS = 3.4e^{-4}$.

Figure 4-6: Amplitude spectrum comparison based on the segment displacement time series for the generation of the wave and the absorption time series of both the ARC algorithms. **f = 0.6 Hz**, $\boldsymbol{\theta}$ **= 45** °, **H= 0.5 m**, Time window spectrum = **[10, 200]** s.

As the 2D filter settings are fixed (Eq. (2-3)), the amplitude of the segment displacement for the Rexroth ARC depends heavily on the ratio between the wave length, propagation angle and segment width. The ARC EKF adapts to the incoming wave angle by scaling the segment displacements according to the identified wave angle, leading to a much improved RMS error with respect to the generation spectrum. The spectrum for the ARC EKF still shows an amplitude error for the peak frequency, as a result of the unmodeled second order dynamics.

Based on the absorption results of the regular second order waves, the ARC EKF shows a more steady performance regarding different values for the frequency, wave height and propagation angle. The performance of the Rexroth ARC depends heavily on the properties of the reflected wave. Although the second order dynamics are not included in the first order wave model of the ARC EKF, the model captures the wave dynamics sufficiently to increase the absorption performance.

4-3 Irregular Waves

To gain more insight into the absorption performances of the algorithms, simulations are performed with more realistic waves, obtained with the Pierson-Moskowitz spectrum. The length of the free-surface elevation time series of the irregular waves is set on 500 seconds. The wave spectrum has a frequency resolution of 0.01 Hz and a maximum frequency of 5 Hz. The values for the propagation direction θ, peak period T_p and the significant wave height H_s will be altered for each simulation in order to test the algorithms for different wave reflections. Table 4-1 shows the parameter values for the EKF algorithm, these settings are tuned for optimized performance regarding these complex waves and remain unaltered during all the test runs. DFTs will be performed every 100 seconds, considering the past 100 seconds for the DFT window, to re-initialize the wave model. This makes the EKF ARC algorithm adaptive when it comes to wave properties that change over time. DFTs with shorter time windows will be performed up until the first 100 seconds to deliver absorption performance in the early stage of the free-surface elevation time series.

Diag Q	[10 10 10]
Diag P	[1e-5 1e-5 1e-5]
R	0.1
Threshold	0.05 %
t_{DFT}	[1 5 10 20 50 100 200 300 400]
DFT window $t_{DFT} \leq 100$	[0, t_{DFT}]
DFT window $t_{DFT} > 100$	[$t_{DFT} - 100$, t_{DFT}]

Table 4-1: Parameter values of ARC EKF for the absorption of irregular waves.

The first simulation considers a perpendicular reflected wave with a significant wave height $H_s = 0.4$ m and a peak period $T_p = 2$ s. Figure 4-7 shows the amplitude spectra of the segment displacement time series for the time interval [10, 100] s. This first part of the time series is taken to show the short-term absorption performance. As the model identification takes time to mature, the ARC EKF will most likely perform better after a certain time interval.

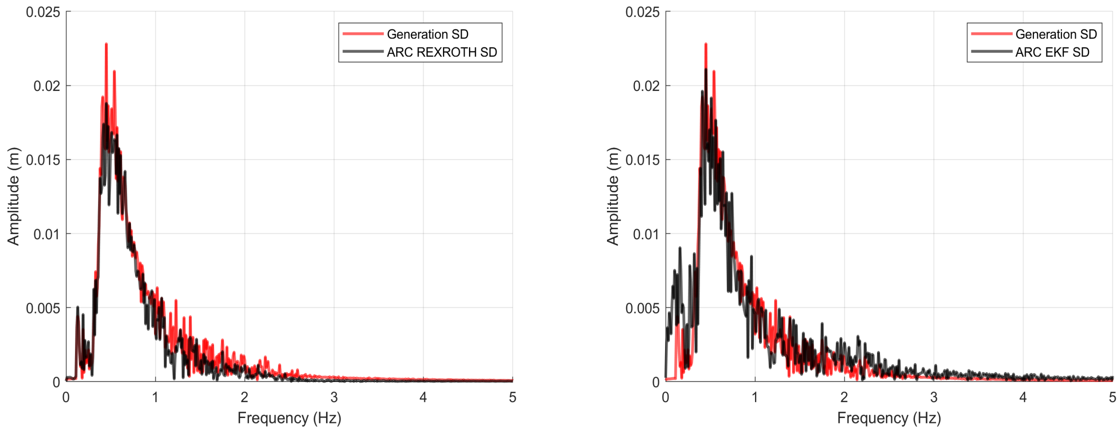

(a) ARC Rexroth, $RMS = 8.2e^{-4}$.

(b) ARC EKF, $RMS = 1.5e^{-3}$.

Figure 4-7: Amplitude spectrum comparison based on the segment displacement time series for the generation of the wave and the absorption time series of both the ARC algorithms. $\boldsymbol{T_p = 2}$ s, $\boldsymbol{H_s}$**= 0.4 m**, $\boldsymbol{\theta = 0}$ °, Time window spectrum = **[10, 100]** s.

The spectra in Figure 4-7 show a noisy line, which makes it less insightful. In Figure 4-8 the noise has been eliminated by the use of a smooth fit line. These smooth fit lines will be used for the upcoming spectra to clarify their differences. The RMS errors between the generation and absorption spectra will still be based on the original spectrum data.

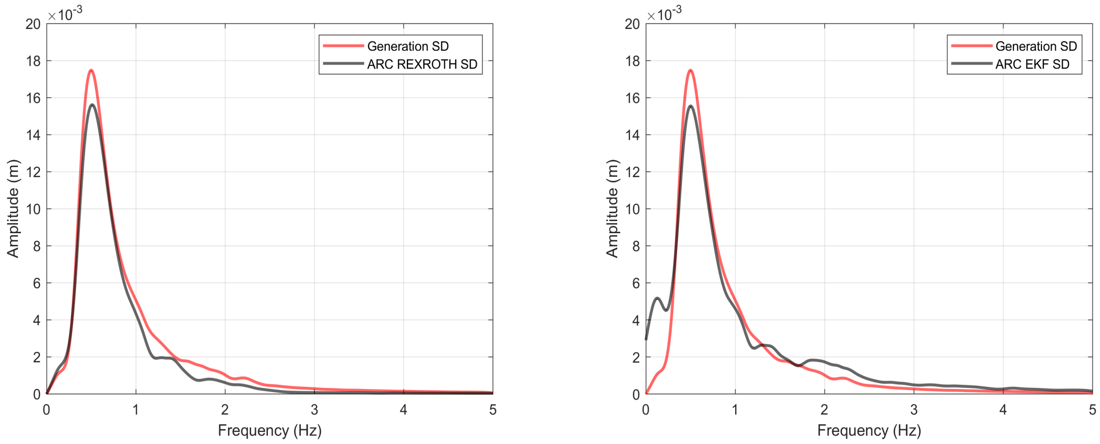

(a) ARC Rexroth, $RMS = 8.2e^{-4}$.

(b) ARC EKF, $RMS = 1.5e^{-3}$.

Figure 4-8: Amplitude spectrum comparison based on the segment displacement time series for the generation of the wave and the absorption time series of both the ARC algorithms. $\boldsymbol{T_p = 2}$ s, $\boldsymbol{H_s}$**= 0.4 m**, $\boldsymbol{\theta = 0}$ °, Time window spectrum = **[10, 100]** s.

Both the algorithms show similar absorption performances for the peak frequencies (≈ 0.5 Hz). The EKF algorithm shows an increase in energy for lower frequencies. This extra energy can be explained by the incorrect segment displacements due to an inaccurate wave model during the early stage of the time series. The Rexroth algorithm shows fast absorption performance already in this early stage, but still shows a discrepancy when looking at the amplitude of the peak frequency. Figure 4-9 shows the spectra for the interval of [100, 500] s. The accuracy of the DFT data increases as more measurement data becomes available. This information sets the basis for the estimation of a more accurate wave model by the EKF. Although the Rexroth ARC and the ARC EKF show similar RMS errors for this time interval, the spectrum of the ARC EKF fits the amplitude of the peak frequency in the generation spectrum better.

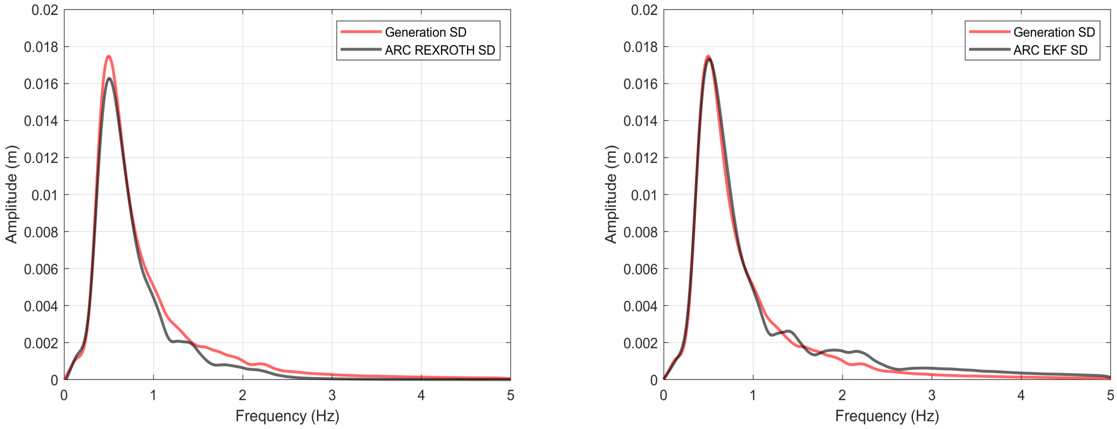

(a) ARC Rexroth, $RMS = 8.9e^{-4}$.

(b) ARC EKF, $RMS = 8.8e^{-4}$.

Figure 4-9: Amplitude spectrum comparison based on the segment displacement time series for the generation of the wave and the absorption time series of both the ARC algorithms. $\boldsymbol{T_p = 2}$ **s**, $\boldsymbol{H_s}$**= 0.4 m**, $\boldsymbol{\theta = 0}$ °, Time window spectrum = **[100, 500]** s.

Only a similar segment displacement spectrum for the generation and absorption of the wave is not enough to draw conclusions about the performance of the algorithm. Figure 4-10 shows snapshots of the time series for the generation and absorbing segment displacements. The RMS values for the errors of both the absorbing time series with the respect to the generation time series is given in the caption of the figures for the time interval [100, 500] s. For this wave, the RMS errors for the time series also indicate a similar absorption performance for the algorithms.

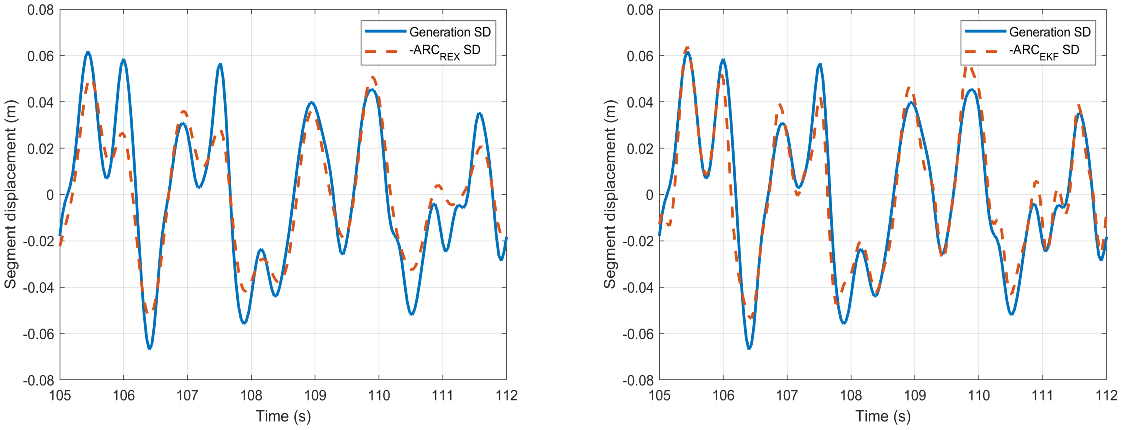

(a) ARC Rexroth, $RMS = 2e^{-2}$. **(b)** ARC EKF, $RMS = 2e^{-2}$.

Figure 4-10: Snapshots of absorbing segment displacement time series of both the ARC algorithms compared to the time series for the generation of the wave. $\boldsymbol{T_p}$ **= 2 s**, $\boldsymbol{H_s}$**= 0.4 m**, $\boldsymbol{\theta}$ **= 0** °.

When considering reflected waves with an oblique propagation angle the performance difference becomes very clear. The 3D implementation of the Rexroth ARC can not compensate for the oblique wave by sufficiently decreasing the amplitude for the segment displacements. The ARC EKF is able to accurately estimate the wave angle, resulting in the proper scaling of the segment displacements.

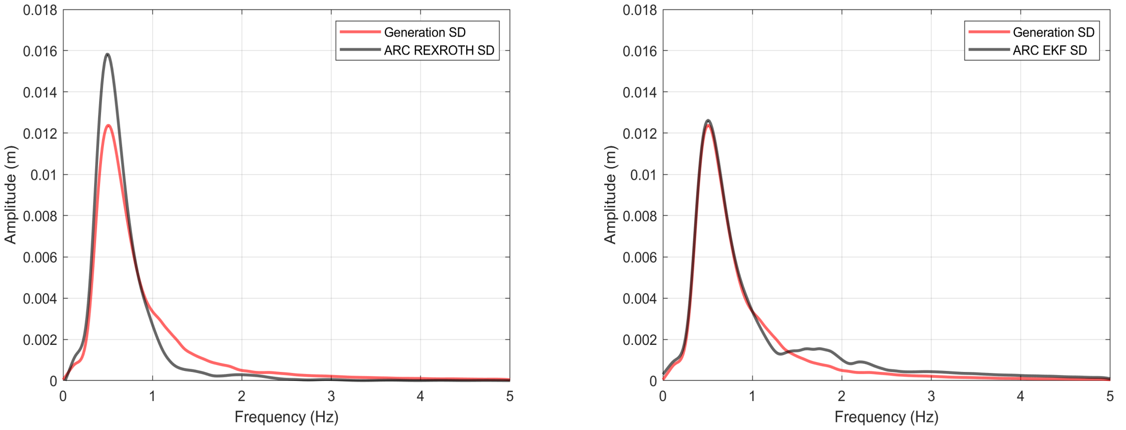

(a) ARC Rexroth, $RMS = 1e^{-3}$. **(b)** ARC EKF, $RMS = 6.5e^{-4}$.

Figure 4-11: Amplitude spectrum comparison based on the segment displacement time series for the generation of the wave and the absorption time series of both the ARC algorithms. $\boldsymbol{T_p}$ **= 2 s**, $\boldsymbol{H_s}$**= 0.4 m**, $\boldsymbol{\theta}$ **= 44** °, Time window spectrum = **[100, 500]** s.

Figure 4-12 shows snapshots of the segment displacement time series. In this snapshot the Rexroth ARC shows a poor absorption performance for the high frequency components in the time series compared to the ARC EKF. This corresponds to the theoretical transfer function in Figure 2-2 (yellow line), in which the Rexroth ARC shows a decrease in performance for frequencies higher than 1 Hz.

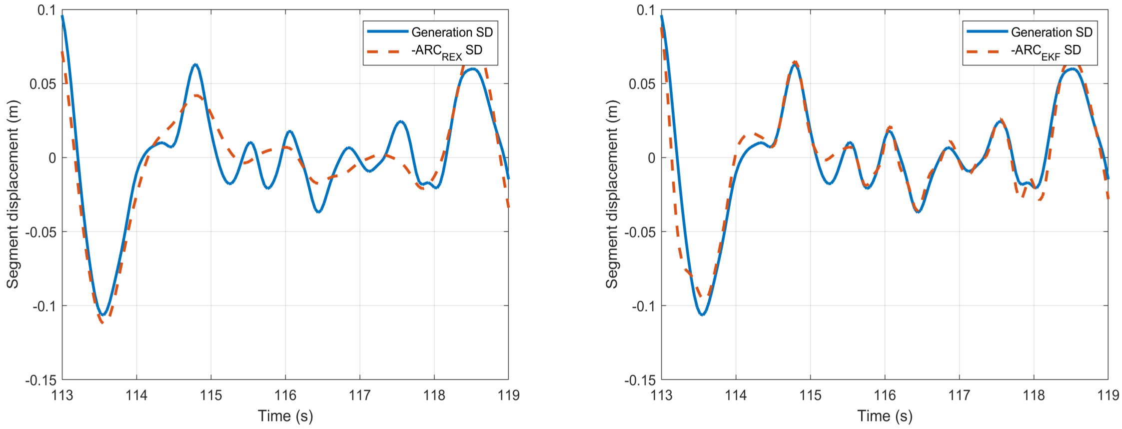

(a) ARC Rexroth, $RMS = 1.9e^{-2}$.

(b) ARC EKF, $RMS = 1.5e^{-2}$.

Figure 4-12: Snapshots of absorbing segment displacement time series of both the ARC algorithms compared to the time series for the generation of the wave. $\boldsymbol{T_p = 2}$ **s**, $\boldsymbol{H_s =}$ **0.4 m**, $\boldsymbol{\theta =}$ **44** °.

Different values for T_p, H_s and θ are chosen for the wave shown in Figure 4-13. Although the Rexroth method shows a good spectrum for this combination of wave characteristics, the EKF shows a slight improvement. Based on this figure this improvement is especially noticeable for the higher frequencies $(1 - 3$ Hz$)$.

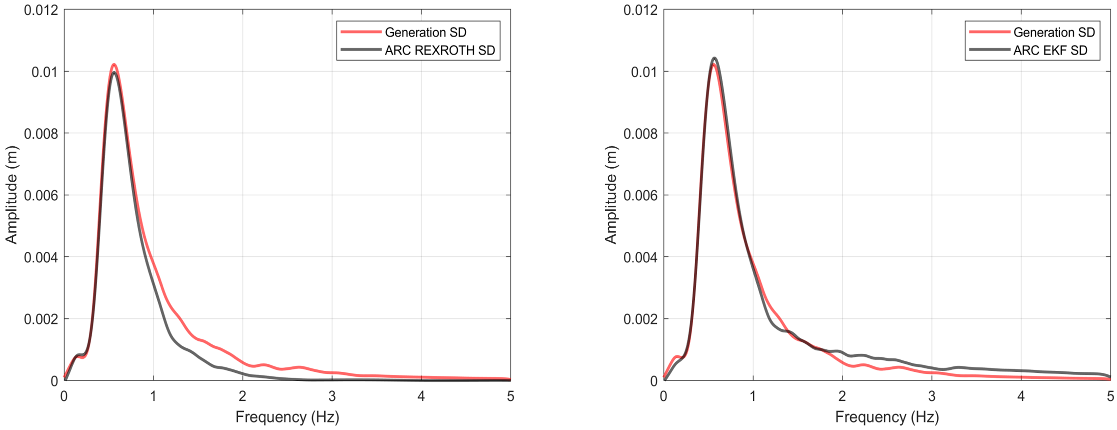

(a) ARC Rexroth, $RMS = 5.5e^{-4}$.

(b) ARC EKF, $RMS = 5.2e^{-4}$.

Figure 4-13: Amplitude spectrum comparison based on the segment displacement time series for the generation of the wave and the absorption time series of both the ARC algorithms. $\boldsymbol{T_p =}$ **1.8 s**, $\boldsymbol{H_s =}$ **0.3 m**, $\boldsymbol{\theta =}$ **15** °, Time window spectrum $=$ **[100, 500]** s.

Figure 4-14 shows snapshots of the segment displacement time series. Although the time series show equal RMS errors, the results show that the higher frequencies are absorbed better by the ARC EKF. This corresponds with the spectrum results in Figure 4-13.

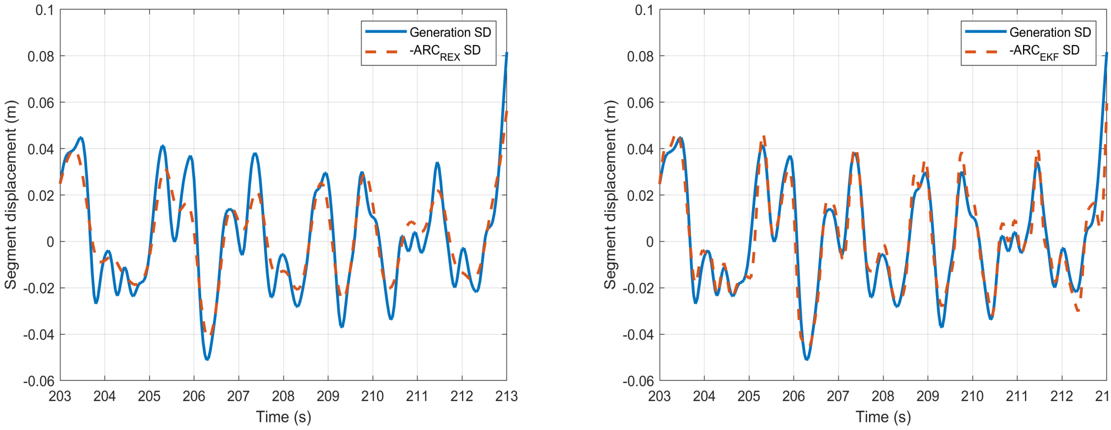

(a) ARC Rexroth, $RMS = 1.2e^{-2}$. **(b)** ARC EKF, $RMS = 1.2e^{-2}$.

Figure 4-14: Snapshots of absorbing segment displacement time series of both the ARC algorithms compared to the time series for the generation of the wave. $\boldsymbol{T_p}$ **= 1.8 s**, $\boldsymbol{H_s}$**= 0.3 m**, $\boldsymbol{\theta}$ **= 15** °.

As the propagation angle of the reflected wave increases, the error between the absorption and generation energy increases for the Rexroth method (Figure 4-15). The larger the propagation angle of the wave, the smaller the necessary segment displacements (Figure 2-5). For large wave angles, this discrepancy can not be compensated by the 2D filter (Eq. (2-3)). The adaptive behaviour of the ARC EKF shows a good fit for the absorption energy for the full frequency range, resulting in a significantly lower RMS error.

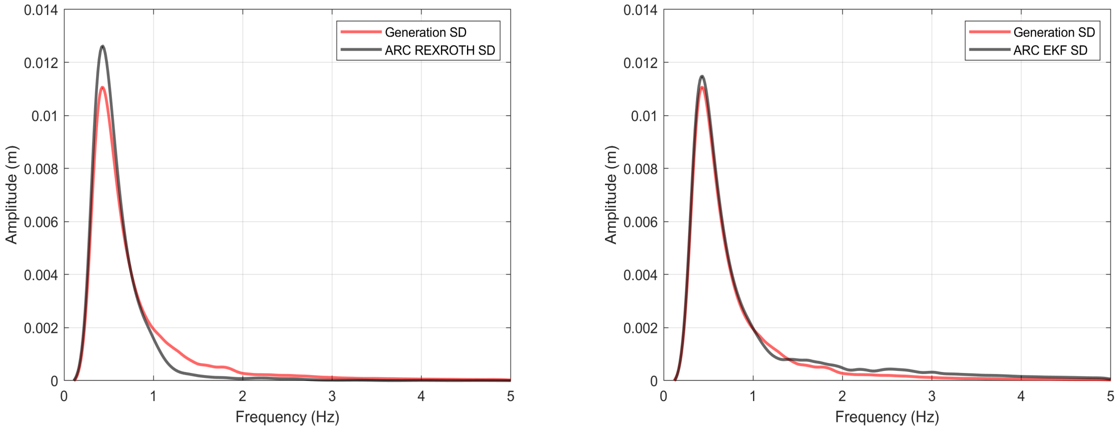

(a) ARC Rexroth, $RMS = 5.5e^{-4}$. **(b)** ARC EKF, $RMS = 3.9e^{-4}$.

Figure 4-15: Amplitude spectrum comparison based on the segment displacement time series for the generation of the wave and the absorption time series of both the ARC algorithms. $\boldsymbol{T_p}$ **=** **2.3 s**, $\boldsymbol{H_s}$**= 0.3 m**, $\boldsymbol{\theta}$ **= 35** °, Time window spectrum = **[100, 500]** s.

Figure 4-16 shows snapshots of the segment displacement time series.

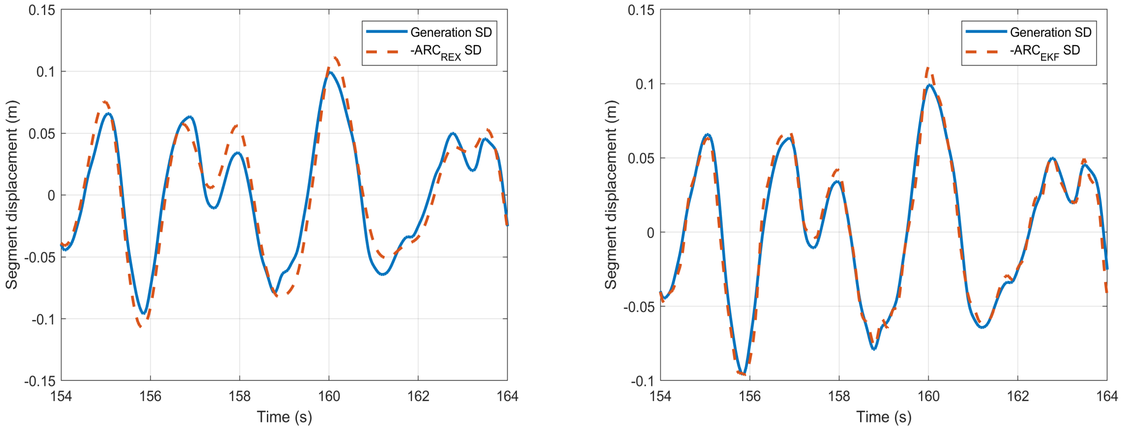

(a) ARC Rexroth, $RMS = 1.1e^{-2}$. **(b)** ARC EKF, $RMS = 6.7e^{-3}$.

Figure 4-16: Snapshots of absorbing segment displacement time series of both the ARC algorithms compared to the time series for the generation of the wave. $\boldsymbol{T_p}$ **= 2.3** s, $\boldsymbol{H_s}$**= 0.3** m, $\boldsymbol{\theta}$ **= 35** °.

Figure 4-17 verifies the major improvement by the ARC EKF for oblique waves. Although both algorithms show a discrepancy in the spectrum for the interval $1 - 2$ Hz, the EKF algorithm shows a much improved peak amplitude.

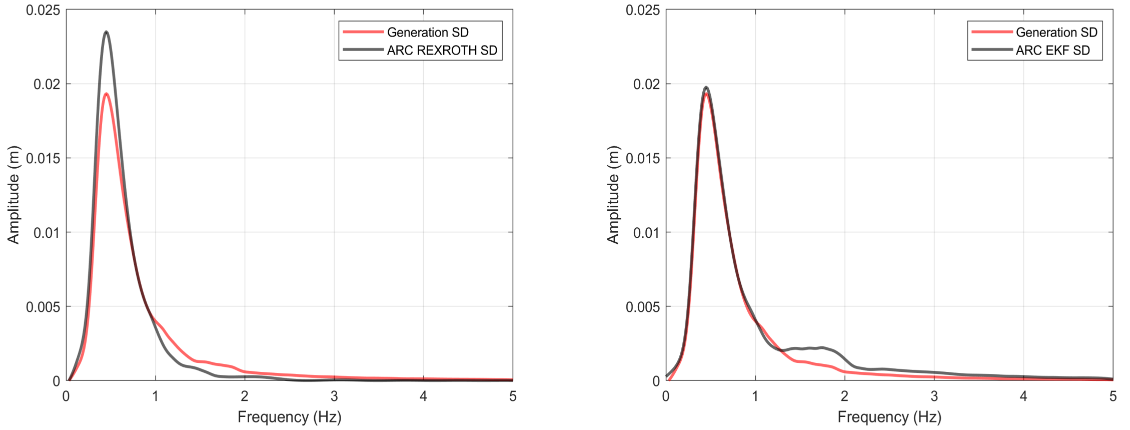

(a) ARC Rexroth, $RMS = 1.3e^{-3}$. **(b)** ARC EKF, $RMS = 1.0e^{-3}$.

Figure 4-17: Amplitude spectrum comparison based on the segment displacement time series for the generation of the wave and the absorption time series of both the ARC algorithms. $\boldsymbol{T_p}$ **= 2.2** s, $\boldsymbol{H_s}$**= 0.6** m, $\boldsymbol{\theta}$ **= 40** °, Time window spectrum = **[100, 500]** s.

Figure 4-18 shows the corresponding segment displacement time series.

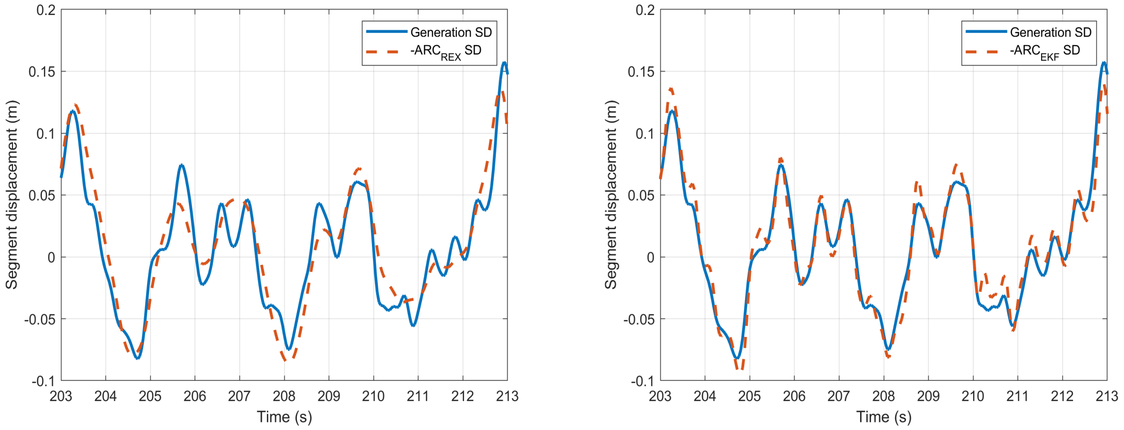

(a) ARC Rexroth, $RMS = 2.7e^{-2}$. **(b)** ARC EKF, $RMS = 2.3e^{-2}$.

Figure 4-18: Snapshots of absorbing segment displacement time series of both the ARC algorithms compared to the time series for the generation of the wave. $\boldsymbol{T_p}$ **= 2.2 s**, $\boldsymbol{H_s}$**= 0.6 m**, $\boldsymbol{\theta}$ **= 40** °.

The results in this section show that the ARC EKF delivers a steady performance for different peak periods, significant wave heights and wave angles. The Rexroth ARC only delivers decent performance for a certain combination of wave characteristics and especially lacks performance regarding the absorption of oblique waves. Introducing wave angle estimation led to a major improvement for the absorption of these waves. Based on the segment displacement spectra and the corresponding time series the ARC EKF shows an improved for the absorption of higher frequencies.

4-3-1 Segment Displacement Prediction

To determine the quality of segment displacement predictions, the displacements will now be based on the predicted wave heights (Eq. (3-13)), instead of the real-time wave heights. A comparison will be made with respect to the real-time segment displacements of the ARC EKF. This is done for the wave corresponding to Figure 4-17. These real-time and predicted segment displacement time series are compared to the time series for the generation of the wave, shown in Figure 4-19. The prediction horizon is set on $T_{pred} = 200$ ms.

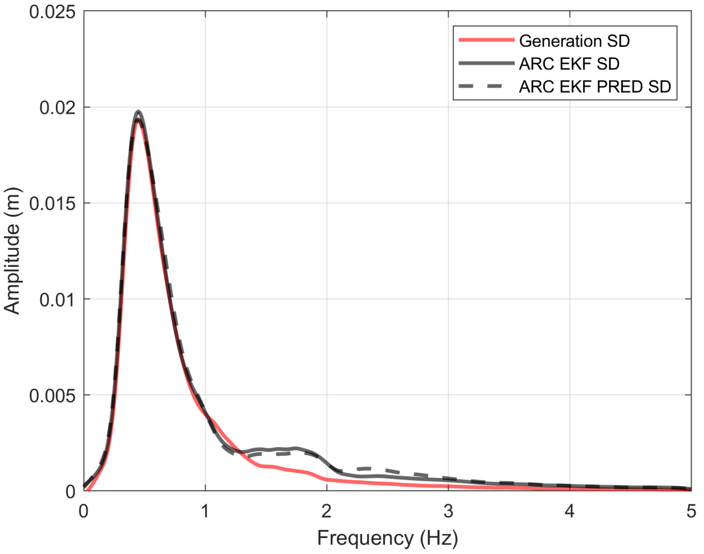

Figure 4-19: Amplitude spectrum comparison based on the real-time and predicted (PRED) segment displacement time series of the ARC EKF for the absorption of the wave versus the time series for the generation of the wave. $\boldsymbol{T_p}$ **= 2.2** **s**, $\boldsymbol{H_s}$**= 0.6** **m**, $\boldsymbol{\theta}$ **= 40** °, Time window spectrum = **[100, 500]** s, RMS prediction spectrum: $\mathbf{1.1}\boldsymbol{e^{-3}}$, RMS real-time spectrum: $\mathbf{1.0}\boldsymbol{e^{-3}}$.

Although the predicted amplitude spectrum has a slightly increased RMS error with the respect the generation spectrum, the difference compared to the real-time spectrum is minimal. Figure 4-20 shows a snapshot of both the predicted and the real-time segment displacement time series compared the time series for the generation of the wave.

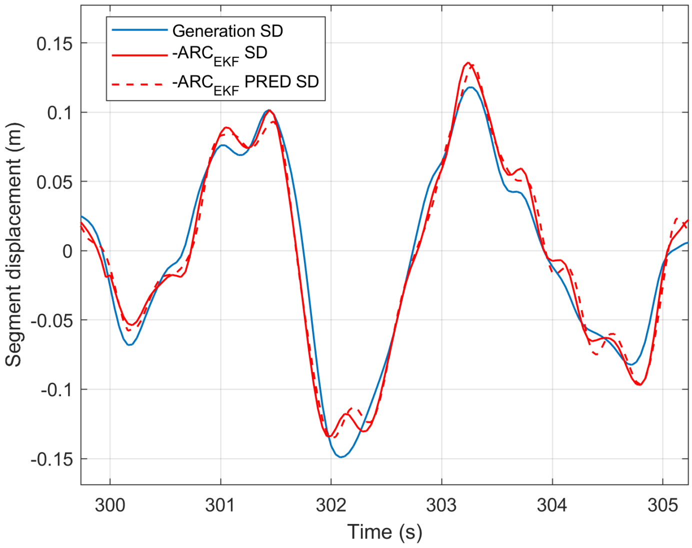

Figure 4-20: Snapshot of the real-time and predicted absorbing segment displacement time series of the ARC EKF compared to the time series for the generation of the wave. $\boldsymbol{T_p}$ **= 2.2 s**, $\boldsymbol{H_s}$**= 0.6 m**, $\boldsymbol{\theta}$ **= 40** °, RMS predicted segment displacements: $\mathbf{2.4e^{-2}}$, RMS real-time segment displacements: $\mathbf{2.3e^{-2}}$.

Also for the time series the RMS error has slightly increased for the predicted segment displacements. Despite these slightly increased RMS errors, the absorption performance for a prediction horizon of 200 ms still shows an improvement with respect to the Rexroth ARC (Figures 4-17 and 4-18).

4-3-2 Short-crested Waves

In the case of short-crested waves the propagation angles of each of the frequency components are based on a spreading function [1]. Although it is considered as a possible wave pattern, it does not often occur in testing facilities. As discussed before, the wave angle estimation shows a poor performance for multiple directions (Figure 3-24). For this reason a single wave angle is estimated based on the ten frequency components with the largest amplitudes. Only the few largest have been chosen, as they have the most influence on the segment motion. The settings for the water height, hinge height and the ARC EKF parameters are equal to the previous simulations for irregular reflected waves. The amplitude spectrum results for the two ARC algorithms are shown in Figure 4-21.

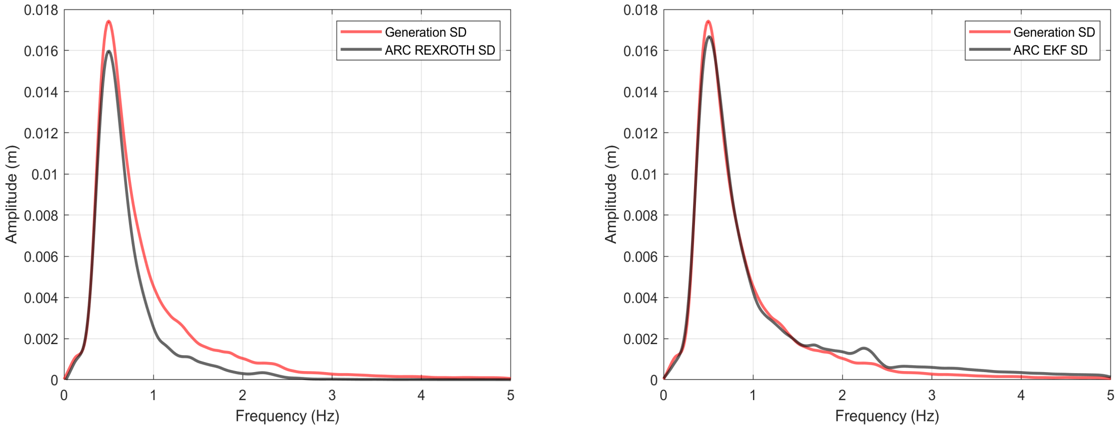

(a) ARC Rexroth, $RMS = 1.2e^{-3}$. **(b)** ARC EKF, $RMS = 8.7e^{-4}$

Figure 4-21: Amplitude spectrum comparison based on the segment displacement time series for the generation of the wave and the absorption of the wave for both the ARC algorithms. $\boldsymbol{T_p}$ **= 2 s**, $\boldsymbol{H_s}$**= 0.45 m**, Time window spectrum = **[100, 500]** s, Spreading parameter **s = 1**.

Figure 4-22 shows snapshots of the corresponding segment displacement time series.

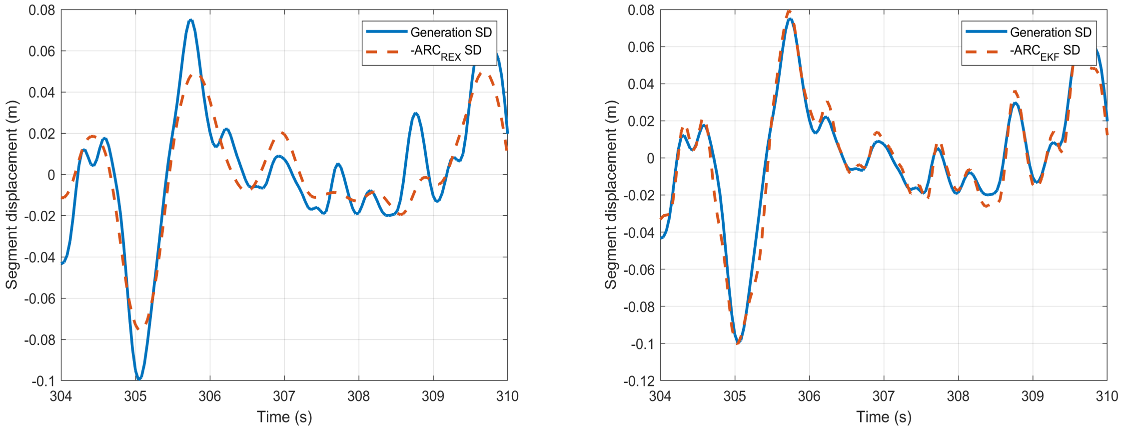

(a) ARC Rexroth, $RMS = 2.4e^{-2}$. **(b)** ARC EKF, $RMS = 2.3e^{-2}$.

Figure 4-22: Snapshots of absorbing segment displacement time series of both the ARC algorithms compared to the time series for the generation of the wave. $\boldsymbol{T_p}$ **= 2 s**, $\boldsymbol{H_s}$**= 0.45 m**, Spreading parameter **s = 1**.

Based on these results, it can be concluded that the ARC EKF, despite the estimation of a single wave angle, shows a substantial improvement regarding the absorption of short-crested waves with the respect to the Rexroth ARC.

4-3-3 Hybrid ARC Algorithm

The ARC EKF algorithm brings a substantial improvement for the absorbing segment displacements as soon as the wave model identification has matured. As the start-up phase for the Rexroth ARC is shorter, the algorithm shows better short-term absorption performance. In order to achieve a good performance for the full time interval of the wave, the two algorithms can be combined to form a hybrid ARC algorithm. The current Rexroth ARC will be responsible for the absorption of the first part of the reflected wave and after a certain time interval, the ARC EKF will take over. Optimally, the ARC EKF should take over as soon as the wave model identification has sufficiently matured. The moment of transition can be made dependent on the fit of the model predicted free-surface elevation time series. In a real scenario, this moment will depend heavily on the complexity of the wave. For the simulated waves in this report, results show (Figures 4-8 and 4-9) that after the first 100 s of the time series the accuracy of the wave model is sufficient to deliver an improved absorption performance. For this reason the fixed moment of transition in the upcoming simulation has been set on 100 s.

Transition Time Series It is important that the transition between the two time series happens as fluent as possible, because extra irregularities result in the generation of additional disturbance waves. Irregular jumps in the segment displacement time series can also clash with the mechanical limits of the wave generator. A smooth transition can be obtained by fading to the new time series over a certain time interval. Figure 4-23 shows the fading over an interval of just one second is enough to avoid strong irregularities in the hybrid time series. With a sampling frequency of 25 Hz, a transition of one second corresponds to 25 time steps.

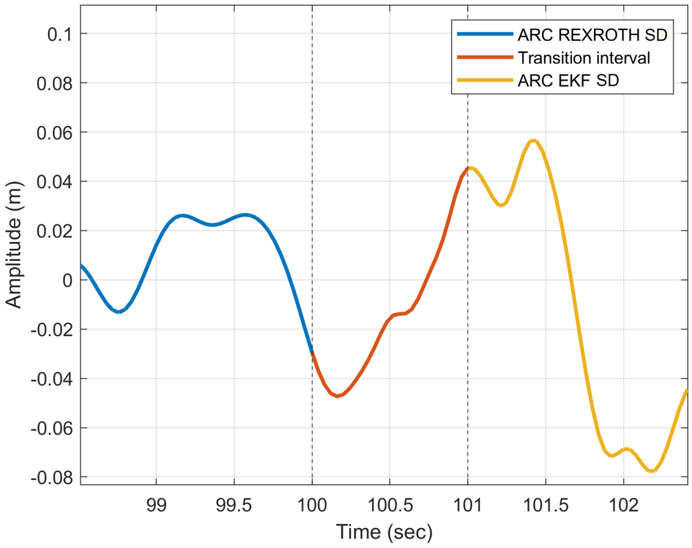

Figure 4-23: Hybrid system: transition from the time series of the Rexroth ARC to the time series for the ARC EKF.

Improvement Rexroth ARC For the first part of the wave, the 3D implementation of Rexroth will still deliver poor absorption results for oblique waves (Figure 4-11). As the estimate for the propagation angle is reasonably accurate after a short time period (Figure 3-26), it could also be used to scale the segment displacements of the Rexroth ARC for the early stage of the reflected wave. The current 3D implementation of Rexroth is omitted and segment displacements delivered by the Rexroth ARC transfer function are multiplied with $\cos(\hat{\theta}_k)$, with $\hat{\theta}_k$ as the estimated wave angle for every time step k. The spectrum improvement is shown in Figure 4-24, for the wave corresponding to Figure 4-11. The spectra are based on the time interval of [10, 100] s. The left figure shows the spectrum for the Rexroth ARC including its original 3D implementation and the right one for the new 3D implementation based on the estimated wave angle (REXROTH+).

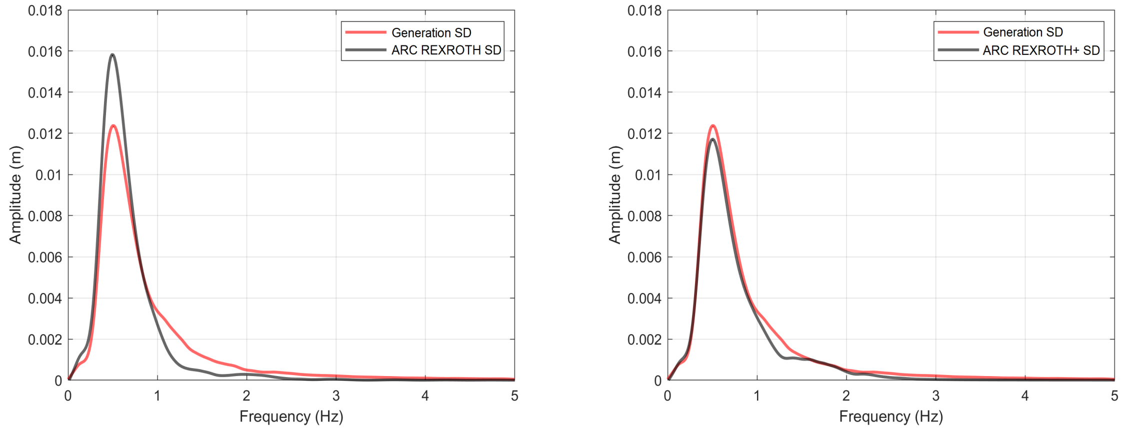

(a) Rexroth ARC: Current 3D implementation, $RMS = 8.8e^{-4}$.

(b) Rexroth ARC: New 3D implementation, $RMS = 5.6e^{-4}$.

Figure 4-24: Amplitude spectrum comparison based on the segment displacement time series for the generation of the wave and the absorption of the wave, for the Rexroth ARC with the current and the new 3D implementation. $\boldsymbol{T_p}$ **= 2 s**, $\boldsymbol{H_s}$**= 0.4 m**, $\boldsymbol{\theta}$ **= 44** °, Time window spectrum = **[10, 100]** s.

Based on these results, including the estimated wave angle for the Rexroth ARC brings a major improvement.

Hybrid Performance Implementing the enhanced Rexroth ARC for short-term absorption and the ARC EKF for long-term absorption, the hybrid ARC delivers good performance over the full time interval of the incoming wave. To clarify the improvement by the hybrid system, Figure 4-25 shows the spectra of both the ARC EKF and the hybrid ARC compared to the generation spectrum for the complete time interval after the start-up phase ([10, 500] s). The ARC EKF shows an amplitude discrepancy for the frequency intervals $0-0.3$ Hz and $1-3$ Hz, due to the immature model identification in the early stage of the free-surface elevation time series. The hybrid method shows an improved spectrum for the full time interval of the reflected wave.

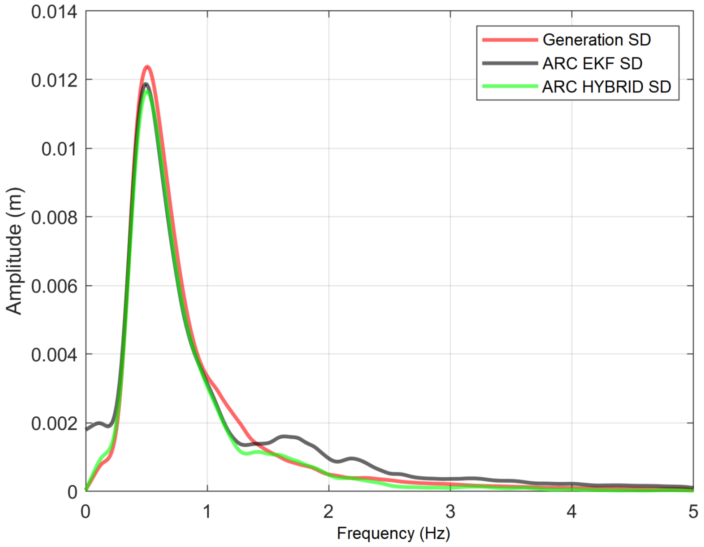

Figure 4-25: Amplitude spectrum comparison based on the ARC EKF and hybrid ARC segment displacement time series for the absorption of the wave versus the time series for the generation of the wave. $\boldsymbol{T_p}$ **= 2** s, $\boldsymbol{H_s}$**= 0.4 m**, $\boldsymbol{\theta}$ **= 44** °, Time window spectrum = **[10, 500]** s, RMS ARC EKF spectrum: $\mathbf{7.6}\boldsymbol{e}^{\mathbf{-4}}$, RMS hybrid ARC spectrum: $\mathbf{5.4}\boldsymbol{e}^{\mathbf{-4}}$.

The RMS error for the segment displacement spectrum of the Rexroth ARC, including its original 3D implementation, is $9.0e^{-4}$ for the full time interval ([10, 500]). Considering the RMS errors in Figure 4-25, the hybrid ARC shows a 40% better fit for the spectrum compared to the current Rexroth ARC. Based on these results, it can be concluded that the hybrid ARC shows a substantially improved performance regarding the full time interval of this reflected wave.

Chapter 5

Real Scenario

This chapter discusses the difficulties that arise when generating waves in laboratory. The simulations consider a more ideal situation compared to a real scenario. Sensors are subject to measurement noise, and the movement of the wave generator segments in water introduces additional effects.

5-1 Measurement Noise

When dealing with sensors for feedback information, measurement noise will often be present. The EKF is powerful when it comes to state estimation in the presence of noise, as it can be specified in the matrix R. The measurement noise of the wave height sensor can be determined by checking the variance of the measurements while keeping the signal, in this case the water level, stable. To check the influence of the measurement noise on the identification of the wave, noise is added to the free-surface elevation measurements in Figure 4-2. Again, a simple wave is used to clarify the performance difference of the two ARC methods. This time the hybrid ARC is used instead of the ARC EKF, because it has proven to deliver the best absorption performance regarding the full time interval of the reflected wave (besides the start up phase). The additional noise has a variance of $\sigma^2 = 1 \cdot e^{-3}$. Figure 5-1 shows snapshots of the time series for the segment displacements of the Rexroth ARC and the Hybrid ARC, based on the noisy measurements. The parameter values for the EKF are equal to the values used for the result in Figure 4-2. As regular waves are identified faster than irregular waves, the moment of transition for the hybrid ARC has been set on 20 s. The RMS errors of the time series correspond to the time interval $[10, \quad 200]$ s.

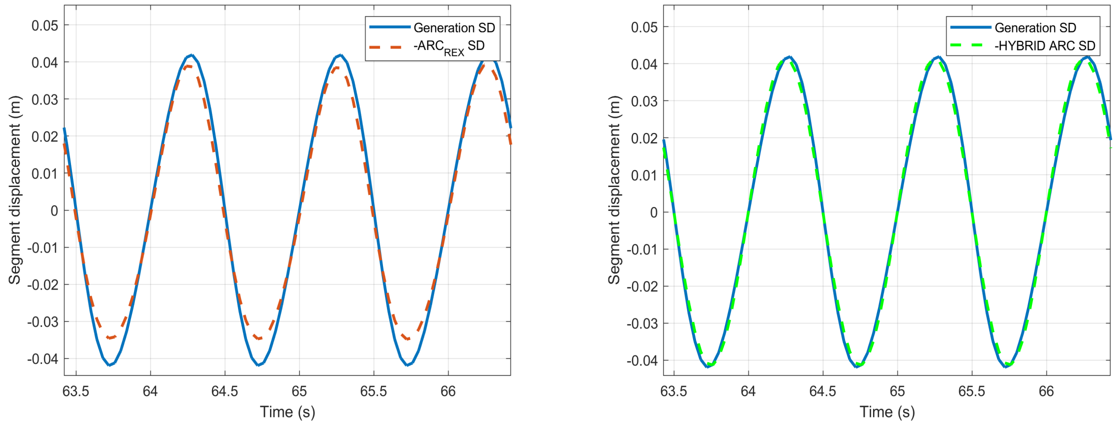

(a) ARC Rexroth, $RMS = 4.1e^{-3}$. **(b)** Hybrid ARC, $RMS = 2.2e^{-3}$.

Figure 5-1: Snapshots of absorbing segment displacement time series for the Rexroth ARC and the hybrid ARC compared to the time series for the generation of the wave. Measurement noise has been added to the free-surface elevation time series of the regular wave. $\boldsymbol{T = 1}$ **s**, $\boldsymbol{H}$**= 0.16 m**, $\boldsymbol{\theta = 0}$ °, Measurement noise: $\boldsymbol{\sigma^2 = 1e^{-3}}$.

The segment displacement time series for the hybrid ARC show a decreased RMS error with respect to the generation time series. This improved result has partially been achieved due to the steady performance of the EKF, despite the presence of measurement noise. This becomes clear when looking at the corresponding amplitude spectra for the segment displacement time series, in Figure 5-2.

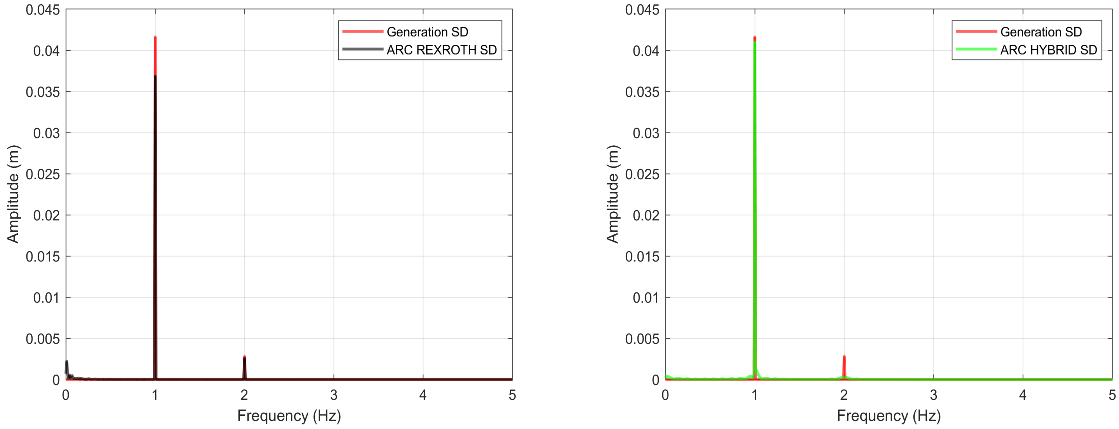

(a) ARC Rexroth, $RMS = 2.4e^{-4}$. **(b)** Hybrid ARC, $RMS = 1.6e^{-4}$.

Figure 5-2: Amplitude spectrum comparison based on the segment displacement time series for the generation of the wave and the absorption time series of the Rexroth ARC and the hybrid ARC. **f = 1 Hz**, $\boldsymbol{\theta = 0}$ °, **H= 0.16 m**, Time window spectrum = **[10, 200]** s, Measurement noise: $\boldsymbol{\sigma^2 = 1e^{-3}}$.

The Rexroth ARC shows some additional energy for low frequencies due to the measurement noise, resulting in a increased RMS error compared to the situation without noise (Figure 4-

4). The steady performance of the EKF results in minimal additional energy in the spectrum due to the noise. The RMS error of the hybrid ARC spectrum even shows an improvement compared to the ARC EKF spectrum for the wave without noise. This emphasizes the power of the hybrid ARC, to deliver an improved performance for the full time interval of the wave.

5-2 Additional Effects

A major difficulty with wave generation in laboratory is the additional effects inherent to the movement of a rigid body in water. This introduces the difference between far-field and near-field waves. The far-field waves correspond to the fully developed desired wave and the near-field waves, so called evanescent waves, arise as a result of the moving segment and decrease with the distance from the wave generator. Eq. (5-1) shows the wave equation as described in [2]. The first part corresponds to the far-field solution and the second part to the evanescent modes. The damping term $e^{-k_n x}$ causes these modes to fade as the distance to the wave generator increases.

$$\eta(x,t) = c \cdot \sinh(kh)\cos(\omega t - kx) + \sum_{n=1}^{\infty} c_n \cdot \sin(k_n h)\, e^{-k_n x} \sin(\omega t) \tag{5-1}$$

A profound derivation of these evanescent modes can be found in [2]. In general only the far-field solution is considered when using the Biésel transfer function for wave generation. Although these evanescent modes can be omitted for the desired fully developed wave, these will still be measured by the sensors. In the case that the wave generator is expected to simultaneously generate a desired wave and absorb the reflected waves, the undesired wave will be determined by subtracting the desired free-surface elevation from the measured one. The remaining free-surface elevation is seen as the reflected wave and is used as an input for the ARC algorithm. To get an accurate description of the reflected wave, the evanescent modes of the desired wave need to be subtracted as well. The second order time series for the progressive wave and additional evanescent modes can be calculated beforehand, so these can be taken into account for the desired wave height.

More of these effects play a role when considering the generation of 3D waves [2]. The snake-like movement of the segments necessary to absorb an oblique wave will never show a perfectly smooth sine, as the width of the segments is not infinitely small. The resulting spurious waves depend on the wavelength λ, the propagation direction θ and the segment width. Incorrect energy is fed into the desired wave due to the variance from the actual displacement with respect to that of a perfect sinusoidal motion. This discrepancy also results in incorrect directed energy causing spurious wave travelling in directions different than the one of the desired wave. These effects cause the actual transfer function from the segment displacement to the wave height to be slightly different than the theoretical Biésel function. A detailed description of these phenomena can be found in [7]. H.A. Schäffer and C.M. Steenberg [9] provide a complete wave generation solution correct to second order, including these additional effects to suppress the generation of spurious waves.

Chapter 6

Conclusion and Recommendation

6-1 Conclusion

Based on the results in this report it can be concluded that the ARC EKF leads to an improved absorption performance for reflected waves with diverging propagation angles, frequencies and wave heights. Especially the wave angle identification is proved to be very useful and can even be implemented in combination with the Rexroth ARC (Figure 4-24). The EKF showed its capability of identifying a first order wave model, based on the measurements of a second order reflected wave. The resulting first order segment displacement time series are proved to be sufficient to substantially increase the absorption performance of this complex wave. Additional tests will need to be performed in order to see whether the first order approximation is sufficient to describe even higher order wave properties, present in e.g. long waves.

As the quality of the wave parameters provided by the DFT depends heavily on its window size, the identification process will need time to mature. This can lead to a lacking absorption performance in the early stages free-surface elevation time series. The Rexroth ARC shows reasonable performance already in an early stage of the reflected wave, but does not improve over time. A solution has been developed in the form of a hybrid ARC. The short-term absorption can be provided by the (enhanced) Rexroth ARC and, when the accuracy of the model is sufficient, the ARC EKF takes over. This leads to an increased performance for the full time interval of the wave (Figure 4-25).

Of course, these test results are based on simulations. The real performance of the hybrid ARC should be tested in an actual testing facility before improvement can be guaranteed. Currently, ARC algorithms are often not used during actual test runs because their performance falls short to add substantial value regarding the suppression of undesired waves. In the case of absorbing reflected waves while simultaneously generating desired waves, the ARC segment displacement adjustments often result in additional perturbations which do not outweigh the absorption performance.

From a broad perspective, if a clear increase in ARC performance can also be verified in an actual test scenario, this can add substantial value to the importance of ARC algorithms for the testing of offshore structures. This improvement can put Rexroth in a leading role when it comes to ARC algorithms, which subsequently results in a stronger market position.

6-2 Recommendation

Based on the results in this report, wave identification is a promising method in the world of ARC algorithms. The influence of the computation time of the identification process has to be investigated during actual test runs. Although short-term predictions can be made, the quality of the absorbing segment displacements decrease as the prediction horizon increases (Figures 4-19 and 4-20). During the last years, the computation power of computers have increased, creating the possibility to use more complex algorithms. Future researches could focus on the identification of higher order models to gain an even higher accuracy of the wave model.

The simulations in this report assume no segment motion with the respect to the free-surface elevation measurements. In a real scenario, the wave height measurements are influenced by the movement of the segment, as the sensors are mounted on the surface. Although the segment motion has been incorporated in the EKF (Eq. (3-6)), additional researched will need to be done in order to clarify the effect of the segment displacements to the performance of the DFT.

Another research could focus on the optimal identification algorithm for the absorption of waves. Grounded reasons led to the choice of EKF for the proposed ARC algorithm in this report but, considering the large variety of identification algorithms, a benchmarking comparison might lead to a more suitable method for this application.

Bibliography

[1] Valentijn Amijs. Active Wave Absorption. *Literature survey TU Delft*, 2019.

[2] Peter Frigaard, Micheal Høgedal, and Morten Christensen. Wave generation theory. *Hydraulics & Coastal Engineering Laboratory Department of Civil Engineering Aalborg University*, 1993.

[3] Tamás Keviczky. Lecture 2 Digital Control (SC42095). *Delft Center for Systems and Control*, 2018.

[4] Manon Kok and Michel Verhaegen. Lecture 4: Kalman Filtering. *Delft Center for Systems and Control*, 2019.

[5] Ian Reid. Estimation II. *PDF: Discrete-time Kalman filter*, 2001.

[6] Stephen Roberts. Lecture 7 The Discrete Fourier Transform. *University of Oxford*, 2003-2006.

[7] Stig Erik Sand. Three-Dimensional Deterministic Structure of Ocean Waves. *PhD thesis of The Technical University of Denmark*, 1979.

[8] Ali H. Sayed and Thomas Kailath. Recursive Least-Squares Adaptive Filters. *http://www.engnetbase.com*, 2000.

[9] H.A. Schäffer and C.M. Steenberg. Second-order wavemaker theory for multidirectional waves. *Elsevier; Ocean Engineering*, 2003.

[10] Maik van de Molengraft. A practical approach to robust reflection compensation. *Coastlab18*, 2018.